POLITECNICO DI TORINO

Corso di Laurea Magistrale
in Ingegneria Aerospaziale e Astronautica

Tesi di Laurea Magistrale

Electro-Magnetic Launchers at the Lunar South Pole

A Feasibility Study

Relatore
Prof. Lorenzo Casalino

Candidato
Luigi Mascolo

Supervisore aziendale
NASA Jet Propulsion Laboratory
Ph.D. Adrian Stoica

A.A. 2017/2018

Abstract

The aim of the research is to explore theoretical and mathematical aspects of a Mass Driver (MD, a.k.a. Electro-Magnetic Launchers, EML) to be used in extreme environmental conditions, in a permanently shadowed region, inside a small celestial body crater, for non-chemical delivery of resources. The analysis consists of two phases.

The first is a preliminary analysis of the state of the art of EML on the two most studied configurations, the Railguns (RGs) and the Coilguns (CGs). The RGs are the most technologically advanced but suffer from an excessive deterioration of the components, reason for which they may be complicated to implement in a scenario where numerous annual launches are expected and where the replacement of broken components is not an easy task.

The latter, more futuristic, can eliminate some of these defects by means of magnetic levitation, and therefore are the focus of this investigation.

The second phase is the preliminary design phase, in which it has been completely configured the dynamical system of the MD, which includes electrical, magnetic, thermal, and structural phenomena. The strong interaction of some of these, namely the electromagnetic and the electrothermal phenomena, has been analyzed in detail, whereas the other problems have been analyzed separately a posteriori. The problem appeared to be strongly non-linear. A SQP algorithm has been developed and used for the constrained nonlinear optimization, in which the Merit Function and the nonlinear constraints are appropriately exchanged to ensure their asymptotic congruence.

The results obtained from the analysis show a good adherence to expectations.

The achieved overall efficiency of the system, namely the set of solar panels, transformers for the energy conversion and distribution, capacitors, all distribution lines, and the MD itself, is similar to the modern pulsed inductive thrusters.

Results demonstrate that the MD works at its best with few launches per year for large masses, but many suborbital launches, ie at lower speeds, may guarantee the same annual tonnage with a non-noticeable decay of performances. This may be considered a benefit, considering that capacitors would be allowed to recharge for longer times, would deteriorate less, and would be more aligned to their current space-qualified TRL.

The mathematical model covers the main electromagnetic and electrothermal phenomena, and its goodness is estimated around 50%. The overall electric efficiency, from the solar panel to the distribution lines, scores around 0.1, heavily influenced by a conservative solar panel efficiency of 0.2.

Future studies may be worth regarding the current tuning to allow the same MD to launch different payloads while maintaining the same magnetic levitation. In addition, a precise FEM study regarding the magnetic levitation is suggested, accompanied by the validation of the considerations regarding the electrical components, especially capacitors and their TRL, the bucket reutilization, and methods for storing the payloads in different points in the Earth-Moon system.

Sommario

Scopo della ricerca è di esplorare gli aspetti teorici e matematici di un Mass Driver (MD, o Lanciatore ElettroMagnetico, EML) da utilizzare in condizioni ambientali estreme in una zona perennemente all'ombra all'interno di un cratere lunare, allo scopo di muovere, senza l'impiego di propellenti chimici, un dato payload. L'analisi consiste di due fasi.

La prima riguarda l'analisi preliminare dello stato dell'arte degli EMLs nelle due configurazioni maggiormente esplorate, cioè i Railgun (RG) e i Coilgun (CG). In tale contesto si è concluso che i RGs sono i più avanzati tecnologicamente ma soffrono un eccessivo deterioramento dei componenti, ragion per cui potrebbero essere di difficile impiego in uno scenario in cui sono richiesti numerosi lanci annui e in cui ci si aspetta che sia complesso sostituire, o riparare, un dato componente danneggiato. I più futuristici CG, invece, possono eliminare alcuni difetti dei RG per mezzo della levitazione magnetica, e pertanto sono stati il focus dello studio.

La seconda fase è quella di design preliminare. In questo contesto si è esplicitato il sistema dinamico del MD, includendo fenomeni elettrici, magnetici, termici, strutturali e orbitali. La forte interazione fra alcuni di questi, specificatamente per i fenomeni elettromagnetici ed elettrotermici, è stata oggetto di approfondimento, mentre le altre problematiche sono state analizzate separatamente a posteriori.

Il problema è apparso fortemente non lineare. L'impiego di un algoritmo SQP ha permesso di effettuare un'ottimizzazione non lineare vincolata, nella quale la funzione oggetto e i vincoli non lineari sono stati opportunamente e mutuamente scambiati per assicurarne la congruenza e convergenza asintotica.

I risultati hanno mostrato una buona aderenza alle previsioni. L'efficienza globale del sistema, che include la struttura solare, i trasformatori per la conversione e distribuzione di energia, i condensatori, tutte le linee di distribuzione e il MD stesso, è nell'ordine dei moderni Propulsori per Induzione a Impulso (PIT). I risultati mostrano come il MD sia più efficiente se impiegato per pochi lanci annui ad alto carico, anche se una serie di lanci suborbitali, cioè a velocità inferiori, potrebbero garantire lo stesso appannaggio annuo, per ciò che riguarda il peso complessivo, senza decadere significativamente nelle prestazioni. La condizione di pochi lanci annui potrebbe essere un beneficio, considerato che i condensatori avrebbero tempi di ricarica maggiori e, pertanto, si consumerebbero meno e sarebbero più in linea con la loro attuale prontezza tecnologica.

Il modello matematico ricopre i principali fenomeni elettromagnetici ed elettrotermici e la sua accuratezza può essere stimata intorno al 50%. L'efficienza elettrica globale, a partire dai pannelli solari fino ai componenti del MD, si attesta intorno allo 0.1, fortemente influenzata da un'efficienza conservativa dei pannelli solari pari a 0.2.

Sarebbe auspicabile approfondire lo studio, in futuro, per ciò che riguarda il tuning della corrente per garantire allo stesso MD masse diverse al lancio, mantenendo comunque la levitazione magnetica. Potenzialmente, tale studio potrebbe essere associato ad un'analisi agli Elementi Finiti per ciò che concerne i campi magnetici all'interno del MD, accompagnato dalla validazione di tutte le considerazioni fatte o suggerite circa i componenti elettrici, specificatamente i condensatori ed il loro TRL, la possibilità di riutilizzare il bucket, e lo studio di metodi per recuperare il payload in diversi punti del sistema Terra-Luna.

Acknowledgement

$\{\varphi, \lambda\} = \{45^\circ\ 3'\ 45''\ \text{N};\ 7^\circ\ 39'\ 44''\ \text{E}\}\ ||\ \boldsymbol{r}_{Tur} = \{4.4599, 0.6000, 4.5099\} \cdot 10^3\,\text{km}$

I extend my most devoted thanks to Prof. Casalino, who, three years ago, following the most bizarre call from Jerusalem to Turin, just talking to me and showing himself as a true man of science as he is, made me understand what was my true way. Perhaps, even today, I have not had the chance to make him notice how much of his interests and passion have become mine.

A heartfelt thanks also to Prof. Iuso, my personal Virgilio, my spiritual guide who always knew how to make me feel part of the great family of DIMEAS and promptly brought me back on the right path whenever there was the need.

Let me thank "la Batti", the formidable Prof.ssa Battipede, who first confidently bet and wagered on my skills, perhaps hidden behind some of my behaviors slightly outside the box.

$\{\varphi, \lambda\} = \{34^\circ\ 8'\ 52''\ \text{N};\ 118^\circ\ 8'\ 37''\ \text{W}\}\ ||\ \boldsymbol{r}_{Pas} = \{-2.4870, -4.6492, 3.5762\} \cdot 10^3\,\text{km}$

My deepest gratitude goes to Adrian Stoica, priceless and commendable mentor, guide, motivator, and friend in my wonderful journey within the JPL. I owe him a considerable part of my feeling included in this complex compromise that is engineering on Earth.

My sincerest thanks also to Prof. Stefano Campagnola, professor at Caltech and luminous beacon in the orbital darkness at the JPL, for pushing me beyond the desiderable in the branch of the astrodynamics that fascinates me most.

Ringraziamenti

$\{\varphi, \lambda\} = \{45^\circ\ 3'\ 45''\ \text{N};\ 7^\circ\ 39'\ 44''\ \text{E}\} \mid\mid \boldsymbol{r}_{Tur} = \{4.4599, 0.6000, 4.5099\} \cdot 10^3\,\text{km}$

Porgo i miei devoti ringraziamenti al Prof. Casalino il quale, tre anni fa, in una stralunata telefonata Gerusalemme-Torino, da vero uomo di scienza qual è, mi ha fatto comprendere quale fosse realmente la mia strada. E forse, fino ad oggi, non ho mai avuto modo di dirgli quanto della sua passione e dei suoi interessi siano diventati miei.

Un particolare ringraziamento al Prof. Iuso, mio personale Virgilio, guida spirituale che ha saputo sempre farmi sentire parte della grande famiglia del DIMEAS e mi ha prontamente riportato sulla diritta via ogni qualvolta ce ne sia stato bisogno.

Lasciatemi ringraziare "la Batti", la formidabile Prof.ssa Battipede, che per prima ha fiduciosamente puntato e scommesso sulle mie capacità, forse nascoste dietro alcuni miei comportamenti leggermente fuori dagli schemi.

$\{\varphi, \lambda\} = \{34^\circ\ 8'\ 52''\ \text{N};\ 118^\circ\ 8'\ 37''\ \text{W}\} \mid\mid \boldsymbol{r}_{Pas} = \{-2.4870, -4.6492, 3.5762\} \cdot 10^3\,\text{km}$

La mia più profonda gratitudine va ad Adrian Stoica, inestimabile ed encomiabile mentor, guida, motivatore e amico nel mio meraviglioso viaggio all'interno del JPL. Devo a lui gran parte del mio sentirmi partecipe di questo complesso compromesso che è l'ingegneria sulla Terra.

I miei sinceri ringraziamenti anche al Prof. Stefano Campagnola, professore al Caltech e luminoso faro nel buio orbitale al JPL, per avermi spinto oltre l'auspicabile nella branca dell'astrodinamica che mi affascina maggiormente.

Table of Contents

List of Figures

List of Tables

Nomenclature

Name	Unit	Value	Description
Latin abc			
a	$\mathrm{m\,s^{-2}}$		Acceleration
	km		Semi-major axis
$a_{\leftmoon}$	km	384748	Moon semi-major axis around Earth
c	$\mathrm{J\,kg^{-1}\,K^{-1}}$		Specific heat capacity
c_ℓ	$\mathrm{m\,s^{-1}}$	$2.99792 \cdot 10^{8}$	Speed of light
c_s	$\mathrm{m\,s^{-1}}$		Speed of sound
e	$\mathrm{J\,kg^{-1}}$		Specific energy
e			Eccentricity
f	Hz		Regular/linear frequency
g, $g_\oplus$	$\mathrm{m\,s^{-2}}$	9.80665	Gravitational acceleration (Earth)
$g_{\leftmoon}$	$\mathrm{m\,s^{-2}}$	1.625	Gravitational acceleration (Moon)
h	$\mathrm{W\,m^{-2}\,K^{-1}}$		Convection heat transfer coefficient
$\hbar$	$\mathrm{J\,s^{-1}}$	$6.62607 \cdot 10^{-34}$	Planck constant
$\hbar$	$\mathrm{J\,s^{-1}}$	$1.05457 \cdot 10^{-34}$	Reduced Planck (Dirac) constant
k	$\mathrm{W\,m^{-1}\,K^{-1}}$		Thermal conductivity
k_B	$\mathrm{J\,K^{-1}}$	$1.38065 \cdot 10^{-23}$	Boltzmann's constant
m_e	kg	$9.10938 \cdot 10^{-31}$	Electron mass
$m_\oplus$	kg	$5.97224 \cdot 10^{24}$	Earth mass
$m_{\leftmoon}$	kg	$7.34767 \cdot 10^{22}$	Moon mass
n	mol		Number of moles
	n/a		Number of elements
p	km		Semiparameter (*semi latus rectum*)
q	C	$1.602 \cdot 10^{-19}$	Particle charge
$\dot{q}$	$\mathrm{W\,m^{-2}}$		Heat flux
$\dot{q}$	$\mathrm{W\,m^{-3}}$		Heat per volume unit
r_a	km		Radius of apoapsis
r_p	km		Radius of periapsis
r_w	m		Wire cross-sectional radius
$r_{,i}$	m		Wire cross-sectional insulation radius
	$\mathrm{W\,m^{-2}}$		Emittance, exitance
v	$\mathrm{m\,s^{-1}}$		Particle velocity
A	$\mathrm{m^2}$		Area
B	T		Magnetic field (magnetic flux density)
	n/a		Clem Coefficients
C	$\mathrm{J\,K^{-1}}$		Heat capacity
$\mathcal{C}$	F		Capacity

$\mathcal{E}$	Pa		Modulus of elasticity (Young's modulus)
E	$\mathrm{N\,C^{-1}}, \mathrm{V\,m^{-1}}$		Electric field
$\mathcal{E}$	J		Energy, various types
F_B	N		Magnetic force
F_E	N		Electrostatic force
F_L	N		Lorentz force
G	$\mathrm{m^3\,kg^{-1}\,s^{-2}}$	$6.67408 \cdot 10^{-11}$	Universal Gravitational constant
$\mathcal{G}$	Pa		Shear modulus of elasticity
H	$\mathrm{A\,m^{-1}}$		Magnetic field (magnetic field intensity)
I	A		Current
J	$\mathrm{A\,m^{-2}}$		Current density
L	H		Inductance
M	H		Mutual inductance
$\mathcal{M}$	$\mathrm{kg\,mol^{-1}}$		Molecular mass
N	molecules		Number of molecules
N_A	$\mathrm{molec\ mol^{-1}}$	$6.02214 \cdot 10^{23}$	Avogadro's number
P	W, $\mathrm{J\,s^{-1}}$		Power, various types
$\mathcal{Q}$	J		Heat
$\dot{\mathcal{Q}}$	W		Power
R	Ω, Ohm		Resistance
$\mathcal{R}$	$\mathrm{H^{-1}}$		Reluctance
$\mathcal{R}$	$\mathrm{J\,mol^{-1}\,K^{-1}}$	8.31447	Universal gas constant
T	K		Temperature
$\mathcal{T}$	$\mathrm{J\,kg^{-1}}$		Specific kinetic energy
$\mathcal{T}$	s		Orbital period
$\mathcal{U}$	$\mathrm{J\,kg^{-1}}$		Specific potential energy
$\mathcal{V}$	V		Voltage
V	$\mathrm{m\,s^{-1}}$		Velocity
V_∞	$\mathrm{km\,s^{-1}}$		Hyperbolic excess velocity
$\mathcal{V}$	$\mathrm{m^3}$		Volume
W	J		Work

Greek $\alpha\beta\gamma$

α	$\mathrm{K^{-1}}$		Thermal coefficient
α_{ref}	$\mathrm{K^{-1}}$		Reference thermal coefficient @20° C
ϵ	n/a		Deformation, elongation, strain
	deg	23.439291	Obliquity of the ecliptic
ε	n/a		Material emissivity
ε_0	$\mathrm{F\,m^{-1}}$	$8.854 \cdot 10^{-12}$	Vacuum permettivity
ε_F	eV		Fermi energy
λ	deg	$0° \le \lambda \le 360°$ E	Longitude ($0° \le \lambda \le \pm 180°$ EW)
μ	$\mathrm{H\,m^{-1}}$		Material permeability
μ_p	$\mathrm{km^3\,s^{-2}}$	GM_{planet}	Standard gravitational parameter
μ_r	$\mathrm{H\,m^{-1}}$		Material relative permeability
μ_0	$\mathrm{H\,m^{-1}}$	$4\pi \cdot 10^{-7}$	Vacuum permeability
ν	deg		True anomaly
ξ	$\mathrm{J\,kg^{-1}}$		Specific mechanical (orbital) energy
ρ	$\mathrm{C\,m^{-3}}$		Charge density
ρ	$\Omega\,\mathrm{m}$		Electrical resistivity

ρ_{ref}	$\Omega\,\mathrm{m}$		Reference electrical resistivity @20° C
ϱ	$\mathrm{kg\,m^{-3}}$		Material density
ω	$\mathrm{rad\,s^{-1}}$	$2\pi f$	Angular frequency
σ	Pa		Stress (normal)
ς	$\mathrm{W\,m^{-2}\,K^{-4}}$	$5.67037321 \cdot 10^{-8}$	Stefan-Boltzmann constant
τ	Pa		Stress (shear)
φ	deg	$0° \leq \varphi \leq \pm 90°$ NS	Latitude (North-South)

Symbols

Name	Description
⊕	Earth
☾	Moon
⊙	Sun
♈	Vernal equinox

Glossary

1D one-dimensional. 47

2BP Two-Body Problem. 59, 63, 64

3BP Three-Body Problem. 59, 65

3D three-dimensional. 47

AC alternate current. 17, 89

BC Boundary Condition. 55

CG coilgun. 69, 70, 71, 72, 73, 74, 105

CR3BP Circular Restricted Three-Body Problem. 59

CS coordinate system. 59

DC direct current. 89

DHT dextral orthogonal triad. 59

DOF Degree of freedom. 40, 41, 42

EE Extreme Environment. 13

EMF electromotive force. 11, 15

EML electromagnetic launcher. 2, 19, 20, 65, 69, 71, 73, 74, 105

EMV Electromagnetic wave. 40, 49

FEM Finite Element Method. 25, 26

JE Joule Effect. 12, 51, 56, 81, 82, 85, 87

LEO Low Earth Orbit. 2

lhs left-hand side. 47, 51, 65, 76, 87

MD mass driver. 2, 10, 51, 67, 68, 69, 73, 75, 77, 85, 90, 104, 106

MDO Mass Driver Optimizer. 92

MF Merit Function. 27, 79, 85

MMF magnetomotive force. 20

MPDB Material Properties DataBase. 13, 35, 45, 46, 48, 58

NAIF Navigation and Ancillary Information Facility. 59

NL Non Linear. 16, 20, 30, 63, 72, 79, 82, 84, 85

ODE Ordinary Differential Equation. 16, 51, 63, 75, 76, 77, 79, 81, 85, 87, 90

PDE Partial Differential Equation. 47, 49, 55, 56

PPI Push-and-Pull Inductance. 71, 73, 74, 105

PSR permanently shadowed region. 67, 73, 88

R3BP Restricted Three-Body Problem. 59

RF reference frame. 59

RG railgun. 69, 70, 74

rhs right-hand side. 8, 47, 51, 65, 87

RMS Root-Mean-Squared. 18

RRR residual resistivity ratio. 13, 50

RS reference system. 59, 60, 63

SC Shackleton Crater. 2, 60, 67, 73

SI International System of Units. 44, 88

sma Semiminor Axis. 62

SMA Semimajor Axis. 62, 64

SOI Sphere Of Influence. 63, 65, 68

SQ superconductive quenchgun. 73

SQP Sequential-Quadratic-Programming. 85

TRL Technology Readiness Level. 90

wrt with respect to. xi, xiii, 13, 20, 31, 34, 35, 43, 45, 48, 49, 50, 51, 54, 56, 58, 59, 60, 68, 88, 109

This document has been reviewed and determined not to contain export controlled technical data.

1. Introduction

> *The dinosaurs became exting because they didn't have a space program. And if we become extinct because we don't have a space program, it'll serve us right!*
>
> — Larry Niven

Since ancient times humanity has sought to know, explore, and reach space. If the *historia magistra vitae* dictum has a meaning, one can not avoid noting that any monoplanetary species may, sooner or later, be destined to undergo the majestic power of nature.
Certainly, it is not intended to emphasize the fragility of the human species, or that a simple catastrophic event can sweep us off the Earth. However, as one chooses to back up important documents on an external storage device, no one can argue that, if humanity becomes a multiplanetary civilization, survival opportunities in the coming millennia would certainly be greater.

Hundreds of studies have been conducted over the last decades regarding the possibility of building a human settlement on Mars, analyzing the feasibility in many fields, including the environmental, scientific, and technological issues. One of the most important problem is that what allows us to live and breathe on our planet, that is the gravitational attraction that retains the air, is at the same time the biggest obstacle to abandon the Earth.

Some of the human needs are mandatory, such as air, water, food, and maybe light. Humans may also need gravity as a consequence of the evolutionary history.

With the aim of establishing ourselves in the near future for a new home –excluding new habitable planets that seem, to date, more distant than our explorative abilities–, all of humanity will need the resources mentioned above, and many others. The first step for this important goal would be to find these resources and to be able to use them or move them easily and without excessive costs.

In recent decades the Moon has become the subject of numerous scientific discussions. After the famous moon landing, the attention had shifted to Mars, considered plausibly a planet more interesting on a scientific level. Yet, recently many have discussed about the possibility of creating a permanent lunar base -human or robotic- in order to build refining centers capable of processing the regolith and obtaining various resources with various techniques.

It is evident the necessity of a device able to move a certain payload -scientific experiments, resources, propellants- between various points of the lunar surface or able to launch it towards the space to be used in other missions. One might wonder what is the most practical, safe, and affordable way to send a payload from the Lunar surface to other destinations.

Chemical guns are limited to practical velocities of about $1 \div 2\,\mathrm{km\,s^{-1}}$ by detonation dynamics, although some multistage laboratory guns have showed muzzle velocities of about

$4\,\mathrm{km\,s^{-1}}$. Moreover, launching a payload via a detonation creates concerns for the great impulsive accelerations it may experience.

The first alternative may be the use of chemical propulsion. Usual multistage rockets can easily produce velocities ranging from the $8 \div 10\,\mathrm{km\,s^{-1}}$ needed for Low Earth Orbit (LEO) to the ΔV for Earth escape maneuvers, even though this implies that the launching vehicle would have, considering the Tsiolkowski equation,

$$\frac{m_f}{m_0} = e^{-\frac{\Delta V}{c}} \tag{1.1}$$

a certain fixed payload fraction. A further observation is that rockets are energetically highly inefficient because most of the propellant is consumed to counteract the gravity force –that is lower on the Moon, but still existent–. Considering the production cost and the small payload fraction of chemical rockets, as well as the environmental issues that may arise –i.e. the production of an unwanted toxic atmosphere–, it is clear that massive space operations or interplanetary travels should base themselves on different technologies that may grant a launching routine of many tons per hour (Kolm et al. 1980).

That is the reason for which electromagnetic launchers (EMLs) are studied. Recent developments and advances in energy and magnet technology make electromagnetic acceleration a viable alternative to chemical rocket spacelaunch –or similar tasks–, usually characterized by heavy engines and the use of fairly huge quantity of propellant. EMLs rely on solar power and can be placed on the Lunar ground, without producing wastes, and are capable of accelerating payloads to high velocities with electromagnetic forces. EMLs also permit almost a tunable constant acceleration during the entire launch duration and are accurately controllable, not subject to projectile size limitations and do not have, ideally, a velocity limit.

Although the technology may be immature for some applications, it is evident that a lunar scenario, in the absence of atmosphere, allows the study of EMLs in a suitable environment, where the terrestrial aerothermodynamic limitations do not come into play.

Therefore, the aim of this study is to produce an estimate of electrical, thermal and material requirements for the use of a lunar EML, namely a mass driver (MD), placed inside the Shackleton Crater (SC) at the lunar south pole, including the analysis of the solar arrays and the energy trasfer. The analysis also presents results about the obtainable tonnage, given a certain structural configuration obtainable through various trade-off processes.

2. Electromagnetism

> *Listening to recordings won't teach you to play piano (though it can help), and reading a textbook won't teach you physics (though it too can help).*
>
> — Schroeder, 1994

The theoretical physic branch called classic electromagnetism studies the physical interaction between electrically charged particles in electric and magnetic fields. An electric charge is a property of matter that allows a charged body to experience a force when placed in an electromagnetic field, i.e. an area in which both electric and magnetic phenomena are present. On the other hand, the electromagnetic field itself can be produced by an electrically charged object in specific circumstances.

There are two types of electric charges: positive charges are commonly referred as protons, while negative ones as electrons. The unit of electronic charge carried by a proton is q, while electrons have charge $-q$, and it is approximately equal to

$$q = 1.602 \cdot 10^{-19}\,\mathrm{C} \tag{2.1}$$

2.1 Electric field

Electrical forces act like gravitation, even if much stronger, varying proportionally as the inverse of the distance squared. It is known that same charges repel each other while opposite charges attract, contrary to what happens with gravity, which only attracts.

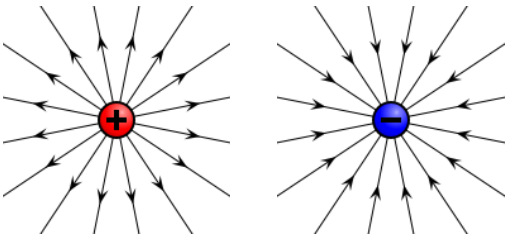

Figure 2.1: Electric field induced by a proton (left) and an electron (right)

Every particle with a charge has an electric field $\boldsymbol{E}$, which is at the base of the electrostatic attraction or repulsion. Indeed, the electric field is a vector field in which the vector force $\boldsymbol{F}_E$ can be defined at a given point. The relationship between charged particles is given by Coulomb's law and it is strongly valid when charges are stationary, in which case the $\boldsymbol{E}$-field is called electrostatic. If two generic charged particles q_1 and q_2 do not move in time, then the repulsive or attractive force $\boldsymbol{F}$ acting on them is

$$\boldsymbol{F} = \frac{q_1 q_2}{4\pi\varepsilon_0 r^2}\frac{\boldsymbol{r}}{|\boldsymbol{r}|} \tag{2.2}$$

The electrostatic force $\boldsymbol{F}_E$ acting on a stationary particle q in an electrostatic field $\boldsymbol{E}$ is

$$\boldsymbol{F}_E = q\boldsymbol{E} \tag{2.3}$$

Therefore positive charges $+q$ are attracted in the direction of the electrostatic field, while electrons $-q$ are pushed in the opposite direction. If an electrostatic field $\boldsymbol{E}$ is applied on a neutral body with $n_+ = n_-$ particles, then there is no net force acting on the system, suggesting that the electrostatic force in eq. (2.3) does not depend on the particle's mass.

The $\boldsymbol{E}$-field is a conservative vector field in which the amount of work needed to move a single charge does not depend on the specific path of the particle but only on its initial and final position. In other terms, the $\boldsymbol{E}$-field is irrotational and simply connected, therefore it is the gradient of a function called electric potential V, a scalar quantity.

$$\boldsymbol{E} = -\nabla V \tag{2.4}$$

Another deduction is that the $\boldsymbol{E}$-field lines go towards zones at lower potential V. Recalling by eq. (2.3) that positive charges accelerate in the same direction of the $\boldsymbol{E}$-field, it follows that protons move towards lower potential zones and electron towards higher ones.

2.2 Magnetic field

The magnetic field $\boldsymbol{B}$ is a solenoidal vector field, defined by both a direction and a magnitude, that can be generated by a moving electric charge or by a variable electric field over time[1]. The term "solenoidal" indicates that the magnetic field flux through any closed reference surface is null or, in other terms, that the vector field has zero divergence. It follows that the magnetic field is rotational and nonconservative. In addition, an important consequence is that magnetic monopoles do not exist.

An electrical charge at rest produces no magnetic effects (Millikan and Bishop 2016). A moving charge, instead, –such as those in an electrical wire in which a current I flows– generates a $\boldsymbol{B}$-field. The Biot-Savart law, a particular case of the more general Laplace formula, defines the $\boldsymbol{B}$-field produced by a constant current I in a straight wire at a generic point at distance r

$$\boldsymbol{B} = \frac{\mu_0 I}{4\pi}\int_\ell \frac{\mathrm{d}\boldsymbol{\ell} \wedge \hat{\boldsymbol{r}}}{r^2} \tag{2.5}$$

[1] William Thomson (recently known as Lord Kelvin) was the first to distinguish between magnetic flux density $\boldsymbol{B}$ and magnetic field intensity $\boldsymbol{H}$ and to find a correlation between the two (Whittaker 2012). Nowadays the two terms are often confused and $\boldsymbol{B}$ is commonly referred simply as "magnetic field".

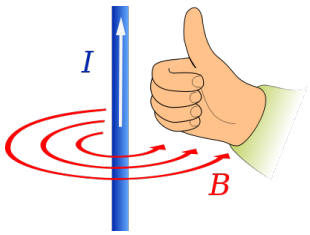

Figure 2.2: $\boldsymbol{B}$-field generated by current I in a wire (Physics, Stackexchange 2017)

Ampère's law provides another relation, stating that the integral along a closed ℓ line of the $\boldsymbol{B}$-field is proportional to the algebraic sum of the concatenated currents through ℓ

$$\oint_{\ell} \boldsymbol{B} \cdot \mathrm{d}\ell = \mu_0 \sum_{i=1}^{n} I_i = \mu_0 I_{enc} \tag{2.6}$$

For example, referring to Fig. 2.2, as long as the closed line ℓ encloses or coincides with the wire circumference, the concatenated current is equal to the one flowing in the wire. For narrower ℓ, the enclosed current is a fraction of the total.

If an external applied $\boldsymbol{B}$-field exists, a moving particle of charge q is subject to an additional force $\boldsymbol{F}_B$, which is velocity-dependent and adds to the electrostatic one in eq. (2.3)

$$\boldsymbol{F}_B = q\boldsymbol{v} \wedge \boldsymbol{B} \tag{2.7}$$

where $\wedge$ is the vector cross-product. $\boldsymbol{F}_B$ is perpendicular to both the velocity $\boldsymbol{v}$ of the charge q, and therefore of current I, and the $\boldsymbol{B}$-field direction, and its direction can be found rapidly with the right-hand rule.

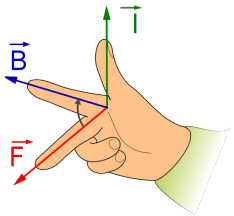

Figure 2.3: Right-hand rule: thumb points $\boldsymbol{v}$ (direction of current), index $\boldsymbol{B}$ (direction of applied field), palm direction is $\boldsymbol{F}_B$ (magnetic force on the particle)(Physics, Stackexchange 2017)

2.2.1 Magnetic field of a solenoid

A solenoid is a coil of length L and winding density n that forms a helix in which current flows. It is usually continuous, meaning that it is formed by infinitely-thin coils highly packed among them, leaving no space in between, and its length L is substantially greater than its diameter D. For these definitions, it is often referred as a cylindrical conductive sheet.

By using Ampere's law, eq. (2.6), the $\boldsymbol{B}$-field calculation is straightforward. Any closed line ℓ that does not enclose a portion of the windings has no current through the line and, therefore, does not generate a magnetic field.

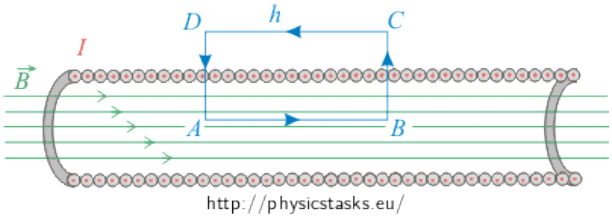

Figure 2.4: Magnetic field in a solenoid

Thus a suitable closed path for such calculation is, for example, that shown in Fig. 2.4. For $L \gg D$, the magnetic field inside the solenoid is parallel to the axis; consequently, the ℓ paths $\overline{BC}$ and $\overline{DA}$ have $\boldsymbol{B} \cdot d\boldsymbol{\ell} = 0$. Even the $\overline{CD}$ line outside the solenoid does not contribute to Ampere's law. To be convinced about this, it is possible to apply Ampere's law to a closed rectangular path outside the solenoid: the two lines perpendicular to the axis nullify by symmetry (and/or for the previous consideration) and there will be no concatenated current. It follows that the line integrals of the two parallel lines would be equal and opposite to any distance these two are located from the axis. By extrapolation, if one of these is at an infinite distance, it would no longer be affected by the field lines, canceling its contribution and, thus, also the other.

The consideration that the magnetic field outside a solenoid is null is strongly accurate for infinitely long solenoids. In this case, exdending $\overline{AB} = L$, it follows

$$\begin{aligned} \oint_\ell \boldsymbol{B} \cdot \mathrm{d}\ell = \int_A^B \boldsymbol{B} \cdot \mathrm{d}\ell &= \mu_0 \sum I \\ BL &= \mu_0 InL \\ B &= \mu_0 nI \end{aligned} \tag{2.8}$$

where the enclosed current is given by the current I in each of the $N = nL$ coil turns.

2.2.2 Magnetic field due to a single coil

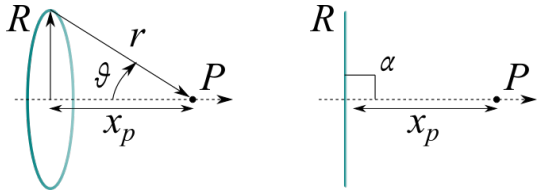

Figure 2.5: Single coil side view (left), top view (right)

In Fig. 2.5 there is a single coil of radius R in which a current I flows. To determine the magnetic field at a point P due to a single loop of current it is considered a coil section with radius R spaced by x_P from the point itself. By considering an infinitesimal length of the wire $d\ell$ and applying the Biot-Savart law

$$d\boldsymbol{B} = \frac{\mu_0 I}{4\pi} \frac{d\boldsymbol{\ell} \wedge \hat{\boldsymbol{r}}}{|\boldsymbol{r}|^2} \tag{2.9}$$

By solving the cross product,

$$dB = \frac{\mu_0 I}{4\pi r^2} d\ell \sin\alpha \sin\vartheta = \frac{\mu_0 I}{4\pi r^2} d\ell \sin\vartheta \tag{2.10}$$

Where $\sin\alpha = 1$, as represented in Fig. 2.5. With trigonometric relations, $\sin\vartheta = \frac{R}{r}$. By substituting and integrating, it results

$$B = \int_\ell \frac{\mu_0 I}{4\pi r^2} \frac{R}{r} \, \mathrm{d}\ell \tag{2.11}$$

By supposing to have a steady current, the constant terms are taken out of integral

$$B = \frac{\mu_0 I R}{4\pi r^3} \int_\ell \mathrm{d}\ell \tag{2.12}$$

Therefore

$$B = \frac{\mu_0 I R}{4\pi r^3} 2\pi R \tag{2.13}$$

The distance r is the hypotenuse of the triangle formed by the two sides R and x_p. It follows the formulation of the magnetic field generated by a single coil at a point P

$$B = \frac{\mu_0 I}{2} \frac{R^2}{\left(R^2 + x_p^2\right)^{\frac{3}{2}}} \tag{2.14}$$

2.2.3 Magnetic field induced by an N turn coil

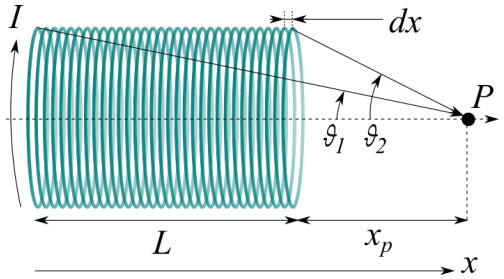

Figure 2.6: N-turns coil

To calculate the B generated by a coil with N turns it is necessary to integrate over all the loops and with the enclosed current I_{enc}. The length of the coil L adds up to the generic distance x_p from the point P. By dividing the coil into an infinitesimal length dx, the total current I_{tot} in the solenoid is related to the one I in each section (Richmond 2017), that is

$$I_{tot} = I(ndx) \tag{2.15}$$

These considerations change the eq. (2.14) into

$$dB = \frac{\mu_0 I n dx}{2} \frac{R^2}{\left[R^2 + \left(x_p + x\right)^2\right]^{\frac{3}{2}}} \tag{2.16}$$

where $x \in [0, L]$. By integrating

$$B = \int_0^L \frac{\mu_0 I n dx}{2} \frac{R^2}{\left[R^2 + \left(x_p + x\right)^2\right]^{\frac{3}{2}}} = \frac{\mu_0 I n R^2}{2} \int_0^L \frac{\mathrm{d}x}{\left[R^2 + \left(x_p + x\right)^2\right]^{\frac{3}{2}}} \tag{2.17}$$

The integration is simplified with a change in the integration variable in the right-hand side (rhs), $\mathcal{X} = (x_p + x)$, that implies $d\mathcal{X} = dx$. Therefore

$$\begin{aligned} B &= \frac{\mu_0 I n R^2}{2} \int_{x_p}^{x_p+L} \frac{\mathrm{d}\mathcal{X}}{\left(R^2 + \mathcal{X}^2\right)^{\frac{3}{2}}} \\ &= \frac{\mu_0 I n R^2}{2} \left[\frac{\mathcal{X}}{R^2 \left(R^2 + \mathcal{X}^2\right)^{\frac{1}{2}}} \right]_{x_p}^{x_p+L} \\ &= \frac{\mu_0 I n}{2} \left[\frac{x_p + L}{\sqrt{R^2 + (x_p + L)^2}} - \frac{x_p}{\sqrt{R^2 + x_p^2}} \right] \end{aligned} \tag{2.18}$$

2.3 Lorentz force

The force exerted on a moving electric charge by the effect of an electromagnetic field is known as Lorentz force $\boldsymbol{F}_L$. The two eqs. (2.3, 2.7) found in the preceding paragraphs have been deduced separately but, in general, electric and magnetic phenomena are only apparently independent.

$$\boldsymbol{F}_L = q\,(\boldsymbol{E} + \boldsymbol{v} \wedge \boldsymbol{B}) \tag{2.19}$$

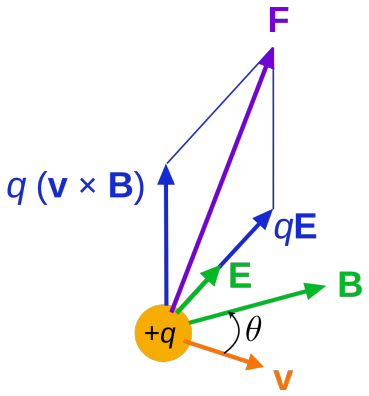

Figure 2.7: Lorentz force - particle trajectory

The interaction of the two fields accelerates the charge parallel to the electric field, concordant if positive and discordant if negative, and perpendicularly to both the magnetic field and the charge velocity vector. It follows that there is no magnetic interaction if the charge motion is parallel to the magnetic field lines.

If the cross product in (2.19) does not cancel out, then the particle is curved in its motion. In particular, the acceleration given from the $\boldsymbol{E}$-field is called tangent acceleration, as it acts in the motion direction. The one from the $\boldsymbol{B}$-field is called, instead, normal, since it changes the velocity direction but not its module. It follows that the force exerted by the magnetic field does no work, always acting perpendicularly to the motion.

Lorentz's force has a fundamental historical significance so that some textbooks use it to define directly electric and magnetic fields. For example, Jackson (Jackson 1998) treats E as an entity proportional to Lorentz's force per charge unit, as well as defines B numerically proportional to the force per current unit.

2.4 Magnetic levitation

The concept of magnetic levitation would be very relevant in this discussion. The entire MD chosen, as will be seen, will exploit this physical phenomenon to avoid sliding contacts and frictions, as well as to optimize the ability to aim at launch.

A first basic formulation, which requires numerous iterative convergence studies to obtain reliable results on stability (Wang et al. 1997), is given by

$$B\frac{dB}{dr} = \mu_0 \varrho \frac{g}{\chi} \tag{2.20}$$

where χ is the magnetic susceptivity.

Nevertheless, this study would have required more time to be conducted in depth and conscientiously, and therefore it was assumed that magnetic levitation existed and was controlled, and it was assumed that the payload at launch was perfectly stable. The various insights into the stability and magnetic oscillations in levitation will be addressed in another context.

2.5 Maxwell Equations

The $\boldsymbol{E}$-field and $\boldsymbol{B}$-field equations are not truly separated. The variation in time of one field causes a change in the other, and viceversa. These interactions are described in the four Maxwell's equations, which provide a complete description of electromagnetic phenomena up to the subatomic scale in the framework of the classic electromagnetism. This set of equations, composed by two vectorial omogeneous formulations and two scalar ones, is a unified formulation and extension of electromagnetism laws previously proposed in Gauss' law, for the $\boldsymbol{E}$-field, and in Faraday-Neumann-Lenz's law of induction. These equations are presented below both in differential and integral form

$$\begin{cases} \nabla \cdot \boldsymbol{E} = \dfrac{\rho}{\varepsilon_0} & \oiint_{\partial\Omega} \boldsymbol{E} \cdot \mathrm{d}S = \dfrac{1}{\varepsilon_0} \iiint_{\Omega} \rho \, \mathrm{d}V \quad (2.21a) \\ \nabla \cdot \boldsymbol{B} = 0 & \oiint_{\partial\Omega} \boldsymbol{B} \cdot \mathrm{d}S = 0 \quad (2.21b) \\ \nabla \wedge \boldsymbol{E} = -\dfrac{\partial \boldsymbol{B}}{\partial t} & \oint_{\partial\Sigma} \boldsymbol{E} \cdot \mathrm{d}\ell = -\dfrac{d}{dt} \iint_{\Sigma} \boldsymbol{B} \cdot \mathrm{d}S \quad (2.21c) \\ \nabla \wedge \boldsymbol{B} = \mu_0 \left(\boldsymbol{J} + \varepsilon_0 \dfrac{\partial \boldsymbol{E}}{\partial t} \right) & \oint_{\partial\Sigma} \boldsymbol{B} \cdot \mathrm{d}\ell = \mu_0 \iint_{\Sigma} \boldsymbol{J} \cdot \mathrm{d}S + \mu_0 \varepsilon_0 \dfrac{d}{dt} \iint_{\Sigma} \boldsymbol{E} \cdot \mathrm{d}S \quad (2.21d) \end{cases}$$

eq. (2.21a) is Gauss' law and states that electric charges produce $\boldsymbol{E}$-fields, and the electrix flux of these fields passing through a given area $\partial\Omega$ is proportional to the electric charge density ρ contained within.

eq. (2.21b) is Gauss' law of magnetism. In analogy with the previous one, it states that the magnetic flux passing through a closed surface $\partial\Omega$ is equal to zero[2]. In other words, it states that magnetic monopoles do not exist, or that $\boldsymbol{B}$-fields are solenoidal vector fields.

eq. (2.21c) is Maxwell-Faraday-Lenz equation, or Faraday's law of induction. It states that a change in time of a magnetic flux through a surface enclosed by a loop induces an electromotive force (EMF)[3] in the closed loop itself. The negative sign is fundamental: the current induced by the induced EMF creates a self-induced $\boldsymbol{B}_{ind}$-field that overlaps the external one and opposes itself to such flux variation.

eq. (2.21d) is known as Ampère-Maxwell circuital law and it states that every current flux or variable electrical flux through a closed surface produces a proportional circulating $\boldsymbol{B}$-field around any path that bounds that surface. For example, this is what happens in a wire in which current flows, as shown in Fig. 2.2.

[2]Since divergence is by definition the tendency of a field to "flow" away from a point more than towards it, "emptying" the source itself, and since all $\boldsymbol{B}$-field lines are closed and always flow again from the same source, the divergence of $\boldsymbol{B}$-fields must be always zero.

[3]Since the electric current is defined as charges moving through a circuit, and given that an $\boldsymbol{E}$-field is able to accelerate charges, then an induced $\boldsymbol{E}$-field may act as a current generator, creating an EMF.

2.6 Elementary circuitry

Electrical circuits are composed by electrical elements linked together. The current I and the voltage V are the two principal variables, from which the power P can be defined. The current is related to the number of electric charges that flow in a conductor over time

$$I(t) = \lim_{\Delta t \to 0} \frac{\Delta q}{\Delta t} = \frac{dq}{dt} \tag{2.22}$$

The instantaneous current is constant between any two uninterrupted wire points: this is a consequence of the principle of conservation of the charge. Each charge has energy, and the potential V is the energy per unit of charge required to move that charge

$$V = \frac{\Delta W}{q} \tag{2.23}$$

Both eqs. (2.22, 2.23) are linked together in the power formulation, namely

$$P(t) = \lim_{\Delta t \to 0} \frac{\Delta W}{\Delta t} = \frac{dW}{dt} = \frac{V dq}{dt} = V(t)I(t) \tag{2.24}$$

2.6.1 Resistive circuit

All materials, except for superconductors, limit the passage of current. This resistive behaviour can be represented with an electrical resistance $R > 0$ between V and I

$$V = IR \tag{2.25}$$

The eq. (2.25) is the linear characteristic relation of circuits and it is known as Ohm's law, where R = cost. Real resistors may closely resemble this behaviour, otherwise there are variable resistors. In general the resistance R of a wire is computed as

$$R = \int_0^L \frac{\rho}{A} \, \mathrm{d}\ell \tag{2.26}$$

where A is the cross sectional area, L is the cable length and ρ is the resistivity, a characteristic value of the used material. In Table A.1, Appendix A, there is a list of resistivities of the most common materials. A first observation is that, given a potential V, the power needed P decreases with I that, in turn, decreases with high resistances. It follows

$$P(t) = V(t)I(t) = \frac{V^2(t)}{R} = RI^2(t) \tag{2.27}$$

that is, a resistor can only absorb power and thus it is a passive element that dissipates energy. The last formulation of eq. (2.27) is knows as Joule Effect (JE), or Joule's first law of heating, that is the dissipated energy in the form of heat in a circuit.

The temperature is one of the factors that can affect the Ohmic behaviour of an electric cable. The resistivity depends on the temperature according to the relationship

$$\begin{aligned} \rho &= \rho_{ref}\left[1+\alpha\left(T-T_{ref}\right)\right] \\ R &= R_{ref}\left[1+\alpha\left(T-T_{ref}\right)\right] \end{aligned} \tag{2.28}$$

where $\alpha > 0$ is the temperature coefficient of resistance, characteristic of the material, and indicates how much the resistivity ρ varies with the temperature T compared to ρ_{ref} @ $T_{ref} = 20°C$ (please refer to Appendix A, Table A.1).

The linear behaviour of eq. (2.28) is valid in a great range, especially for high temperatures . At temperatures below 100 K, in which quantum phenomena are predominant, the resistivity tends to settle asymptotically at a constant value called residual resistivity ρ_0, function of the residual resistivity ratio (RRR), the ratio between the resistivity at 273 K and the one close to the liquid helium condition, at 4 K.

In this document $T \geq 90$ K (Stoica et al. 2016; Sefton-Nash et al. 2017). Therefore, the charges residual mobility at very low temperatures can be neglected and the eq. (2.28) will suffice. The Material Properties DataBase (MPDB) software (JAHM Software, Inc. 1998) is used to extract discrete data points to be interpolated, as shown in Appendix A, Table A.6. This operation will prove particularly useful in considering the initial condition in the lunar Extreme Environment (EE), at ambient temperatures of 90.15 K.

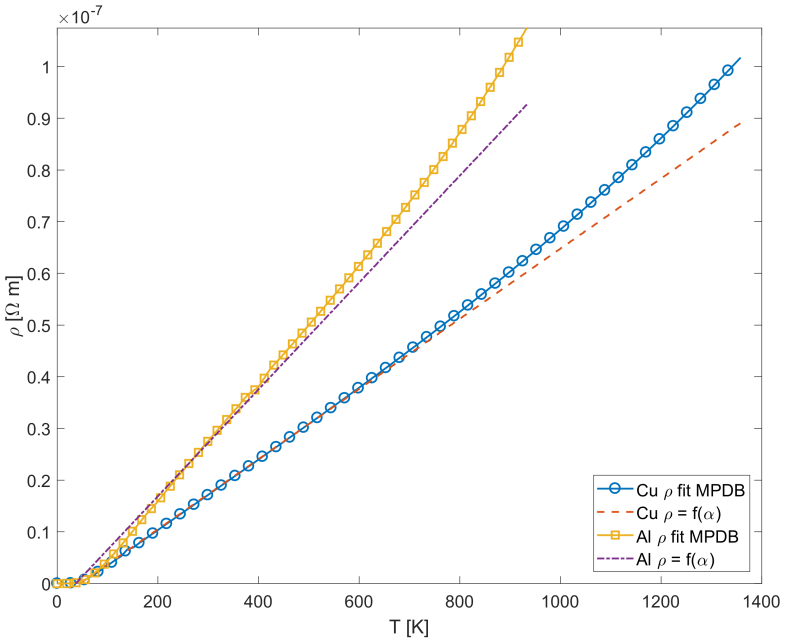

Figure 2.8: Resistivity ρ variation wrt temperature T for Cu and Al

Numerical interpolation or the use of the eq. (2.28) prove to be almost coincident for a wide range –excluding at most the lower and upper temperature limits–, as can be clearly seen in Fig. 2.8 and, therefore, the computationally lighter method can be used.

Capacitors

The relation between current and potential in a capacitor is linear

$$I(t) = C\frac{dV(t)}{dt} \tag{2.29}$$

where $C > 0$ is the capacity. The capacitors, in the most schematic version, are devices with two or more parallel conductive plates separated by a dielectric material. The material choice, as well as the geometrical characteristics of the capacitor, directly affect the capacity

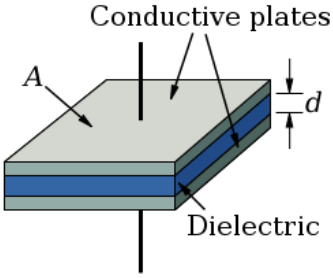

Figure 2.9: Capacitor scheme

$$C = k\varepsilon_0\frac{A}{d} \tag{2.30}$$

Where A is the plate area, d is the distance between plates, and k is the material dielectric constant (Appendix A, Table A.2). The capacity has typical values of $C \in [10^{-12}, 10^{-3}]\,\mathrm{F}$.

The instantaneous power P of the capacitor is, in analogy to eq. (2.27),

$$P(t) = V(t)I(t) = V(t)C\frac{dV(t)}{dt} \tag{2.31}$$

The maximum energy $\mathcal{E}_c$ that can be stored by a capacitor is function of both the potential V and the capacity C and is equal to

$$\mathcal{E}_c = \int_0^t P(t)\ \mathrm{d}t = \frac{1}{2}CV^2 \tag{2.32}$$

In this analysis the capacitors will be considered as entities defined *a priori* and will not be analyzed in detail, specifically for their ability to instantaneous discharge the current or for what concerns energy conservation. This analysis is certainly relevant and should be addressed in subsequent studies.

Inductors

The inductor is a linear circuit component characterized by the following differential relation between the potential and the current

$$V(t) = L\frac{dI(t)}{dt} \tag{2.33}$$

Where $L > 0$ is the inductance. A more detailed physical explaination is that the inductance L is a property of a conductor by which a current variation induces an EMF and it measures how strongly a circuit opposes to the current change. Indeed, another definition for the inductance is that it is the costant of proportion between the current over time in the circuit and the magnetic flux induced by the current itself, that is

$$\Phi_B(t) = \int_S \boldsymbol{B}(t) \cdot \mathrm{d}\boldsymbol{S} = LI(t) \tag{2.34}$$

A variabile current over time induces a magnetic field that opposes the change that produced itself, as stated in Lenz's law. This statement is reflected in Faraday's law of induction, eq. (2.21c), in the negative sign that expresses also the energy conservation principle. Therefore

$$\mathcal{E} = -\frac{d\Phi_B}{dt} \tag{2.35}$$

The explicit calculation of the inductance L for generic geometries, especially in closed form, has been the subject of numerous studies over the last few decades (Maxwell 1892a; Langford-Smith 1952; Smythe 1989; Rosa and Grover 2016). Later in the Chapter will be presented particular cases that allow approximate resolution in closed form for specific geometries.

The inductor is able to absorb istantaneous power equal to

$$P(t) = V(t)I(t) = L\frac{dI(t)}{dt}I(t) \tag{2.36}$$

Therefore, the maximum energy absorbed over time $\mathcal{E}_i$ by the inductor is equal to

$$\mathcal{E}_i = \int_0^t P(t)\ \mathrm{d}t = \frac{1}{2}LI^2 \tag{2.37}$$

Like the capacitors, the inductive components are also taken "as they are". It should be noted that these will be analyzed more thoroughly for what concerns their self-inductance and mutual-inductance: refer to Section 2.8, Paragraph 2.8.1, for more details.

2.6.2 Dynamic circuit

Dynamic circuits have a differential characteristic between potential V and current I, while resistive circuits have an istantaneous V-I bond. The two electrical components just analyzed are dynamic and they are able to store energy but never to dissipate it[4].

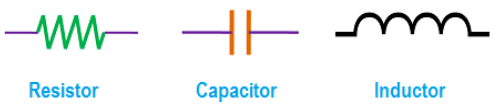

Figure 2.10: Circuit passive components

The behaviour of dynamic circuits is usually described by a differential equation. There are first and second order circuits, depending on whether there is only one dynamic component, capacitor or inductor, or both. The study of these circuits is beyond the scope of the analysis, even if a detailed description can be found in various existing books, for example (Hambley 2009; Perfetti 2012).

Nonetheless, it is worth the effort to emphasize the importance of the time constant τ in the two circuits. In general, the solution for the variable x in a first order circuit is

$$x(t) = \left[x(0) - x(\infty)\right] e^{-\frac{t}{\tau}} + x(\infty) \tag{2.38}$$

Where

$$\tau = RC \qquad\qquad \tau = \frac{L}{R} \tag{2.39}$$

respectively for a RC and a LR circuit. For a discrete t step, it is possible to notice that, regardless of the initial $x(0)$ value, when $t \geq 5\tau$ the solution approaches asymptotically $x(\infty)$. In other words, after approximately 5 constants of time it can be said that the transient is finished and the solution is nearly costant. The τ constant is also the inverse of the decay rate: low τ values correspond to a very rapid decay, and vice versa.

In the resolution of Non Linear (NL) Ordinary Differential Equation (ODE) system the time constants will not be directly computed, but these information become useful for correctly instructing the optimizer in order to understand in which direction it should proceed to find the solution.

Therefore, qualitatively the resistance, capacity, and inductance values will strongly affect the current and potential evolution in a circuit over time.

[4] This is strongly verified in the ideal case, whereas in the real one there are minimal dissipations.

2.6.3 Circuits in sinusoidal regime

Both current I and potential V can exist in a sinusoidal form, the so called alternate current (AC) regime. A generic sinusoidal variable corresponds to the function

$$x(t) = A\cos(\omega t + \vartheta) \tag{2.40}$$

Where $A > 0$ is the wave amplitude, or peak value, $\omega > 0$ the angular frequency, ϑ the phase. ω is related to the period T and, therefore, to the frequency f as

$$T = \frac{2\pi}{\omega}, \quad f = \frac{1}{T} \quad \Longrightarrow \quad \omega = \frac{2\pi}{T} = 2\pi f \tag{2.41}$$

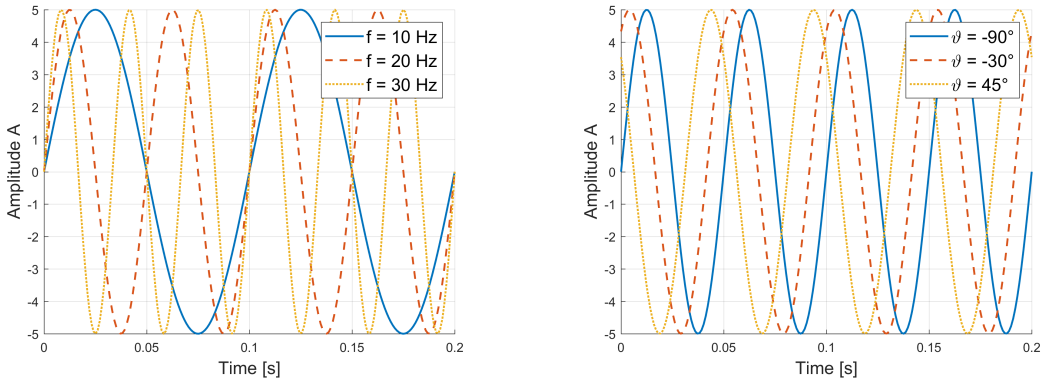

Figure 2.11: Sinusoidal waves with different frequency f (left) and different phase ϑ (right)

In Fig. 2.11 there are the effects on the waves by a change in different parameters. Three waves with the same amplitude A have different frequencies f and same phase ϑ, on the left, and viceversa on the right. A different phase corresponds to a function translation with respect to the base $A\cos(\omega t)$ cosinusoidal function. A frequency variation, instead, implies a greater or smaller pulse in the same unit of time.

Specifically, by defining I_m and V_m as the peak current and potential, and ϑ_V and ϑ_I the respective phases, the eq. (2.40) becomes

$$\begin{aligned} V(t) &= V_m\cos(\omega t + \vartheta_V) \\ I(t) &= I_m\cos(\omega t + \vartheta_I) \end{aligned} \tag{2.42}$$

A generic resistive element absorbs over time a power $P(t)$ equal to

$$P(t) = V(t)I(t) = V_m\cos(\omega t + \vartheta_V)I_m\cos(\omega t + \vartheta_I) \tag{2.43}$$

A prostaferesis trigonometric trasformation allows expressing eq. (2.43) as

$$P(t) = \frac{1}{2}V_mI_m\cos(\vartheta_V - \vartheta_I) + \frac{1}{2}V_mI_m\cos(2\omega t + \vartheta_V + \vartheta_I) \tag{2.44}$$

Where the first term is constant and is called active power, or mean power, $\hat{P}$

$$\hat{P} = \frac{1}{2} V_m I_m \cos(\vartheta_V - \vartheta_I) \tag{2.45}$$

This value is the one around which the istantaneous power $P(t)$ oscillates over time. The peak pover P_m, that is the maximum power that can be requested instantly, is given by the sum of the active $\hat{P}$ and half-oscillation power, i.e.

$$P_m = P + \frac{1}{2} V_m I_m \tag{2.46}$$

In the specific case of a resistor, instantaneous and mean power, eqs. (2.44, 2.45), are

$$\begin{aligned} P(t) &= \frac{1}{2} R I_m^2 + \frac{1}{2} R I_m^2 \cos(2\omega t + 2\vartheta_I) \\ \hat{P} &= \frac{1}{2} V_m I_m = \frac{1}{2} R I_m^2 \end{aligned} \tag{2.47}$$

The Root-Mean-Squared (RMS) voltage (or Current), is defined as the amount of sinusoidal Voltage that has the same power as an equivalent constant voltage. By definition, the RMS or effective value of a function is the square root of the arithmetic mean of the square values or, if the function is continuous, the integral over the whole domain. In the case of a sinusoidale waveform the domain is the period T, and therefore

$$x_{eff} = \sqrt{\frac{1}{T} \int_0^T x_m^2 \cos^2(\omega t) \, \mathrm{d}t} \tag{2.48}$$

By integrating it is obtained

$$x_{eff} = \frac{x_m}{\sqrt{2}} \tag{2.49}$$

with $x = \{V_m, I_m\}$. By substituting eq. (2.49) into the mean power expression, the $\frac{1}{2}$ factor disappears and it results

$$\hat{P} = V_{eff} I_{eff} \cos(\vartheta_V - \vartheta_I) = R I_{eff}^2 \tag{2.50}$$

or any equivalent formulation obtained with Ohm's law, eq. (2.25).

Chirp

A chirp is a sweep signal in which the frequency changes over time (Easton 2010). It is known as up-chirp if the frequency increases over time, down-chirp if it decreases. A generic sinusoidal variable would appear as

$$x(t) = A\cos\big(\vartheta(t)\big) \tag{2.51}$$

where $\vartheta(t)$ is the instantaneous phase and is function of the instantaneous frequency $f(t)$. The simplest case is given by a linear chirp in which the frequency varies linearly over time from an initial value f_0 to a final f_1 in a time t_s, the sweep time. The instantaneous frequency, also related to the phase change over time, becomes

$$f(t) = f_0 + \frac{f_1 - f_0}{t_s}t \qquad\qquad f(t) = \frac{1}{2\pi}\frac{d\vartheta(t)}{dt} \tag{2.52}$$

By integrating the eq. (2.52) it results a quadratic-phase signal

$$\vartheta(t) = 2\pi\left(f_0 t + \frac{f_1 - f_0}{2t_s}t^2\right) + \vartheta_0 \tag{2.53}$$

where ϑ_0 is the classic phase shift shown already in eq. (2.40). Therefore, a chirp signal has a sinusoidal function that appears like the following

$$x(t) = A\cos\left[2\pi\left(f_0 t + \frac{f_1 - f_0}{2t_s}t^2\right) + \vartheta_0\right] \tag{2.54}$$

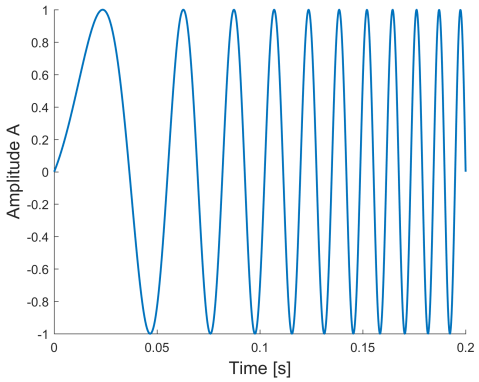

Figure 2.12: Sinusoidal chirp: $\vartheta_0 = -90°$, $f_0 = 5$ Hz, $f_1 = 100$ Hz, $t_s = 0.2$ s

The EML that will be illustrated in the concluding Chapters will use a chirp signal to generate the magnetic field necessary to accelerate the payload. However, a spatial rather than a temporal analysis will be preferred, and therefore the sinusoidal pulses of the current will be at constant frequency in space. It is implied that, since the payload accelerates in space, this configuration will result in a chirp signal over time, which however will be a result of the spatial analysis and not an input signal.

2.7 Reluctance and magnetic saturation

Reluctance $\mathcal{R}$, also known as magnetic resistance, defines how much a magnetic flux can penetrate inside a solid: the more the reluctance value is high, the more the flow is "reluctant" to pass through it. Indeed, its inverse is called permeance $\mathcal{P}$. The most general formulation is known as Hopkinson's law and it states

$$\mathcal{R} = \frac{\mathcal{F}}{\Phi} \tag{2.55}$$

where $\mathcal{F}$ is the magnetomotive force (MMF) and Φ is the magnetic flux. In a uniform magnetic field, reluctance is expressed in closed form by the following relation (Sears 1958)

$$\mathcal{R} = \frac{\ell}{\mu_0 \mu_r A} \tag{2.56}$$

where ℓ is the length of the magnetic path, μ_0 is the vacuum permeability, μ_r is the relative magnetic permeability of the material, and A is the cross-sectional area of the area in which the flux enters (please refer to Appendix A, Table A.3). The product between μ_0 and μ_r, μ, is the material magnetic permeability.

Magnetic permeability is a strongly NL proportionality coefficient wrt Φ. For weak magnetic fluxes it exists a linear relationship between $\boldsymbol{H}$ and $\boldsymbol{B}$

$$\boldsymbol{B} = \mu \boldsymbol{H} \tag{2.57}$$

where H represents how much the B field can influence the reorientation of the dipoles. The magnetic saturation phenomenon shows that there is a magnetic field intensity value beyond which the $H - B$ relationship becomes NL.

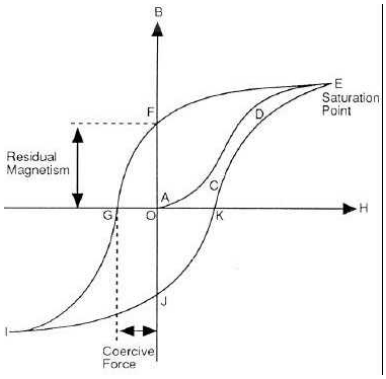

Figure 2.13: Hysteresis $H - B$ cycle

If the applied magnetic field intensity H is strong enough, the material incurs in the saturation, that is, the B field is no longer able to increase the magnetization of the medium. Saturation is a characteristic of ferromagnetic materials.

What has been said outlines an important consequence: if the magnetic fields involved in the EML are intense, it will not be possible to use ferromagnetic cores due to their saturation, and different solutions will have to be chosen.

2.8 Mutual inductance calculations

2.8.1 Mutual inductance of coaxial circular filaments

Mutual inductance is the inductance between two separate circuits that evaluates how a magnetic field, generated by a circuit, exerts an electromotive force on the other circuit, thus inducing a current by Faraday's law of induction, eq. (2.21c).

The term "mutual" underlines that, once the geometric characteristics of two circuits are fixed, a certain variation of current in a circuit causes an electromotive force in the other, as well as the same variation of current in the second circuit would cause the same electromotive force in the first one.

There are various semi-empirical methods for the calculation of mutual (and self) inductances. The tabular method is often referred as the faster but the less accurate, around zeroth and first order. The Grover's method mainly refers to the geometric characteristics of the two coaxial coils and often uses tabular approximations to be interpolated for lookup values that fall between those presented. A formulation provided by Grover for the mutual inductance M (in μH) between two coaxial circular filaments of radii a and A, and spaced apart by a distance d, is (Rosa and Grover 2016)

$$M = f\sqrt{Aa} \tag{2.58}$$

in which the value of f has to be found in Grover's table through the lookup parameter k^2

$$k^2 = \frac{(A-a)^2 + d^2}{(A+a)^2 + d^2} \tag{2.59}$$

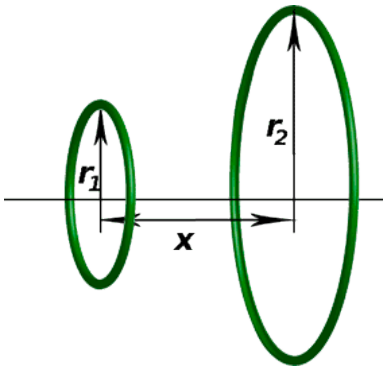

Figure 2.14: Two coaxial circular filaments

It is possible to validate the eq. (2.58) by means of an analytical analysis. Consider two circular filaments c_1 and c_2 in Fig. 2.14 with radii r_1 and r_2 and spaced apart by a distance x. The coil paths are s_1 and s_2, respectively, and the whole circumferences have angle parameters ϑ_1 and ϑ_2. The mutual inductance M between the two circuits is given by the double integral Neumann's formula (Nalty 2011)

$$M = \frac{\mu_0}{4\pi} \oint_{c_1} \oint_{c_2} \frac{\mathrm{d}\boldsymbol{s}_1 \cdot \mathrm{d}\boldsymbol{s}_2}{|\boldsymbol{r}|} \tag{2.60}$$

The generic distance r between two points in the two coils is

$$r = \sqrt{r_1^2 + r_2^2 + x^2 - 2r_1 r_2 \cos(\vartheta_2 - \vartheta_1)} \tag{2.61}$$

while the two paths are

$$\begin{aligned} \mathrm{d}\boldsymbol{s_2} &= r_2\left(-\sin\vartheta_2 \hat{a}_x + \cos\vartheta_2 \hat{a}_y\right) d\vartheta_2 \\ \mathrm{d}\boldsymbol{s_1} &= r_1\left(-\sin\vartheta_1 \hat{a}_x + \cos\vartheta_1 \hat{a}_y\right) d\vartheta_1 \\ \mathrm{d}\boldsymbol{s}_1 \cdot \mathrm{d}\boldsymbol{s}_2 &= r_1 r_2 \left(\sin\vartheta_1 \sin\vartheta_2 + \cos\vartheta_1 \cos\vartheta_2\right) d\vartheta_1 d\vartheta_2 \\ &= r_1 r_2 \cos(\vartheta_2 - \vartheta_1) d\vartheta_1 d\vartheta_2 \end{aligned} \tag{2.62}$$

By substituting eqs. (2.61, 2.62) into eq. (2.60)

$$M = \frac{\mu_0}{4\pi} \oint_{\vartheta_1} \oint_{\vartheta_2} \frac{r_1 r_2 \cos(\vartheta_2 - \vartheta_1) d\vartheta_1 d\vartheta_2}{\sqrt{r_1^2 + r_2^2 + x^2 - 2r_1 r_2 \cos(\vartheta_2 - \vartheta_1)}} \tag{2.63}$$

By applying a variable change

$$\gamma = \vartheta_2 - \vartheta_1 \implies d\gamma = d\vartheta_2 \tag{2.64}$$

Therefore

$$\begin{aligned} M &= \frac{\mu_0}{4\pi} \oint_{\vartheta_1} \oint_{\gamma} \frac{r_1 r_2 \cos\gamma d\vartheta_1 d\gamma}{\sqrt{r_1^2 + r_2^2 + x^2 - 2r_1 r_2 \cos\gamma}} \\ &= \frac{\mu_0}{4\pi} \oint_{\vartheta_1} d\vartheta_1 \oint_{\gamma} \frac{r_1 r_2 \cos\gamma d\gamma}{\sqrt{r_1^2 + r_2^2 + x^2 - 2r_1 r_2 \cos\gamma}} \\ &= \frac{\mu_0}{2} \oint_{\gamma} \frac{r_1 r_2 \cos\gamma d\gamma}{\sqrt{r_1^2 + r_2^2 + x^2 - 2r_1 r_2 \cos\gamma}} \end{aligned} \tag{2.65}$$

The integral contained in eq. (2.65) has a known solution by means of elliptic functions K and E. The reference solution is

$$\oint_{\vartheta} \frac{\cos\vartheta \ \mathrm{d}\vartheta}{\sqrt{a - b\cos\vartheta}} = \frac{4\sqrt{a+b}}{b}\left[\left(1 - \frac{\beta^2}{2}\right)K(\beta) - E(\beta)\right] \tag{2.66}$$

where

$$\begin{aligned} \beta &= \sqrt{\frac{2b}{a+b}} \\ K(\beta) &= \int_0^{\frac{\pi}{2}} \frac{\mathrm{d}\vartheta}{\sqrt{1 - \beta^2 \sin^2\vartheta}} \\ E(\beta) &= \int_0^{\frac{\pi}{2}} \sqrt{1 - \beta^2 \sin^2\vartheta} \ \mathrm{d}\vartheta \end{aligned} \tag{2.67}$$

Therefore the values in eq. (2.65) corresponding to those in eq. (2.66) are

$$\begin{aligned} a &= \frac{r_1^2 + r_2^2 + x^2}{r_1^2 r_2^2} \\ b &= \frac{2}{r_1 r_2} \end{aligned} \tag{2.68}$$

By joining eqs. (2.65, 2.66, 2.67, 2.68) it is obtained

$$M = 2\mu_0 \frac{\sqrt{a+b}}{b} \left[\left(1 - \frac{\beta^2}{2} \right) K(\beta) - E(\beta) \right] \tag{2.69}$$

By comparing the results obtained from the eq. (2.69), deduced by analytical means (Nalty 2011), with those derived from the tabulations given by Grover (Rosa and Grover 2016), it can be concluded that the analytical model is confirmed with very coincident results.

2.8.2 Mutual inductance of finite coaxial single-layer coils

Calculations of mutual inductances for finite coils, i.e. not approximable to the ideal solenoid model, have always been complex, sometimes for the accuracy, sometimes for the inapplicability of a certain formulation for particular geometries.

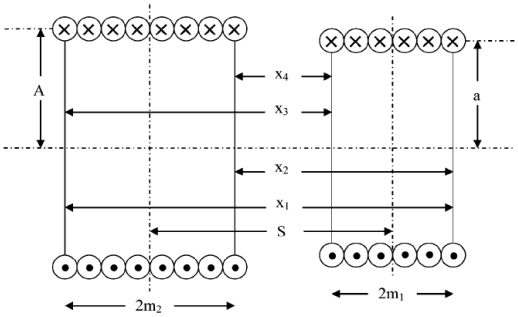

Figure 2.15: Geometry for the mutual inductance of two single-layer coils

Recent studies (Engel and Rohe 2006; Engel and Mueller 2009) have analyzed the computation time and precision of mutual inductance calculation through finite element methods, analytical integration and tabular methods. Also in this case there is a closed form formula that evaluates the mutual inductance M (Rosa and Grover 2016) as

$$M = 0.002\pi^2 a^2 n_1 n_2 \left(r_1 B_1 - r_2 B_2 - r_3 B_3 + r_4 B_4\right) \cdot 10^{-6} \tag{2.70}$$

Where a and A are respectively the radius of the smaller and the bigger coil, n_1 and n_2 are the winding densities, and the r_n values are the diagonal lengths calculated as

$$r_n = \sqrt{A^2 + x_n^2} \qquad n = 1,2,3,4 \qquad \begin{cases} x_1 = s + (m_1 + m_2) \\ x_2 = s + (m_1 - m_2) \\ x_3 = s - (m_1 - m_2) \\ x_4 = s - (m_1 + m_2) \end{cases} \tag{2.71}$$

The total number of wire turns N is directly proportional to m –and, therefore, to the length l of the coil– and to the winding density n, i.e.

$$2mn = N \qquad \text{where } 2m = l \tag{2.72}$$

The B_n values, instead, are derived from the lookup table provided by Grover. The lookup parameters, both ranging from 0 to 1, are

$$\rho_n = \frac{A^2}{r_n^2} \qquad \alpha = \frac{a}{A} \tag{2.73}$$

Grover provides two different tables. The first has a 0.05 spacing for both ρ_n and α values, the second has a finer granulation of 0.01 for $\rho_n^2 \geq 0.9$, $\alpha \geq 0.9$. The main problem with

this method is that any lookup parameter that does not coincide with those in the tables must be interpolated. It has been shown in the recent studies that for $\rho \to 1$, $\alpha \to 1$, errors can be as much big as $5 - 10\%$, especially if the distance s is small. These approximation errors can be reduced by tightening the table values, thus reducing the granularity.

Nonetheless, a great precision, compared to those values obtained via empirical experiments, is obtained by using Finite Element Method (FEM) or analytical methods.

Analytical computations involve solving elliptic integral of the first and second kind. To date, these elliptical integrals can be solved with the most popular computational softwares by numerical convergence or series expansion equivalent formulations. Such alternative methods of calculation may diverge for particular geometries (Maxwell 1892b), explaining recent studies attempts to make tabular methods more precise.

A further analysis shows how calculations made using finite elements are wholly comparable with analytical ones, and both have the lowest error. It may be agreed that for a preliminary analysis it suffices to use analytical formulation in place of FEM. Moreover, FEM analyses have shown to execute more than a thousand time slower than tabular methods. On the other hand, as much as Grover tables can be refined, there are always errors deriving from lookup parameters interpolation.

An elegant yet effective solution could be to change the evaluation of the B_n terms, Clem coefficients, in eq. (2.70), that is, not to get them tabulated but evaluated analytically. This method is implemented in a recent research (Engel and Rohe 2006). Using the eq. (2.73) it can be obtained

$$B_n = \frac{2}{\pi} \int_0^{\pi} \sin^2 \varphi \frac{\sqrt{1 + \alpha^2 \rho_n^2 - 2\alpha \rho_n^2 \cos \varphi}}{1 + \alpha^2 - 2\alpha \cos \varphi} \mathrm{d}\varphi \tag{2.74}$$

With this information, it is immediately possible to obtain the pattern of the mutual inductance and its gradient as the distance between the centers of the two coils varies.

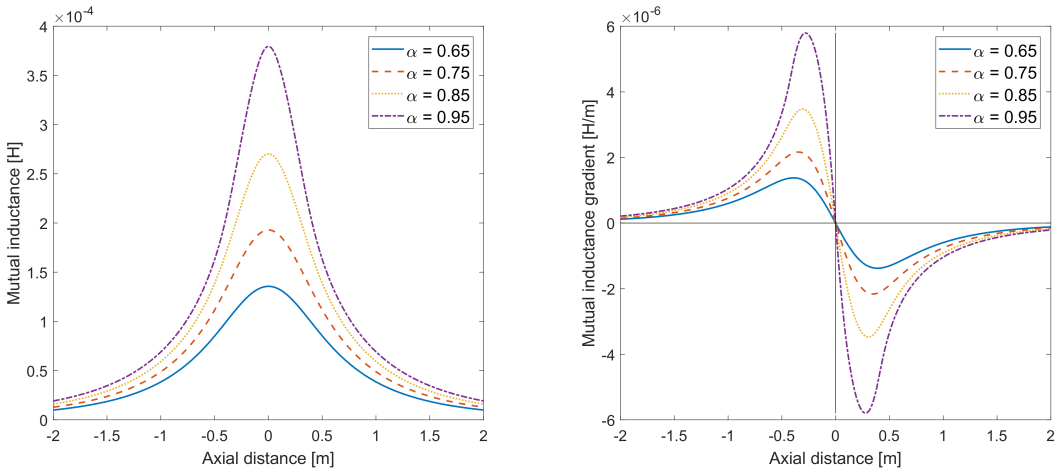

Figure 2.16: Mutual inductance M and its gradient $dM_{,x}$ as function of α

In Fig. 2.16, in which the drive coil is centered in $x = 0$, it is possible to appreciate the increase of mutual inductance, of its gradient and, hence, of the force exerted on the bucket, when $\alpha \to 1$, that is, when the radii of the two coils are similar.

2.8.3 Mutual- and self-inductance of multi-layer coils

If it is necessary to use more than one radial layer of wire windings, it may be more appropriate to use a spatial FEM discretization. This new approach is taken up by recent studies (Akyel and Babic 2007) and is accurate, robust, and fast for small mesh sizes.

This method is based on the Maxwell's coils analyzed in Paragraph 2.8.1. A coil with n_l radial wire layers and N turns in the axial direction will have a total of $n_l N$ windings; if these are sufficiently close to each other, namely if there are few empty spaces[5], it is possible to suppose that a coil section is rectangular, with dimensions l and h, respectively axial span and height. The FEM approach divides the rectangle into small portions and computes the self- and mutual inductances for both the coils. The total contribution will be superimposed on each single contribution of the filament.

Altough this method has a quick execution, its integration over space is computationally expensive and is avoided in this preliminary study. To consider the increase in total windings N for a multilayer coil, reference will be made to eq. (2.70) by expressing the winding densities as ratio between the total number of windings and the length of the coil, namely

$$M = 0.002\pi^2 a^2 \frac{N_1 n_{l1}}{l_1} \frac{N_2 n_{l2}}{l_2} \left(r_1 B_1 - r_2 B_2 - r_3 B_3 + r_4 B_4\right) \cdot 10^{-6} \tag{2.75}$$

or alternatively

$$M = 0.002\pi^2 a^2 n_1 n_2 \left(r_1 B_1 - r_2 B_2 - r_3 B_3 + r_4 B_4\right) \cdot 10^{-6} \cdot \left(n_{l1} n_{l2}\right) \tag{2.76}$$

where n_{l1} and n_{l2} are the number of layers. As explained in (Rosa and Grover 2016), simply multiplying the single-layer formulation by the total number of layers provides values lower than the real ones. Nevertheless, it is preferred to have this numerical discrepancy because it is conservative.

Self-inductances are found through approximate analytical formulations (Langford-Smith 1952) for the same reasons. These are

$$\begin{cases} L_s \approx \dfrac{r^2 N^2}{9r + 10l} - \dfrac{crN^2}{10\pi l} & \text{if } \dfrac{l}{c} \geq 10 \\ L_s \approx \dfrac{rN^2}{13.5} \log_{10}\left(\dfrac{k_L}{\sqrt{l^2 + c^2}}\right) & \text{else, with } k_L = \begin{cases} 3.6a & \text{if } 0.35 < \dfrac{l}{c} < 1 \\ 4.02a & \text{if } 0.15 < \dfrac{l}{c} < 0.35 \\ 4.55a & \text{if } 0 < \dfrac{l}{c} < 0.15 \\ 4 & \text{else for } \dfrac{l}{r} \approx \dfrac{c}{r} \approx 0 \end{cases} \end{cases}$$

$$L = L_s + 4.951125 \cdot 10^{-3} rN \tag{2.77}$$

[5] This assumption is also function of the wire insulation radius, further analyzed in Chapter 4.

where $c = 2k_i r_w n_l$ is the thickness of the multilayer sheet, i.e. twice the radius of the wire times the number of layers. Please note that the eq. (2.77) (Langford-Smith 1952) is valid only for closely packed wires, namely wires with spacing equal to one insulated wire diameter –otherwise another corrective term has to be added–.

As shown in eq. (2.39), an increase in the self-inductance ensures a slower decay of the current in an LR circuit. Therefore, a circuit with forced current will be more efficient with low values of L, whereas a natural decaying circuit would be better with higher inductances. At the same time, the mutual inductance of two circuits would be higher as the number of layers increase. To achieve the best compromise, it is possibile to show how L, M, and its gradient $dM_{,x}$ varies with the geometrical parameters

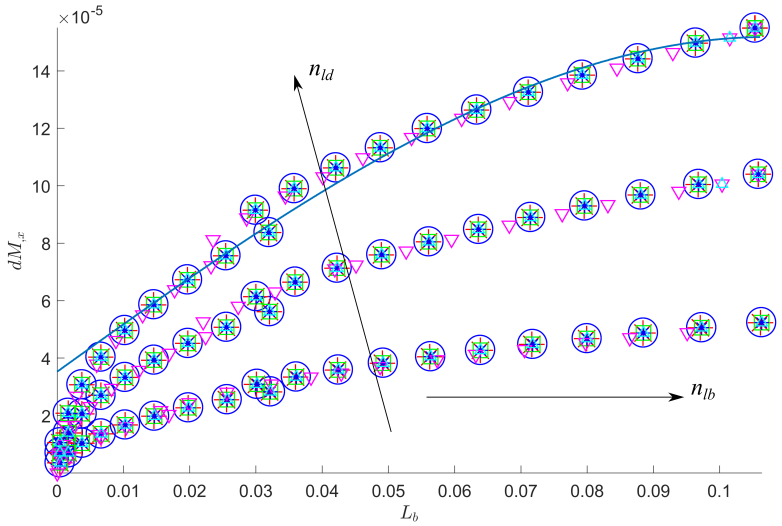

Figure 2.17: Self- and mutual inductance peak wrt number of coil layers

The results in Fig. 2.17 are obtained though optimization with different Merit Functions (MFs) f. It is clear that the mutual inductance gradient increases as the number of layers of both the bucket and the drive increase. There is also an asymptotic behaviour with increasing number of layers in the bucket only, due to the fact that the average radius r of the latter is reduced to accomodate the new layers. In decreasing size order, the matching MFs used to retrieve the values of L_b and $dM_{,x}$ are

- Blue circle, $f_{max} = L_b$;
- Red star, $f_{max} = \sum \left| dM_{,x}(x) \right|$ for $x \in [-x_i, x_i]$, where x_i is the ignition distance which will be discussed further in Chapter 8;
- Green square, $f_{max} = L_b + \sum \left| dM_{,x}(x) \right|$;
- Pink triangle, $f_{max} = \max dM_{,x}$;
- Light blue triangle, $f_{max} = L_b + \max \left(dM_{,x} \right)$.

where the difference between the two MFs for $dM_{,x}$ are the computation of only the peaks of the mutual inductance gradient or the whole area covered by the curve –which is, in particular, the effective proportional value for the force, as will be further analyzed in this dissertation–.

However, all the optimizations are sufficiently in agreement to notice a trend. Even more

clearly, as shown in the following Figures, it can be understood which parameters influence the variation of L, M, and its gradient $dM_{,x}$, including the ratio $b:d$ of bucket and drive wire layers. The following results are not optimized.

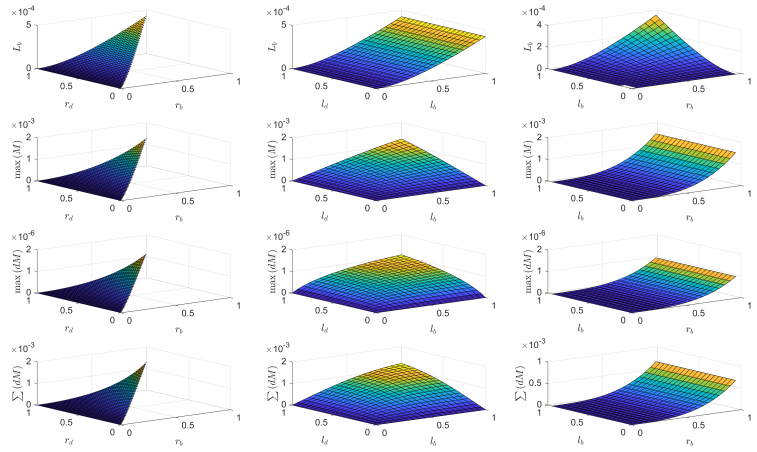

Figure 2.18: L, M, $dM_{,x}$ variation wrt geometric parameters, $1:3$ layers

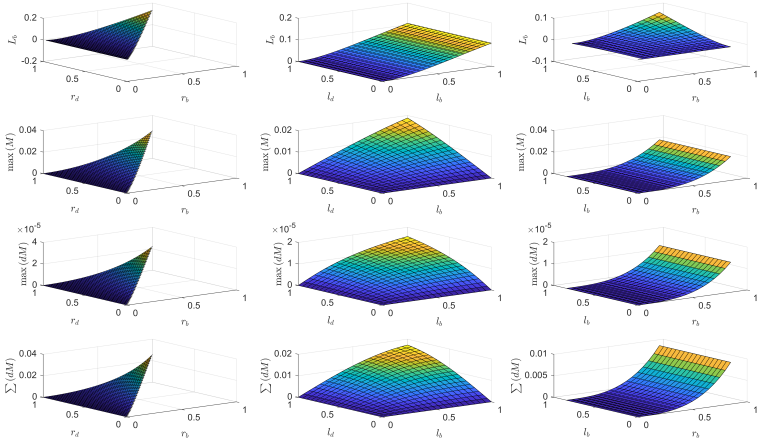

Figure 2.19: L, M, $dM_{,x}$ variation wrt geometric parameters, $20:3$ layers

In conclusion, it seems that the maximum of L and $dM_{,x}$ is obtained in first approximation by similar radii, namely $r_b \to r_d$, and for maximum bucket solenoid axial lengths –as it increases the maximum windings per layer–. Nevertheless, the combined effect is to be explored, and therefore these values are to be taken as first guess and are not definitive.

3. Mechanics

To the optimist, the glass if half full. To the pessimist, the glass is half empty. To the engineer, the glass is twice as big as it needs to be.

— Unknown

3.1 Mechanics of materials

The mechanics of materials is the engineering branch that deals with the structures resistance to different stresses and strains, which cause deformations and desplacements of the materials wrt their initial conditions. This branch is extremely wide and has the fundamental role to verify, in many engineering fields, that structures are able to withstand the loads to which they will be subjected.

The analysis can focus on an instantaneous test of material strength or a dynamic control over the time of the material's loads. In the latter case, reference is made to the fatigue behaviour and to the fracture mechanics, which deals with how and how much a crack propagates, that is, a microfracture of the material over time due to repeated loads - even well below those instantly bearable by the material - that can cause fracture.

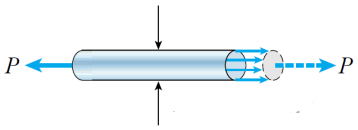

Figure 3.1: Bar in tension

In Fig. 3.1, suppose to exert a traction P on the bar with cross-sectional area A. The stress σ, supposed uniformly distributed over A, is (Gere 2003)

$$\sigma = \frac{P}{A} \tag{3.1}$$

Specifically, traction forces cause tensile stresses, while compressive ones cause compressive stresses. Conventionally, tensile stresses are the positive ones.

The bar streches due to traction. Assuming that the bar has elongated equally in each of its sections, the elongation per unit of length of the material, or strain, is

$$\varepsilon = \frac{\Delta L}{L} \tag{3.2}$$

again, dilatations are called tensile strains, compressions are defined as compressive strains.

3.1.1 Stress-strain diagrams

For a good range of stress and strain values, σ and ε have a linear relationship. Hooke's law is valid for pure traction or compression, that is, an uniaxial stress, and it states

$$\sigma = \mathcal{E}\varepsilon \tag{3.3}$$

where $\mathcal{E}$ is known as the modulus of elasticity of the material, or Young's modulus.

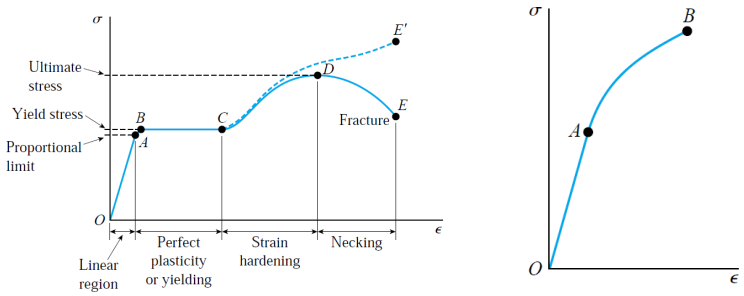

Figure 3.2: Stress-strain diagram for steel (left) and a brittle material (right) (Gere 2003)

There are a series of diagrams that relate strain and stress depending on the material.

For example, with reference to Fig. 3.2 L, there is a characteristic $\sigma - \varepsilon$ diagram of a metal. The $\overline{OA}$ tract is the proportionality section and its slope is the Young's modulus; up to this point the deformation phenomenon is reversible, that is, by releasing the load the structure re-enters in its undeformed condition[1]. By increasing the load a plastic deformation $\overline{BC}$, called yielding, is induced, with non-reversible strain. In this condition $\mathcal{E}$ becomes NL and the material has great strains with small loads up to the point in which it hardens. This process, shown in $\overline{CD}$, consists in a reorientation of the material's crystalline structure. By further increasing the load to $\sigma = \sigma_R$, the material reaches its ultimate stress condition, after which it breaks. The $\overline{DE}$ section is "apparent", because the load does not actually decrease. The region in which the fracture happens is shrinking, reducing the cross sectional area and, therefore, increasing the "apparent" load according to (3.1). In fact, the real material behaviour is represented in the dashed section $\overline{CE'}$.

A material varies its section after a traction or compression depending on the Poisson module ν, defined as the ratio between the lateral and axial dilatation.

Brittle materials, such as glass, have however less ductility. They do not have a large plastic component and their fracture is more repentine, as shown in Fig. 3.2R.

All the above considerations are strictly true with tensile loads. The compression diagrams are quite similar, but the ultimate yield strenghts are much higher.

[1]For some materials, such as aluminium, the yield point A is hard to define. It is customary to adopt the offset method, defining A at the 0.2% plastic deformation noted in the experimental tests.

3.1.2 Shear stress and strain

While normal stress acts perpendicular to a given surface A, shear stress is produced when a force acts tangentially wrt the same surface.

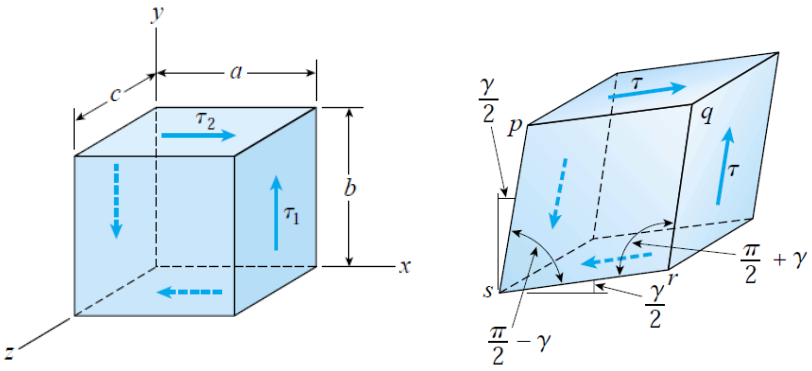

Figure 3.3: Shear stresses convention (left), shear strain (right)

With reference to Fig. 3.3L, two shear stress components τ_1, τ_2 on the equal upper and right-side faces are considered. Assuming that the shear stresses are evenly distributed on the surfaces, the element is in equilibrium when these stresses are equal in magnitude and opposite in direction. Graphycally, this means that the forces always have arrowheads pointing to a common point or leaving simultaneously.
Unlike normal strain, shear strains do not vary the length of the material but its spatial arrangement. The shear deformation is defined as γ; the whole γ is only for the inner side deformation, while the real deformation per side is half of that value.

The eq. (3.3) has a shear counterpart that extends Hooke's law in shear

$$\tau = \mathcal{G}\gamma \tag{3.4}$$

where $\mathcal{G}$ is called shear modulus of elasticity. $\mathcal{G}$ and $\mathcal{E}$, together, define the Poisson coefficient ν

$$\mathcal{G} = \frac{\mathcal{E}}{2(1+\nu)} \tag{3.5}$$

Usually the Poisson ratio is positive, which means that a material reduces its thickness if tractioned, viceversa if compressed[2]. The follow-up consideration is that ν binds $\mathcal{E}$ and $\mathcal{G}$, indicating that the directional elastic properties of the material are not generally independent of each other.

An additional elastic parameter, called bulk modulus, defines how much a material is resistant to compression. For most materials, especially for metals, this can be expressed as a function of both the Poisson ratio and the elastic modulus, as in the following equation

$$\mathcal{K} = \frac{\mathcal{E}}{3(1-2\nu)} \tag{3.6}$$

[2]Some particular materials, called auxetics, have a negative Poisson ratio and they thicken if tractioned.

3.2 Safety factors and allowable stresses

From an engineering point of view aimed at obtaining components that do not rapidly break and do not suffer irreversible deformations, it is necessary to focus on two parameters: to avoid fractures over a certain time span it has to be imposed that the component shall work cyclically with loads below those of fracture; to avoid irreversible deformations means to never have stresses close or beyond the plasticization, or yield, limit.

A safety factor $n > 1$ can limit the maximum stress so that no plastic deformation arises. At the same time, this safety factor defines the maximum allowable stress, once given the maximum one of yielding σ_y. Therefore

$$\sigma_{all} = \frac{\sigma_y}{n} \tag{3.7}$$

the equation above works well for safety considerations regarding ductile materials. For brittle materials it is customary to impose the ultimate stress σ_u as limit, especially due to the not clearly defined plastic zone. The eq. (3.7) for brittle materials is

$$\sigma_{all} = \frac{\sigma_u}{n} \tag{3.8}$$

3.3 Structures optimization

In the present text, the term structure optimization refers to an optimized structure as the lightest among all of those able to withstand the maximum allowable stress defined with a certain safety factor n. It is taken as reference a partially excavated cylinder (a hollow cylinder).

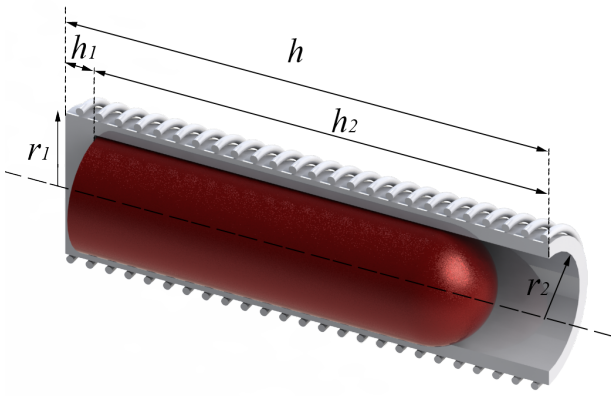

Figure 3.4: Sample design - bucket with payload (tank)

If the cylinder has a total heigth of h, it can be divided into two sections: h_2 refers to the hollow tube, while h_1 to the base filled cylinder. Similarly, r_1 is the radius of the main cylinder and r_2 is the inner hole radius. The existing load force are F_{x1}, applied equally on the anular surface at the top of the hollow tube, and F_{x2}, applied equally on the bottom of the hole.

It is easily inferred that the two areas A_1 and A_2 on which the forces act are

$$\begin{cases} A_1 = \pi \left(r_1^2 - r_2^2 \right) \\ A_2 = \pi r_2^2 \end{cases} \tag{3.9}$$

It follows that the volume of the total structure is

$$\mathcal{V} = \mathcal{V}_1 + \mathcal{V}_2 = A_1 h + A_2 h_1 = \pi r_1^2 h - \pi r_2^2 h + \pi r_2^2 h_1 = \pi \left[r_1^2 h - r_2^2 \left(h - h_1 \right) \right] \tag{3.10}$$

and, therefore, having ϱ_{mat} as material density, its mass is

$$m = \mathcal{V} \varrho_{mat} = \pi \left[r_1^2 h - r_2^2 \left(h - h_1 \right) \right] \varrho_{mat} \tag{3.11}$$

The minimum mass is achieved the more h_1 is close to h and the more r_2 is close to r_1.

Once the material of the structure has been defined, consequently it is defined in which case of the eqs. (3.7, 3.8) the problem falls. Therefore, it is defined the allowable force on the given area, which at minimum should be (and, optimizing, has to be) the applied force.

$$\begin{cases} \sigma_1 = \dfrac{F_{x_1}}{A_1} \leq \sigma_{all_1} = \dfrac{\sigma_y}{n} \\ \sigma_2 = \dfrac{F_{x_2}}{A_2} \leq \sigma_{all_2} = \dfrac{\sigma_y}{n} \end{cases} \tag{3.12}$$

$$\begin{cases} F_{x_1} = \sigma_{all_1} A_1 = \dfrac{\sigma_y}{n} \pi \left(r_1^2 - r_2^2 \right) \\ F_{x_2} = \sigma_{all_2} A_2 = \dfrac{\sigma_y}{n} \pi r_2^2 \end{cases} \tag{3.13}$$

It is added another condition. The heigth h_2 and the radius r_2 are constrained by the dimensions of a cylindrical payload inserted into the cavity. It follows that the force F_{x_2} is given precisely by the weight that the payload exerts on the bottom of the hole and, in first approximation, it can be stated that the payload occupies exactly the available space. Given the mass of the payload m_p and its density ϱ_p, the payload volume is obtained and the following conditions are imposed

$$\begin{cases} \mathcal{V} = \dfrac{m_p}{\varrho_p} = \pi r_p^2 l_p \\ r_p = r_2 \\ l_p = h_2 \end{cases} \tag{3.14}$$

it follows

$$\begin{cases} m_b = \mathcal{V}_b \varrho_b = \pi \left[r_1^2 h - r_p^2 \left(h - l_p \right) \right] \varrho_p \\ F_{x_1} = \dfrac{\sigma_y}{n} \pi \left(r_1^2 - r_p^2 \right) \\ F_{x_2} = \dfrac{\sigma_y}{n} \pi r_p^2 \end{cases} \tag{3.15}$$

The total mass is therefore

$$\begin{aligned} m = m_p + m_b = \mathcal{V}_p \varrho_p + \mathcal{V}_b \varrho_b = \pi r_p^2 l_p \varrho_p + \pi \left[r_1^2 h - r_p^2 \left(h - l_p \right) \right] \varrho_b \\ = \pi r_p^2 l_p \varrho_p + \pi r_1^2 h \varrho_b - \pi r_p^2 h \varrho_b + \pi r_p^2 l_p \varrho_b \end{aligned} \tag{3.16}$$

3.4 Speed of sound in solids

The speed of sound in solids depends on the material intrinsic properties such as those defined in Paragraphs 3.1.1, 3.1.2. In particular the sound propagation follows the earthquakes phenomenon with P-waves and S-waves, respectively the faster longitudinal primary waves and the slower traslational secondary ones, such that

$$\begin{aligned} c_{s,L} &= \sqrt{\frac{\mathcal{E} \left(1 - \nu \right)}{\varrho \left(1 + \nu \right) \left(1 - 2\nu \right)}} = \sqrt{\frac{\mathcal{K} + \frac{4}{3} \mathcal{G}}{\varrho}} \\ c_{s,T} &= \sqrt{\frac{\mathcal{G}}{\varrho}} \end{aligned} \tag{3.17}$$

These velocities would be constant once defined the three variables in the two eq. (3.17). If, however, these variables undergo a change wrt, for example, the temperature, then the speed of sound will also experience a certain temperature-dependent variation.

Often it is commonly defined an average speed of sound in the material. In this regard, in the literature, there are different formulations that may differ in certain conditions. The two most commonly found formulations (Holland 1963; Romanowski et al. 2015), respectively $c_{s,av,1}$ and $c_{s,av,2}$, are reported below

$$\begin{aligned} c_{s,av,1} &= \left[\frac{1}{3} \left(\frac{2}{c_{s,T}} + \frac{1}{c_{s,L}} \right) \right]^{-1} \\ c_{s,av,2} &= \left[\frac{1}{3} \left(\frac{2}{c_{s,T}^3} + \frac{1}{c_{s,L}^3} \right) \right]^{-\frac{1}{3}} \end{aligned} \tag{3.18}$$

These are the values that will be used in subsequent calculations, in place of those presented in eq. (3.17).

3.5 Properties variation with temperature

Analyzing in more detail the nature of the elastic constant, this depends on the interatomic forces. Metal elements, or ones with crystalline structures, have mainly strong primary bonds among atoms, and therefore they have great $\mathcal{E}$ moduli. In contrast, the secondary weak bonds of non-crystalline elements lead to reduced $\mathcal{E}$.

By dwelling on the metallic elements, it is immediately evident that a variation of temperature causes a variation in the thermal agitation velocity of the atoms: this causes a volumic variation, defined through the bulk constant $\mathcal{K}$, but at the same time it causes a variation in the elastic modulus, given that the atoms experience a variation in their mutual distance and, therefore, in the intensity of their mutual bonds.

Although the nature and entity of these phenomena is to be found with a more detailed thermodynamic study including the Debye temperature (refer to Chapter 4, Section 4.1 for further details), it can be qualitatively stated that the $\mathcal{E}$ variation is negiglible for temperatures close to absolute zero, whereas its decay is sub- or superlinear with the increase of higher temperatures (Wigley 2012).

Analyses related to the trasformations of crystalline structures of materials wrt change in temperature are neglected. Moreover, pure elements are considered, which means that referring to aluminium, for example, actually means dealing with the Al element, and not one of its alloy.

From the smallest variation at the atomic level it is possible to obtain large variations in density, elastic moduli, conductivity, and many other characteristics as the temperature changes. Given the vastness of the subject and the almost infinite number of materials, in this dissertation are considered only Cu and Al.

The MPDB (JAHM Software, Inc. 1998) software lends itself as an excellent alternative to numerically evaluating –and complicating the analysis– all these properties at cryogenic temepratures, allowing to draw up tables with discrete values from which it is possible to proceed by numerical extrapolation. The complete tabulation can be found in Appendix A, Table A.6.
As can be seen from the Fig. 3.5, it is evident that the density and the elastic modulus of the two materials confirm the expected trends. There is a more or less marked decrease of both values as the temperature increases, demostrating that the materials dilate and become more malleable. This behaviour is clearly to be taken into consideration, as it can substantially influence an analysis and may lead to incorrect results if neglected or misjudged. In fact, by implementing these values in the equations of the speed of sound eq. (3.17) in a medium, the following results are obtained

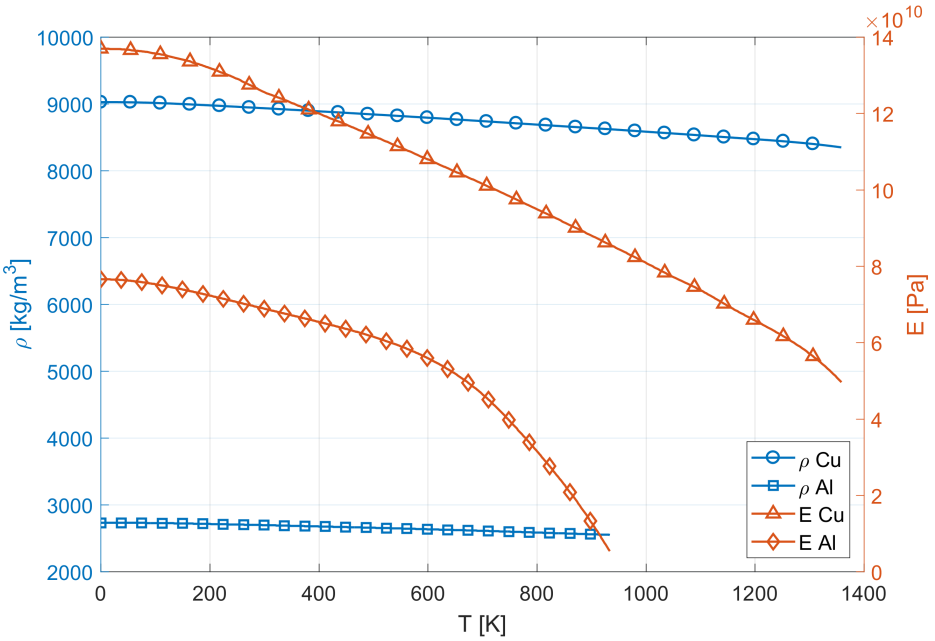

Figure 3.5: Density ϱ and elastic modulus $\mathfrak{E}$ variation wrt temperature T for Cu and Al

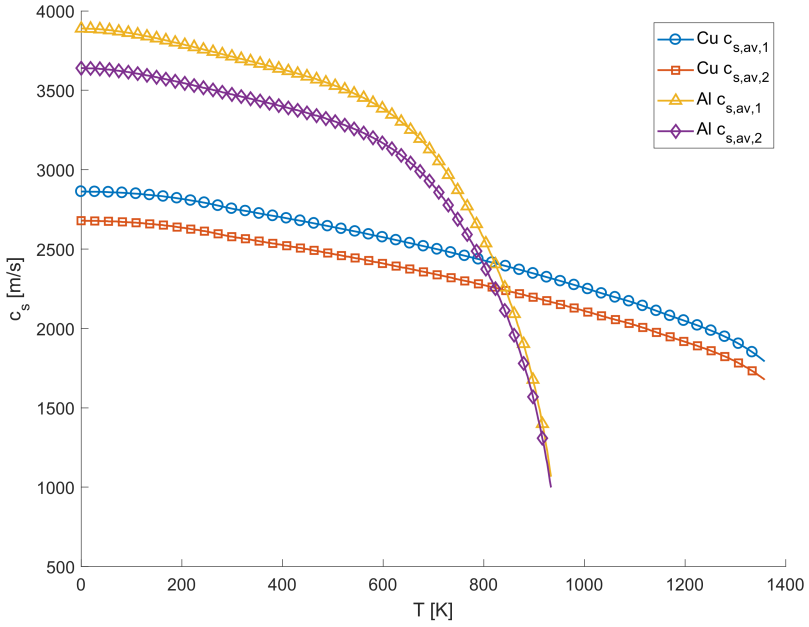

Figure 3.6: Speed of sound in a medium as a function of temperature $c_s = f(T)$

In the following Fig. 3.6 it is possible to notice the trend of the longitudinal, transversal, and averaged speed of sound waves propagation –whose last formulation is shown in the two forms $c_{s,av,1}$ and $c_{s,av,2}$ as in eq. (3.18)–.

For the purposes of this analysis, temperatures below $T = 90\,\mathrm{K}$ will never be treated. Furhtermore, the melting values of the materials would be avoided. With these hypoteses, and considering only copper for reasons that will be subsequently explained, it is possible

to derive an interpolating function for each of the quantities described. Namely

$$\begin{aligned} E(T) \approx\ & 1.367357\ \cdot 10^{11} + 1.506419\ \cdot 10^{7} T - 2.842035\ \cdot 10^{5} T^{2} + \\ & + 4.587768\ \cdot 10^{2} T^{3} - 1.810566\ \cdot 10^{-1} T^{4} - 3.317744\ \cdot 10^{4} T^{5} + \\ & + 3.834610\ \cdot 10^{-7} T^{6} - 1.161974\ \cdot 10^{-10} T^{7} \\ \varrho(T) \approx\ & 9.027303\ \cdot 10^{3} + 1.115309\ \cdot 10^{-1} T - 3.008421\ \cdot 10^{-3} T^{2} + \\ & + 8.852896\ \cdot 10^{-6} T^{3} - 1.513867\ \cdot 10^{-8} T^{4} + 1.459334\ \cdot 10^{-11} T^{5} + \\ & - 7.354734\ \cdot 10^{-15} T^{6} + 1.503195\ \cdot 10^{-18} T^{7} \end{aligned} \tag{3.19}$$

4. Thermodynamics

> *Zeroth: there's a game. First: you can't win. Second: you can't break even. Third: you can't quit.*
>
> — C. P. Snow

An in-depth study of thermodynamics would require a substantial separate treaty and goes beyond the scope of the dissertation. Therefore, here are presented the main principles and some useful considerations for the continuing of the study.

First of all, it is considered a "system", for reference a region of space with a certain mass and delimited by a boundary between the system and the surrounding environment.

The concept of energy $\mathcal{E}$ can have different variations depending on the specific topic. Energy can be defined as the ability to perform an action and it is a quantity that can be trasferred -or converted- mainly into three forms, that are heat, work, and mass flow. Heat is the form of energy that is trasferred due to a temperature difference; work by means of a force along a distance; mass flow by exchanging mass between a system and the outside.

If the mass of a system is kept constant, then the energy can be trasferred only through heat or work. If the system is fixed and closed, which means it has constant mass with fixed boundaries, then the energy can be trasferred only through heat.

Thermodynamics' key concept is the thermal equilibrium. Two systems in contact with different temperatures show a heat transfer from the warmer to the colder region and, after being in contact long enough, their temperatures coincide. This concept extends to n bodies by transitive property, and its intrinsic meaning, though it may seem trivial and naive, is so important to be called zeroth law of thermodynamics (Cengel 2002). In essence, it implies the existance of the temperature as a system property and, qualitatively, as an indicator of how spontaneosly a system is inclined to yield spontaneously part of its own energy.

The following three well-known laws of thermodynamics can have many different facets depending on the scope and the most convenient definition for the specific case. However, despite the definition, the physical meaning remains unchanged, that is that the energy is conserved, natural processes are irreversible and disordered, and that any system at absolute zero temperature has minimal residual entropy.

The period just above attempts to enclose, perhaps in a too hasty and inaccurate way, the many implications contained in the first, second, and third law of thermodynamics.

4.1 Heat capacity

Every system has a certain total energy $\mathcal{E}$. This can be considered, in first approximation, composed by three main components

$$\mathcal{E} = \mathcal{E}_i + \mathcal{E}_k + \mathcal{E}_p \tag{4.1}$$

where $\mathcal{E}_i$ is the internal energy (often referred to as U), $\mathcal{E}_k$ the kinetic, and $\mathcal{E}_p$ the potential. The first law of thermodynamics, also known as the conservation of energy principle, establishes that the total energy that a system possesses can at most, during a process, vary its form and redistribute itself in the different components of eq. (4.1), but never create or destroy itself. In other words, if the energy of a system increases or decreases, in another external space one or more systems have lost or gained energy, respectively.

The internal energy is given by the sum of heat and work, that is

$$\Delta\mathcal{E}_i = \Delta U = \mathcal{Q} + \mathcal{W} \tag{4.2}$$

Conventionally, the two values are positive when entering the system, i.e. for heat absorbed and work done on the system, or negative for outsourcing. If a system is stationary, then kinetic and potential energies in the eq. (4.1) experience no net variation and its total energy variation coincides with its change in internal energy. In this case, heat, that is energy in transition, is the only form of transferable energy (Boles 2014), and the eq. (4.2) reduces to the simpler

$$\Delta U = \mathcal{Q} \tag{4.3}$$

There are three mechanisms of heat transmission, depending on whether this is transmitted through molecular contact, fluids, or Electromagnetic waves (EMVs). Another way to express the eq. (4.3) and to relate the variation of internal energy with the temperature variation is to introduce the concepts of heat capacity C and specific heat capacity c. Therefore,

$$\Delta U = mc\Delta T = C\Delta T \tag{4.4}$$

The specific heat defines the heat needed to change by 1 degree (Celsius or Kelvin) 1 kg of matter. Since a stationary system can not change its shape and, therefore, its volume, in this case the specific heat is at constant volume, c_v [1].

Specifically, the eq. (4.4) is valid only for temperature variations without substance phase change. In the case of incompressible systems, i.e. solids and the great part of liquids, $c_v = c_p$, and the specific heats depend only on temperature.

[1] If, as great part of materials do, a system expands when heated, this would perform a work towards the surrounding environment and, if the pressure remains constant, it can be defined a specific heat at constant pressure such as it is always valid $c_p > c_v$.

The specific heat is strongly temperature dependent, with different trends for different temperature ranges. In the ideal case, its trend is linked to the Degree of freedom (DOF) of the atoms that make up the system, that is, in which ways each atomic or molecular structure can move -translations, rotations, vibrations-, and when these modes "activate" due to the thermal energy. The detailed quantum mechanics treatment is well beyond the scope of the discussion, but it can be easily found in the literature, for example in (Schroeder 1999) or (Ashcroft and Mermin 1976). For the moment, it shall be sufficient to state that there are two mathematical models for the c evaluation: one for ambient or higher temperatures, the law of Dulong and Petit, and one for lower temperatures, the Einstein-Debye model, which takes into consideartions the quantum processes.

The basis of these considerations is the equivalence, at the molecular level, of the kinetic energy of a particle with its thermal energy, such that for each spatial direction $\{x, y, z\}$ the following equality holds

$$\frac{1}{2}mV_x^2 = \frac{1}{2}mV_y^2 = \frac{1}{2}mV_z^2 = \frac{1}{2}k_BT \tag{4.5}$$

The vector sum of the terms in the eq. (4.5) provides the translational kinetic energy $\mathcal{E}_{k,t}$ of a molecule such that

$$\mathcal{E}_{k,t} = \frac{1}{2}mV^2 = \frac{3}{2}k_BT \tag{4.6}$$

A quick observation of eq. (4.6), strictly valid for gases, most liquids, and -sometimes- for solids, points out that the average velocity due to thermal agitation for the molecules is greater for light atoms than for light ones, at the same temperature.

The more general and realistic formulation of eq. (4.6) is called equipartition (of energy) theorem; each form of energy contained in a molecule is referred to as DOF, and this may be due to a translation, rotation, vibration, or elastic potential energy. Each form of energy has a quadratic function such as those in eq. (4.5), and the theorem states that each has an average thermal energy equal to $\frac{1}{2}k_BT$. However, the theorem fails to correctly evaluate molecular energy at low temperatures, i.e. when thermal energy is lower than quantum energy, that is when some DOFs are "frozen out".

Generally, by relating these considerations to eq. (4.4), it can be stated that the average internal thermal molecular energy for N molecules with n_f DOFs activated is equal to

$$U_{th} = Nn_f\frac{1}{2}k_BT \tag{4.7}$$

The real problem in quantum mechanics is to understand which DOFs are active. Translational degrees are usually three. Rotational degrees depend on inertia on rotation; linear molecules, i.e. oxygen O_2, lack a rotational DOF since the inertia around the connection axis is negligible; polyatomic molecules, however, can rotate around three axis. Molecular vibration is more complex, as each vibration has at least two DOFs, one for the vibrational kinetic energy and one for the spring potential, and at room temperature many vibrational DOFs are frozen out, that is, they do not own enough energy to contribute. For example,

atoms in solids can vibrate in the three main directions, and therefore the vibrational DOFs are 6, 3 kinetic and 3 potential.

Another useful formulation called energy capacity, with reference to the (4.4), is

$$C_{\mathcal{V}} = \left(\frac{\partial U}{\partial T}\right)_{\mathcal{V}} \tag{4.8}$$

From now on, unless otherwise specified, reference is made to steady-state stationary systems. Therefore, it is possible to differentiate the (4.7) to obtain

$$C = \frac{\partial U}{\partial T} = \frac{N n_f k_B}{2} \tag{4.9}$$

As written, the eq. (4.9) is known as rule of Dulong and Petit and it assumes that the heat capacity, and consequently the specific heat c, is independent of the temperature and, therefore, it is fixed and constant for a given number of DOFs. This implies, in turn, that the DOFs number is temperature independent, which is known to be not always true.

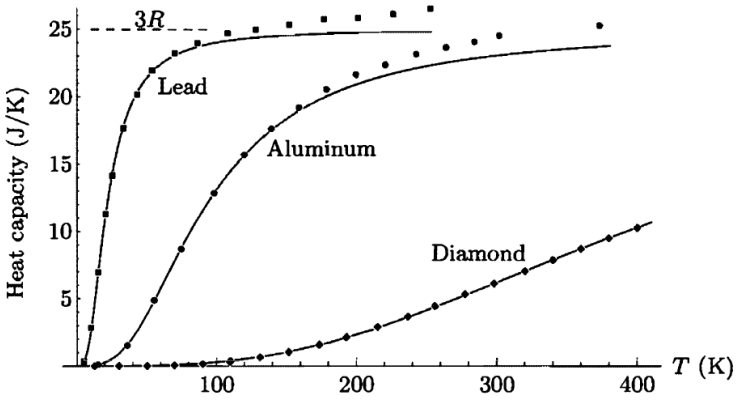

Figure 4.1: $C_{\mathcal{V}} - T$ for solid with varying temperature (Schroeder 1999)

Nevertheless, this rule approximates the values of specific heats at high temperatures, in which, for example, a solid tends to have a $C = 3\mathcal{R}$, as can be noted in Fig. 4.1.

It is easy to note that the law of Dulong and Petit lends itself to analyses in specific high temperature ranges, provided that some approximations are accepted. While this law is based on the statistical Maxwell-Boltzmann energy distribution, Einstein's contribution had to be expected, followed by Debye's one, to allow the inclusion of quantum phenomena and electron lattice vibrations (phonons), respectively. Again, how the Einstein-Bose statistic energy distribution is introduced, what the quantum harmonic oscillators are, how these affect the intensive quantities of materials, and other observations on energy states, are far beyond the scope of the discussion.

The main result researched here is an integral or closed formulation of the heat capacity for each temperature range. This exists and exploits two concepts called Fermi energy ε_F and Debye temperature T_D. For what concerns the first quantity

$$\varepsilon_F = \frac{h^2}{8m_e}\left(\frac{3N}{\pi\mathcal{V}}\right)^{\frac{2}{3}} \tag{4.10}$$

where the value $\frac{N}{\mathcal{V}}$ is the electron density, which is function of the material (see Appendix A, Table A.4). This is the highest energy an electron can have.

The Debye temperature is defined as

$$T_D \stackrel{!}{=} \frac{hc_s}{2k_B}\left(\frac{6N}{\pi\mathcal{V}}\right)^{\frac{1}{3}} \tag{4.11}$$

here c_s is the speed of sound in the material defined in eq. (3.17). Sometimes the eq. (4.11), moving the $\frac{1}{2}$ factor in the parenthesis, is written in the form of the Debye frequency ν_D

$$T_D \stackrel{!}{=} \frac{h\nu_D}{k_B} = \frac{h}{k_B}c_s\left(\frac{3N}{4\pi\mathcal{V}}\right)^{\frac{1}{3}} \tag{4.12}$$

For gases and for metal lattice vibration there is a formulation in closed form of the internal energy as a linear function of temperature. This, once derived over temperature, provides the heat capacity per mole as (Schroeder 1999)

$$C_{lv} = \frac{\pi^2 N_A k_B^2 T}{2\varepsilon_F} \tag{4.13}$$

For solids, it could be possible to refer to Einstein solid model, in which each atom vibrates independently in three directions. This model, however, may be inaccurate especially for metals, in which the lattice vibration has a key role; indeed, the Einstein model shows an exponential decay of C versus temperature, while experimentally it is known that $C \propto T^3$. Hence the need to include Debye's contribution to the Einstein model, which is an excellent approximation for low and high temperatures. It can be proved that it is possible to express the internal energy as (Van Sciver 2012)

$$U = 9Nk_B\frac{T^4}{T_D^3}\int_0^{\mathcal{T}}\frac{x^3}{e^x-1}\,\mathrm{d}x \tag{4.14}$$

where $\mathcal{T} = \frac{T_D}{T}$. The upper and lower limit solutions of the eq. (4.14) are

$$\begin{cases} U = 3N_A k_B T & C = 3N_A k_B & T \gg T_D \\ U = \dfrac{3}{5}\pi^4 N_A k_B \dfrac{T^4}{T_D^3} & C = \dfrac{12}{5}\pi^4 N_A k_B\left(\dfrac{T}{T_D}\right)^3 & T \ll T_D \end{cases} \tag{4.15}$$

results which agree with the Dulong and Petit approximation eqs. (4.7, 4.9) for a solid in which $n_f = 6$, and therefore with the equipartition theorem eq. (4.5) and the Einstein solid

model. An additional consideration must be made wrt metals; in these the heat capacity is increased due to the conduction electrons, and in the free electron model this additional linear term for the lattice vibration is the one presented in the eq. (4.13).

The set of all the considerations just made shows how the thermodynamic problem, even as presented in a quick and simplistic manner, is complex and strongly diversified according to the temperature ranges. A good approximation for the heat capacity, for temperatures above $10 \div 20\,\mathrm{K}$, may be that of deriving eq. (4.14) and of numerically evaluating the integral. For the level of the present discussion and for the phase of the project, this method seems the most appropriate, sufficiently precise and unequivocal as the temperature changes. Therefore

$$C = 9N_A k_B \left(\frac{T}{T_D}\right)^3 \int_0^{\mathcal{T}} \frac{x^4 e^x}{\left(e^x - 1\right)^2}\,\mathrm{d}x \qquad [\mathrm{J\,mol^{-1}\,K^{-1}}] \tag{4.16}$$

It is inferred that eq. (4.16) provides the heat capacity per mole of matter (to be precise, this would be a specific molar heat). By dividing it by the molecular mass of the material, it is possible to obtain the specific heat in the International System of Units (SI). Therefore

$$c = \frac{9N_A k_B}{\mathcal{M}} \left(\frac{T}{T_D}\right)^3 \int_0^{\mathcal{T}} \frac{x^4 e^x}{\left(e^x - 1\right)^2}\,\mathrm{d}x \qquad [\mathrm{J\,kg^{-1}\,K^{-1}}] \tag{4.17}$$

4.1.1 Temperature dependence of Debye temperature

The particularity of defining the Debye temperature as the limit between the temperature regions in which quantum phenomena should be considered or not, and subsequently declare that this temperature is dependent on the temperature itself, should sound an alarm bell. Not by chance, in literature, can be found dozens of studies in which the same material shows a different Debye temperature (Patterson and Bailey 2016; Pässler 2017). To date, defining a "Debye temperature" has become more a consolidate terminology, since nowadays its trend is obtained from the experimental values of heat capacities, which are temperature dependent. The heat capacities trend $C = f\left(T_D(T)\right)$ is called "non-Debye nonmonotonic model" and requires highly elaborate analytical models for each material.

In the present analysis, it would burdensome and counterproductive to carry out this study, since the whole Chapter has been focusing on the specific heats calculations as output parameter. Although the calculation of T_D from eq. (4.11) is sufficiently accurate wrt the values found in literature, it is common nowadays to choose and force T_D as that temperature-varying value which allows to obtain specific heats values comparable to those found experimentally (Schroeder 1999; Van Sciver 2012; Patterson and Bailey 2016).

Therefore, this particular analysis is avoided. To give a better realism, though, the effect of temperature in the speed of sound in solids is included, in the form of variation of Young's modulus in eq. (3.17) as done in Section 3.5, Fig. 3.6. By doing so, the T_D defined in eq. (4.11) is temperature dependent, as shown in the following Figure

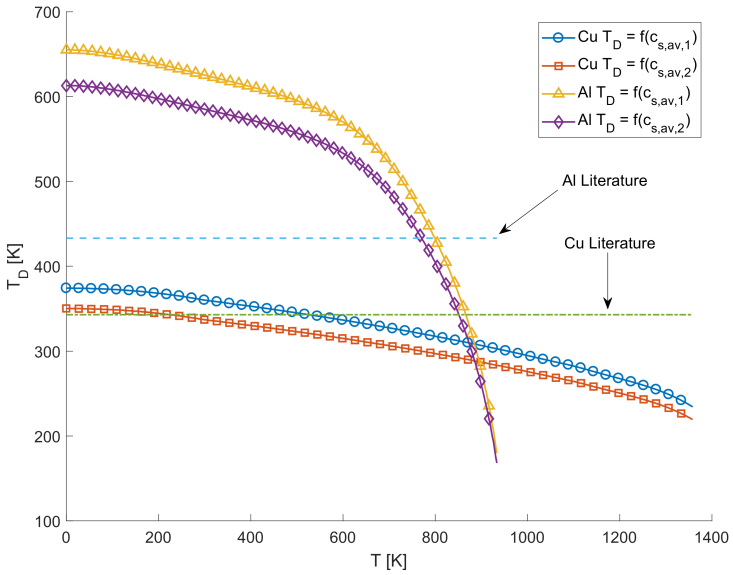

Figure 4.2: Debye temperature as a function of temperature $T_D = f(T)$

The T_D usually found in literature differs from the calculable values and intersects the other curves only in some points, i.e. for the copper around the room temperature. Nevertheless, the values calculated with the formulas eqs. (3.17, 3.18, 4.17) should provide a more truthful trend of the T_D and, consequently, of the specific heats c values, even compared with those read from the MPDB software

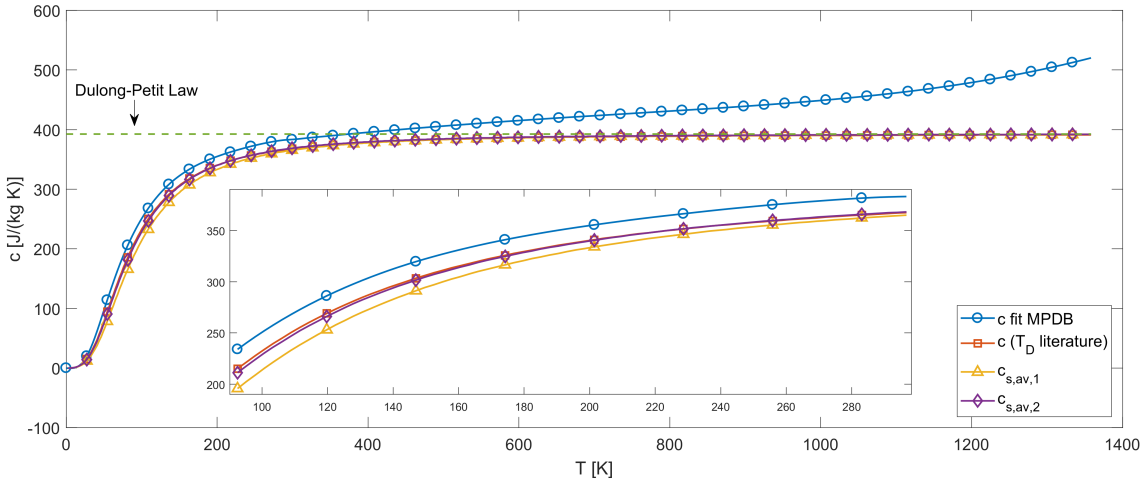

Figure 4.3: Specific heat of Cu as a function of temperature $c|_{Cu} = f(T)$

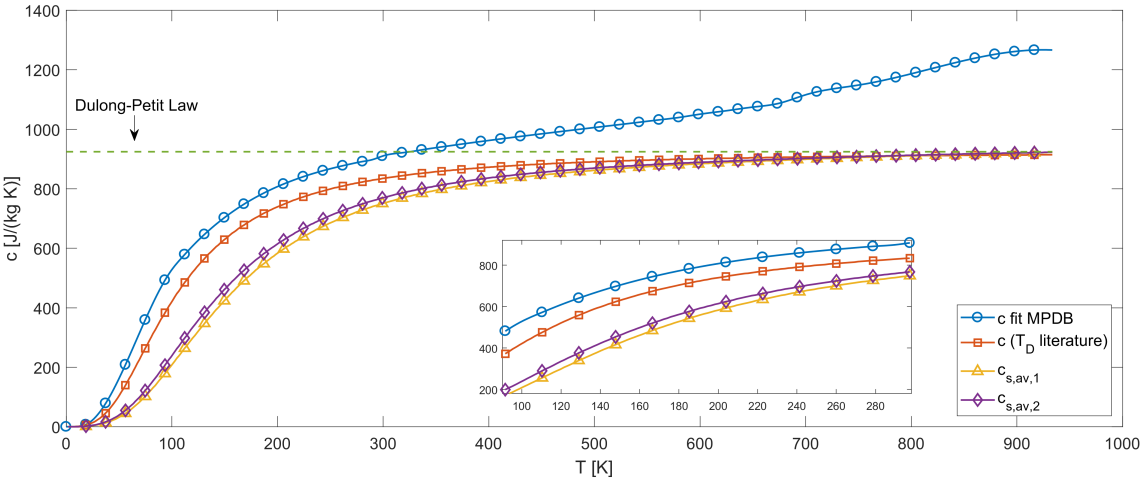

Figure 4.4: Specific heat of Al as a function of temperature $c|_{Al} = f(T)$

In the two Figs. 4.3, 4.4, the asymptotic trend of the curves is clearly shown, in accordance with the Dulong and Petit approximation in eq. (4.9). In both cases, at least one curve approaches sufficiently the experimental values. Unfortunately, this curve is always the one given by the T_D chosen in literature to match the specific heat experimentally measured values. For this reason, and due to the fact that the analytical formulations fail to take into account the specific heat increase beyond the Dulong-Petit limit, the interpolated values from the MPDB software will be used in the continuation of the analysis.

4.2 Thermal conduction

Conduction is one of the three heat transfer mechanisms and occurs through a physical exchange of thermal energy between particles in contact with each other; the other two are convection and radiation. In a solid the conduction can take place between any two points inside the material itself or at the boundary of two materials. The transported heat $\mathcal{Q}$ is dimensionally related with the heat transfer rate $\dot{\mathcal{Q}}$ and the heat flux $\dot{q}$ as follows

$$\mathcal{Q} = \dot{\mathcal{Q}}\Delta t = \dot{q}A\Delta t \tag{4.18}$$

The heat equation is a general Partial Differential Equation (PDE) that describes the three-dimensional (3D) heat transport in a stationary, homogeneous, and isotropic solid (Hahn and Özişik 2012) both in space and time

$$\nabla \cdot (k\nabla T) + g = \varrho c\frac{\partial T}{\partial t} \tag{4.19}$$

where the nabla operator varies depending on the coordinate system. For example, by directly showing the heat equation in cylindrical coordinates, and developing the vector differential operator, the general heat conduction in eq. (4.19) is

$$\frac{1}{r}\frac{\partial}{\partial r}\left(kr\frac{\partial T}{\partial r}\right) + \frac{1}{r^2}\frac{\partial}{\partial \varphi}\left(k\frac{\partial T}{\partial \varphi}\right) + \frac{\partial}{\partial z}\left(\frac{\partial T}{\partial z}\right) + g = \varrho c\frac{\partial T}{\partial t} \tag{4.20}$$

The eq. (4.20) states that the net rate of heat conducted per volume unit plus the rate of energy generated per volume unit, in the left-hand side (lhs), is equal to the net energy stored per volume unit, in rhs. Furthermore, $\{r, \varphi, z\}$ form the cylindrical coordinate system, respectively in the radial, circumferential, and axial coordinate. The eq. (4.20) with no heat generation leads to the Fourier's equation; steady-state conduction to the Poisson's equation; if both conditions are verified simultaneously, the Laplace equation is found (Karwa 2017).

Assuming a one-dimensional (1D) problem with isothermal conditions in the φ and z coordinate and no heat generation, the remaining non-zero temperature gradient is the radial one and the eq. (4.20) is reduced to the simpler form

$$\frac{1}{r}\frac{\partial}{\partial r}\left(kr\frac{\partial T}{\partial r}\right) = \varrho c\frac{\partial T}{\partial t} \tag{4.21}$$

or, if k is not radius-dependent,

$$k\frac{\partial^2 T}{\partial r^2} + \frac{k}{r}\frac{\partial T}{\partial r} + g = \varrho c\frac{\partial T}{\partial t} \tag{4.22}$$

or

$$\frac{\partial^2 T}{\partial r^2} + \frac{1}{r}\frac{\partial T}{\partial r} + \frac{g}{k} = \frac{1}{\alpha}\frac{\partial T}{\partial t} \tag{4.23}$$

Still simplifying the problem, for a steady-state problem, from the eq. (4.21) it is obtained the Fourier's 1D heat conduction equation (Cengel 2002)

$$\dot{\mathcal{Q}}_{cond} = -kA\frac{dT}{dx} \tag{4.24}$$

the minus sign indicates that heat is conducted in the direction of decreasing temperature. As expected, following the analysis in Sections 3.5, 4.1, the thermal conductivity k is material and temperature dependent itself.

4.2.1 Temperature dependent thermal conductivity

The thermal conductivity for metals is given by the contributions of the electrons and the lattice. As in Section 4.1, k undergoes the same rules and is proportional to the heat capacity (Van Sciver 2012). For model congruity, k values have been interpolated from the software MPDB, as shown in the following Figure

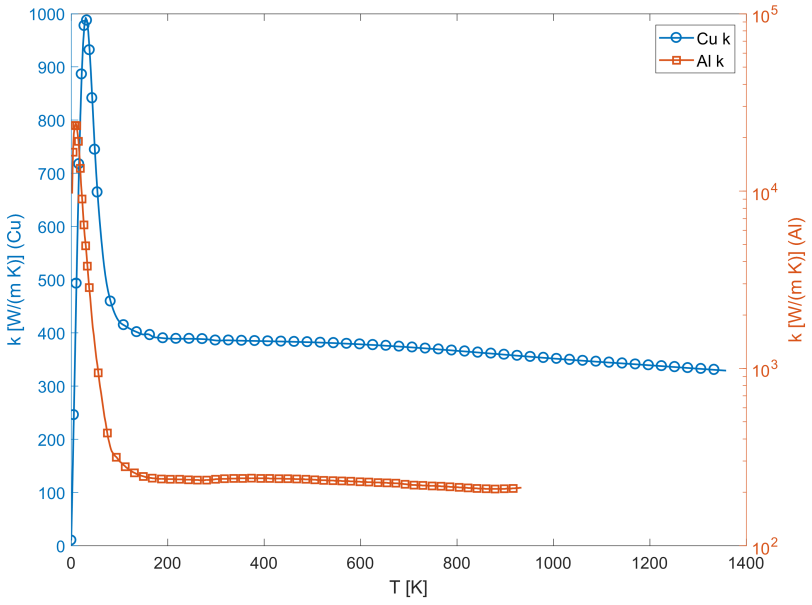

Figure 4.5: Thermal conductivity k variation wrt temperature T for Cu and Al

4.3 Thermal convection

Convection is the principle of heat transfer between a solid and a moving fluid, where the "in motion" concept is crucial, as a stationary fluid transfers heat by pure conduction. This subtle difference between pure conduction and "conduction with fluid motion" (Cengel 2002) is the reason why sometimes, in literature, convection is not considered a transportation phenomenon in its own right but a particular conduction condition. Nevertheless, the rate of conduction heat transfer is described by the Newton's law of cooling

$$\dot{\mathcal{Q}}_{conv} = hA\left(T - T_{\infty}\right) \tag{4.25}$$

where the convection rate transfer coefficient h is not a property of the fluid and is determined sperimentally. For the present analysis, since the case study happens to be on the lunar surface, in the vacuum, and there will never be fluids in motion with which to exchance heat, this transfer mechanism is neglected.

4.4 Thermal radiation

Every body with non-zero absolute temperature emits thermal energy in the form of EMVs, and radiation is the only form of heat transfer that does not require a medium. Although the phenomenon is volumetric –every portion of a body emits energy with different intensity–, in the present analysis only the energy emitted by the external surface will be considered. The radiative heat transfer rate is given by the Stefan-Boltzmann formulation

$$\dot{\mathcal{Q}}_{rad} = \varepsilon \varsigma A\left(T^4 - T_{surr}^4\right) \tag{4.26}$$

It has to be specified that the temperatures in the eq. (4.26) must be expressed in degrees Kelvin. The T_{surr} indicates the temperature of the outside portion of space enclosing the emitting reference surface A. If the surrounding environment is the vacuum, which has a background temperature $T_{BG} \approx 3\,\mathrm{K}$, usually the back-radiation is negligible and the $T_{surr} \approx 0$ can be neglected.

Emissivity ε is a property of bodies that identifies how much these are prone to emit thermal energy in the form of EMVs –where 1 is a black body and 0 a white body–. Emissivity is also strongly temperature dependant for gray bodies, and also wavelength dependent for non-gray bodies.

The complete formulation of the heat equation in cylindrical coordinates containing the emissive phenomena, from the PDE in eq. (4.20), assumes the form (Karwa 2017)

$$\frac{1}{r}\frac{\partial}{\partial r}\left(kr\frac{\partial T}{\partial r}\right) + \frac{1}{r^2}\frac{\partial}{\partial \varphi}\left(k\frac{\partial T}{\partial \varphi}\right) + \frac{\partial}{\partial z}\left(\frac{\partial T}{\partial z}\right) + g = \varrho c\frac{\partial T}{\partial t} - \varepsilon \varsigma \frac{A}{\mathcal{V}}\left(T^4 - T_{surr}^4\right) \tag{4.27}$$

4.4.1 Temperature dependent emissivity

In the present analysis is omitted the study of the reasons for which the optical and thermal properties of a material, such as the emissivity, are dependent on electrodynamic properties, such as the resistivity and the wavelength. It can be stated that the emissivity trend wrt temperature is substantially different for cryogenic and high temperatures.

For low temperatures a closed formulation has been developed over the years, only resistivity- and temperature-dependent (Estalote and Ramanathan 1977; Sievers 1978)

$$\varepsilon = 0.751\,(\varrho T)^{\frac{1}{2}} - 0.632\,(\varrho T) + 0.67\,(\varrho T)^{\frac{3}{2}} - 0.607\,(\varrho T)^{2} + \dots \tag{4.28}$$

For high temperatures the values are taken from the literature (Ramanathan and Yen 1977), even if it exists a complex integral calculation. Both values consider pure materials.

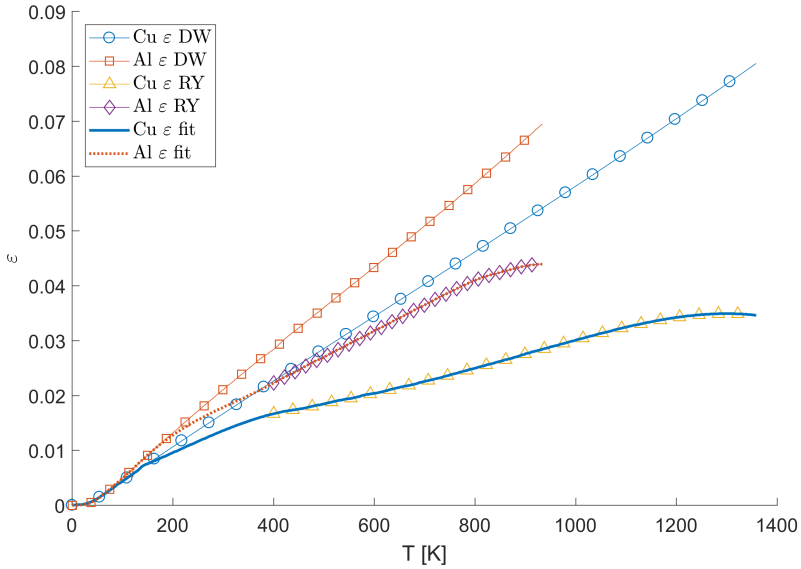

Figure 4.6: Emissivity ε variation wrt temperature T for Cu and Al

The first two curves in Fig. 4.6, following the Davisson-Weeks (DW) formulation in eq. (4.28), were obtained using the interpolated resistivity values from Table A.6, Appendix A. Between the low (DW) and high (Ramanathan-Yen, RW) temperature values, the curves are interpolated.

It is important to underline that the materials used are perfectly pure and no surface treatments have been carried out. For non-pure materials there are higher RRR as the impurity degree increases, with a greater asymptotic value for the resistivity as $T \to 0$ (Van Sciver 2012). At the same time, surface treatments may greatly change the material emissivity. A slight polishing process is supposed in the analysis prosecution, giving a $\approx 50\%$ increase in emissivity.

4.5 Electrothermal analysis

A general overview of the eletrical and thermal phenomena, shown respectively in Chapter 2 and at the beginning of Chapter 4, allows to make an interesting case study which will help to introduce the MD model analyzed in the last part of the present analysis. Although the specific MD configuration will be presented in Chapter 7 and specific case studies will be carried out in Chapter 8, some concepts should be anticipated. It is understood that the reasons for which the following considerations are taken into account have to be found in the aforementioned Chapters, while for the moment the focus will be the understanding of the electrical and thermal phenomena. In particular, it is sought the set of assumptions and simplifications that can be made for the prosecution of the analysis.

The first concept presented has as subject a good conductor. It can be reasonably assumed that copper and aluminium are the two most widespread, as they have excellent conductivity compared to their cost. It is known that the current passage in a conductor dissipates by JE part of the energy, and wrt eq. (4.20), it can be seen as a source of energy in the conductor core. A similar consideration can be made from the first law of thermodynamics in eqs. (4.4, 4.3), so that

$$m_w c_w \dot{T}_w = \dot{\mathcal{Q}}_{Je,w} = R_w I(t)^2 \tag{4.29}$$

where m_w, c_w, and $\dot{T}_w$, in the lhs, are respectively the wire mass, specific heat, and temperature variation over time. In the rhs there is the wire resistance R_w and a certain current source variable in time. By explicitly writing the quantities in the eq. (4.29), with mass as density and volume, it is obtained

$$\varrho_w(T)\ell_w A_w c\dot{T} = \frac{\rho_w(T)\ell_w}{A_w} I(t)^2 \tag{4.30}$$

or

$$\frac{dT}{dt} = \frac{\rho_w(T)}{\varrho_w(T) A_w^2 c(T)} I(t)^2 \tag{4.31}$$

where all temperature-dependent values can be appreciated; to lighten the notation, from now on the temperature-dependent quantities, if already presented in the previous Sections, will be implicitly understood as such without the need of writing (T). The eq. (4.31) is an ODE that can be easily solved numerically. Results could be provided as parametrized, but for sake of readibility the wires cross sectional area A_w is given by a wire radius of $r_w = 0.01\,\mathrm{m}$, while the current is

$$I(t) = 1 \cdot 10^5 e^{-0.8t}\,\mathrm{A} \tag{4.32}$$

By appropriately changing the material-dependent parameters between copper and aluminium, the following results are obtained with the same current trend

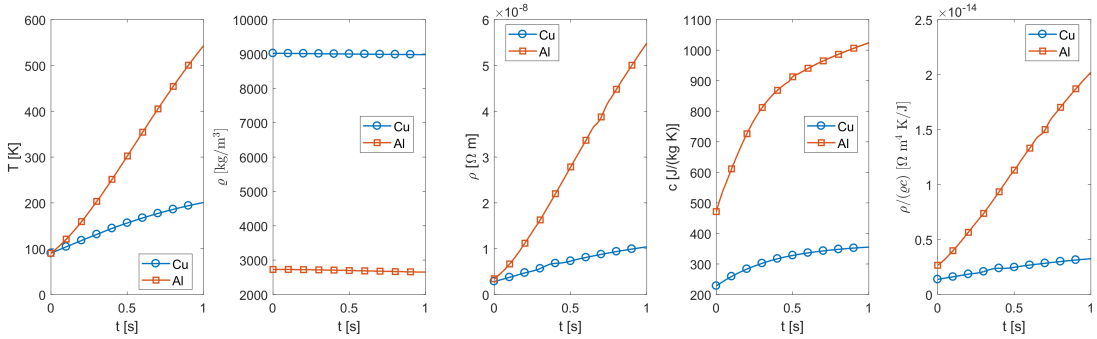

Figure 4.7: $T(t)$ due to JE for Cu and Al

The analysis is performed over one second. If the aim is to better withstand the temperature increase over time, the copper lends itself as the best candidate. The set of its parameters leads to a less intense temperature gradient, as can be noted in Fig. 4.7. To confirm this assumpion, the radiative contribution is added to eq. (4.29)

$$m_w c_w \dot{T}_w = R_w I^2 - \dot{\mathcal{Q}}_{rad,w} \tag{4.33}$$

The additional radiative term in eq. (4.33) is written as

$$\frac{dT}{dt} = -\frac{\varepsilon(T)\varsigma}{\varrho_w(T)\ell_w A_w c(T)} A\left(T^4 - T_s^4\right) \tag{4.34}$$

where A is the cable exposed external surface, ie $A = 2\pi r_w \ell_w$. Performing the same analysis, with a surrounding temperature $T_s = 90.15\,\mathrm{K}$, the following results are shown.

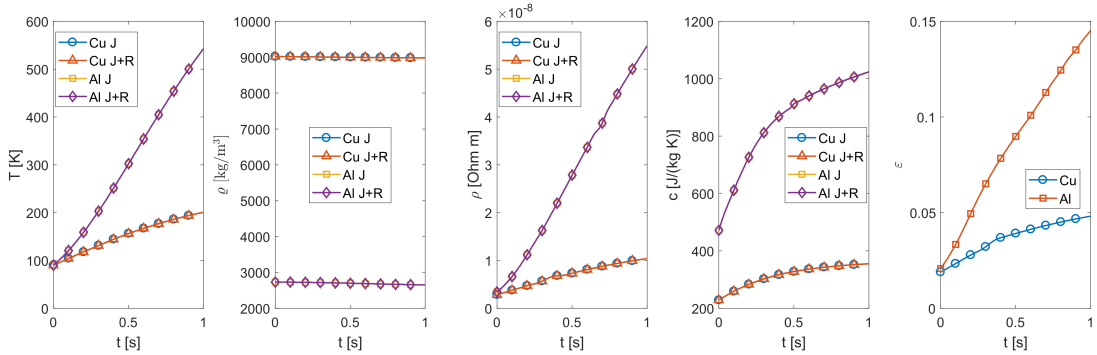

Figure 4.8: $T(t)$, $t \in [0,1]\,\mathrm{s}$ due to JE and radiation for Cu and Al

In Fig. 4.8 the trend of emissivity for both materials takes the place of the last graph in Fig. 4.7, presented only as an indication of the "weigth" of the materials' parameters.

The radiative phenomenon does not significantly vary the maximum temperature reached. Since aluminium reaches a maximum temperature of $T_{Al,max} \approx 550\,\mathrm{K}$, one would anyway expect a slight variation in this particular analysis. To consider this situation, the same is perfomed over 60 seconds: it should be noted that the current in eq. (4.32) was chosen specifically to tend to zero shortly before 2 s, so that the maximum temperature of the wires is mantained subsequently constant without other heat transmission mechanisms.

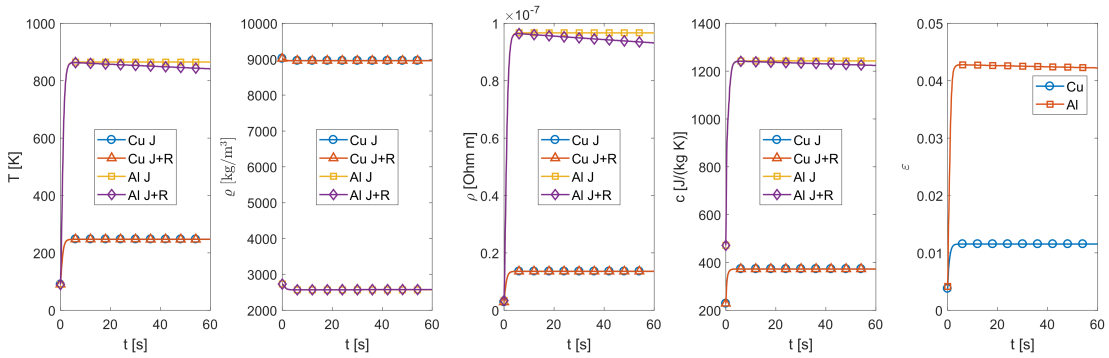

Figure 4.9: $T(t),\ t \in [0,60]\,\mathrm{s}$ due to JE and radiation for Cu and Al

A greater dissipation time and a higher maximum temperature reached allow to dissipate more energy for radiation, as is evident in the case of aluminium in Fig. 4.9, while copper has temperatures still too low for appreciable emissions. It is anticipated that the heating times in the mass driver analysis are in the order of a second, and therefore the last example is for demonstration purposes only.

Although conductive phenomena are still not considered, copper shows a better overall heating resistance. To verify whether or not the radiation is negligible up to one-second copper heating, the analysis is repeated with a higher current

$$I(t) = 1.2 \cdot 10^5\,\mathrm{A} \qquad t \in [0,1] \qquad \Longrightarrow\ T_{Cu,max} \approx 1000\,\mathrm{K},\ t = 1\,\mathrm{s} \tag{4.35}$$

The maximum temperature is certainly indicative of radiative phenomena. It follows

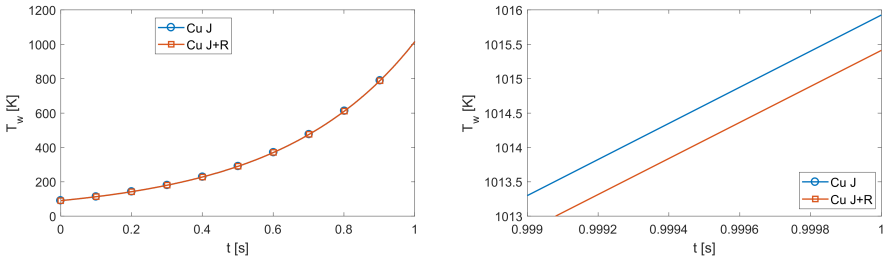

Figure 4.10: High temperature copper radiative emission for $t \in [0,1]$

The radiation reduces by $\approx 1\,\mathrm{K}$ the maximum temperature reached, and therefore the radiative phenomena, even with very high temperatures, are negligible for short times.

4.5.1 Wires insulation

Before considering the conductive heat transportation, it should be noted that is unrealistic to consider that the conductor is left exposed and not isolated. For example, a solenoid-shaped conductor, if not isolated and in contact, would make the current find less resistance in flowing axially instead then circumferentially. Moreover, by isolating the conductor, as radiative emission has been shown negligible, also the conduction will be limited.

The problem, therefore, shifts in finding the insulation (cable or wire) thickness able to withstand the temperatures that the conductor can reach (cable core, or simply core). Many companies provide the standard thickness for heavy-duty cables that can withstand these conditions, for example (Plastelec SAS 2018; Eland Cables 2018). However, it is advisable to find an approximate closed-form formulation for the insulation radius as a function of the core radius.

The heat transfer between core and cable is considered steady. The differential Fourier's law, eq. (4.24), in cylindrical coordinates, integrating between the core and insulator radiuses, r_w and r_{ins}, and over their steady temperatures, T_w and $T_{ext,all}$, is

$$\dot{\mathcal{Q}}_{all,loss} = -2\pi\ell_{ins}k_{ins}\frac{T_{ext,all} - T_w}{\ln\left(\frac{r_{ins}}{r_w}\right)} \tag{4.36}$$

where $T_{ext,all}$ is the allowable temperature at the insulator external surface, and $\dot{\mathcal{Q}}_{all,loss}$ the maximum allowable heat loss of the core. Hence, by solving for r_{ins},

$$r_{ins} = r_w \exp\left[-\frac{2\pi k_{ins}\ell_{ins}}{\dot{\mathcal{Q}}_{all,loss}}\left(T_{ext,all} - T_w\right)\right] \tag{4.37}$$

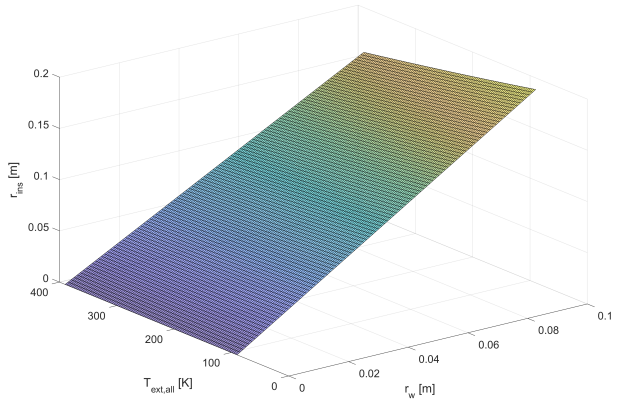

Figure 4.11: Insulation radius r_{ins}

A good insulator can have conducibilities around $k_{ins} \approx 0.02$. The results in Fig. 4.11 assume a power loss per unit length of $\dot{\mathcal{Q}}_{all,loss}/\ell_{ins} = 100\,\mathrm{W\,m^{-1}}$ and a constant core temperature of $T_w = 1100\,\mathrm{K}$, both conservative values wrt real conditions. Given the approximate calculation in eq. (4.37), it may be initially assumed that the isolation radius is $r_{ins} = 1.5r_w$ compared to the core. Nevertheless, some advanced insulation technologies

–by means of polymer dielectric films (Jones and Wright 1992; Tan et al. 2014)– allow very low insulation radii even at high temperatures.

For this reason, the multiplicative coefficient between r_{ins} and r_w is conservatively imposed equal to $k_i = 1.1$.

By inserting these consideration into the PDE in eq. (4.20) and solving numerically with the finite –central– differences method (Recktenwald 2017), the temperature in space and time is

$$T_i^{n+1} = T_i^n + \Delta t \alpha \frac{T_{i+1}^n - 2T_i^n + T_{i-1}^n}{\Delta x^2} \tag{4.38}$$

where $i = 0 : N + 1$ is the discretization of the spatial coordinate, and $n = t_i : dt : t_f$ is the time discretization. The Euler explicit method implies that the Δx can not be chosen at will, since the Courant-Friedrichs-Lewy condition must be respected

$$\text{CFL} = \frac{\alpha \Delta t}{\Delta x^2} < \frac{1}{2} \tag{4.39}$$

By appropriately selecting the discretization steps and the Boundary Conditions (BCs), in which the boundary temperature is the one obtained in Fig. 4.10, the following conductive heat transfer in the insulator is obtained

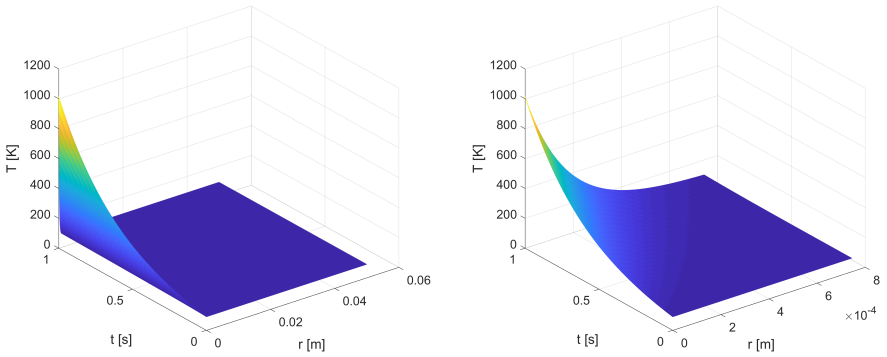

Figure 4.12: Heat conduction calculation with central finite-differences method

Both for the good insulator characteristics and for the short analysis time, the heat does not penetrate deeply and is well confined in the core. To fully validate this approximate analysis, the various parameters obtained in this Section are included in a complete unsteady-transient heat analysis with the Matlab® PDE toolbox.

4.5.2 Application example

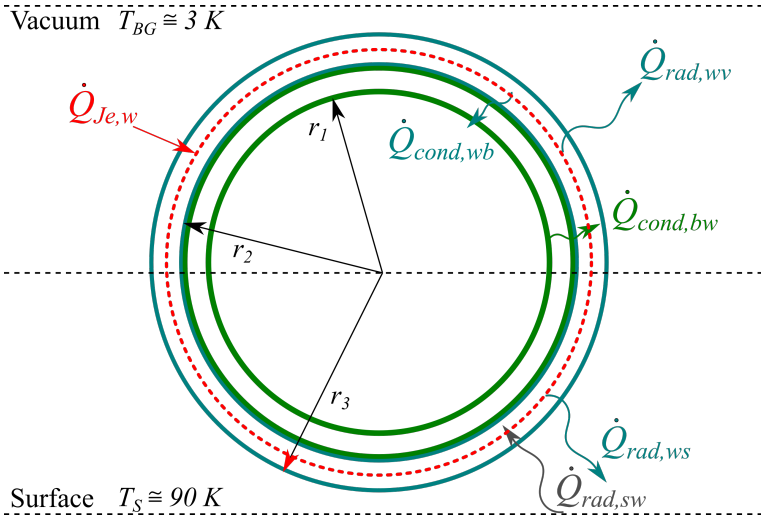

Figure 4.13: Thermal equilibrium of two coaxial cylinders

The Fig. 4.13 represents the resulting case study from the previous Paragraphs considerations. A hollow cylindrical bucket, with inner and outer radius r_1 and r_2, is placed in perfect contact with a coaxial solenoid-shaped insulated wire. The wires packing factor allows it to be considered as a cylinder with inner and outer radius, wrt the central axis, r_2 and r_3. Accordingly scaled, the core is placed with a central mean radius between the insulator ones. The wires are heated by JE and have a $T_w = 1100\,\mathrm{K}$, while the remaining geometries have an initial condition of $T = 90.15\,\mathrm{K}$. The heat is transferred by conduction between all the geometries in contact and by radiation towards the environment. The geometric implementation in the Matlab® PDE toolbox is shown in the following Figure.

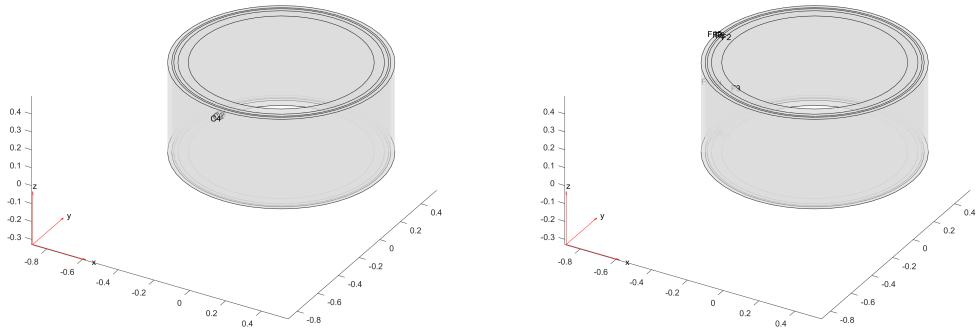

Figure 4.14: Transient heat transport - PDE model

Running the analysis for 1 s produces the following results

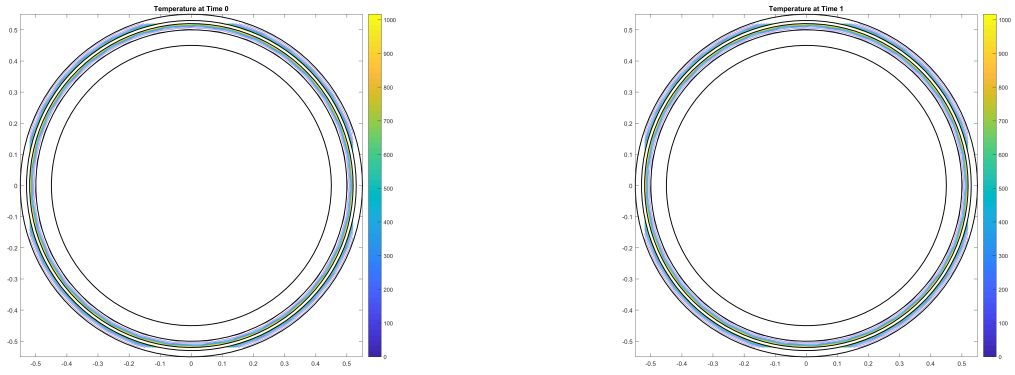

Figure 4.15: Transient heat transport - isothermal contours PDE result for $t \in [0, 1]$

while, running the same analysis, with the same initial and boundary conditions, for 60 s produces the following

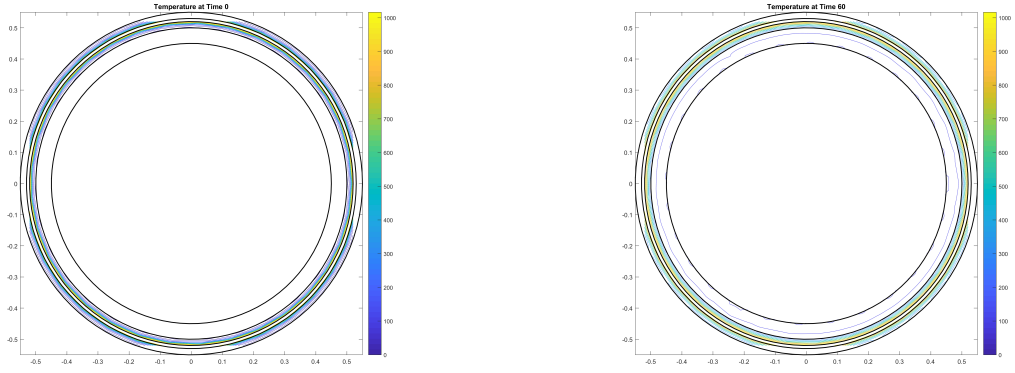

Figure 4.16: Transient heat transport - isothermal contours PDE result for $t \in [0, 60]$

The insulation performs its tasks well. There is no excessive conduction for high temperatures and for long period, as can be clearly seen in Fig. 4.16, and therefore will be minimal and negligible conduction for very short periods, such as those expected in this analysis and shown in Fig. 4.15.

In conclusion, although the radiative and conductive thermal phenomena are fundamental for a complete thermal analysis, it is considered that they can be neglected in the specific case. Nevertheless, future studies could perform a more in-depth analysis of these, which would include, for example, the cooling and reuse times of the components, as well as the life cycle stress limit of the same.

4.6 Polynomial interpolation of thermal properties

The analysis in the current Chapter faithfully reproduces both the experimental value and those made available through MPDB, but suffers for a high computational cost in the implementation due to the high volume of interpolation function calls.

The analysis is adapted trying to preserve its accuracy. It will be shown that the temperature would be kept in $T \in [90, 1200]\,\mathrm{K}$. The range of allowable temperatures outlines a family of properties that can be interpolated polynomially, with at the most 0.7% different values wrt experimental ones, but highly reducing the computational cost.

By writing the generic material property $\mathcal{X} = \{\mathcal{E}, \varrho, c, k, \rho\}$ as

$$\mathcal{X}(T) \approx \sum_{k=0}^{n} a_k T^k \tag{4.40}$$

the following polynomial coefficient for each property are found.

a_k	E	ϱ	c	k	ρ
a_0	$1.367\,357 \cdot 10^{11}$	$9.027\,303 \cdot 10^{3}$	$4.038\,080$	$7.015\,013 \cdot 10^{2}$	$-2.877\,876 \cdot 10^{-10}$
a_1	$1.506\,419 \cdot 10^{7}$	$1.115\,309 \cdot 10^{-1}$	$-2.648\,113$	$-5.818\,977$	$2.495\,959 \cdot 10^{-12}$
a_2	$-2.842\,035 \cdot 10^{5}$	$-3.008\,421 \cdot 10^{-3}$	$1.750\,206 \cdot 10^{-1}$	$4.601\,388 \cdot 10^{-2}$	$5.011\,418 \cdot 10^{-13}$
a_3	$4.587\,768 \cdot 10^{2}$	$8.852\,896 \cdot 10^{-6}$	$-2.381\,144 \cdot 10^{-3}$	$-2.015\,002 \cdot 10^{-4}$	$-1.811\,758 \cdot 10^{-15}$
a_4	$-1.810\,566 \cdot 10^{-1}$	$-1.513\,867 \cdot 10^{-8}$	$1.751\,250 \cdot 10^{-5}$	$5.364\,811 \cdot 10^{-7}$	$3.464\,188 \cdot 10^{-18}$
a_5	$-3.317\,744 \cdot 10^{4}$	$1.459\,334 \cdot 10^{-11}$	$-8.226\,901 \cdot 10^{-8}$	$-9.024\,209 \cdot 10^{-10}$	$-3.590\,511 \cdot 10^{-21}$
a_6	$3.834\,610 \cdot 10^{-7}$	$-7.354\,734 \cdot 10^{-15}$	$2.643\,471 \cdot 10^{-10}$	$9.623\,143 \cdot 10^{-13}$	$1.912\,434 \cdot 10^{-24}$
a_7	$-1.161\,974 \cdot 10^{-10}$	$1.503\,195 \cdot 10^{-18}$	$-6.014\,245 \cdot 10^{-13}$	$-6.301\,254 \cdot 10^{-16}$	$-4.093\,559 \cdot 10^{-28}$
a_8			$9.852\,038 \cdot 10^{-16}$	$2.309\,740 \cdot 10^{-19}$	
a_9			$-1.166\,286 \cdot 10^{-18}$	$-3.626\,692 \cdot 10^{-23}$	
a_{10}			$9.886\,735 \cdot 10^{-22}$		
a_{11}			$-5.850\,912 \cdot 10^{-25}$		
a_{12}			$2.295\,138 \cdot 10^{-28}$		
a_{13}			$-5.361\,589 \cdot 10^{-32}$		
a_{14}			$5.645\,295 \cdot 10^{-36}$		

Table 4.1: Polynomial interpolation of Cu properties (note $k_{fit} \iff T \geq 90\,\mathrm{K}$)

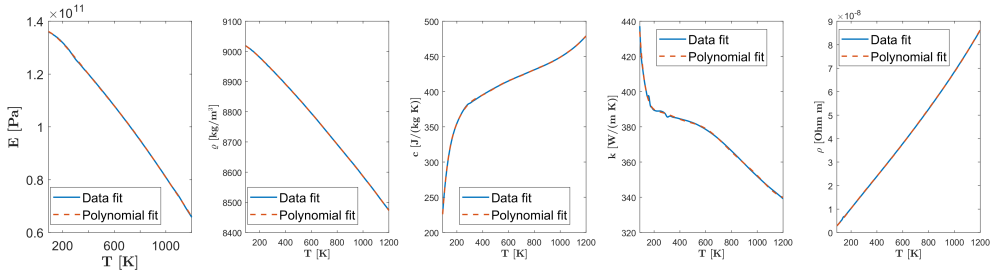

Figure 4.17: Polynomial fitting

5. Orbital Mechanics

We are insignificant creatures on a small rock orbiting a very average star in the outer suburbs of one of a hundred thousand million galaxies.

— S. W. Hawking, 1995

5.1 Introduction

The celestial mechanics is an astronomy branch that deals with the definition of the motion of celestial bodies. The study of orbital mechanics is located within the latter; this subcategory has the main purpose of studying the motion of a spacecraft and its maneuvering under the gravitational influence of one or more celestial bodies.

For this purpose, reference is often made to Newton's law of universal gravitation, starting with a simple approximate problem known as Two-Body Problem (2BP), and then extending the treatment to more complex scenarios.

In the 2BP the spacecraft is supposed to be subject to the sole gravitational attraction of a main body. In the Three-Body Problem (3BP) two main bodies simultaneously influence the temporal propagation of the orbit of the less massive third body, that is, the spacecraft. The Restricted Three-Body Problem (R3BP) assumes that the spacecraft has negligible mass, and in the Circular Restricted Three-Body Problem (CR3BP) the hypotesis of circular orbits is appended to the latter.

Describing an orbit implies the definition of references, both for space and time. There are appropriate reference systems (RSs) based on the specific study to be conducted; for example, the study of a planet's orbit around the Sun would require a heliocentric RS, while the study of a satellite around the Earth would require a geocentric one. The starting point for the definition of a RS is to define its origin, the orientation of the fundamental planes and the principal direction[1]. Please note that, sometimes, the terms RS, reference frame (RF), and coordinate system (CS) may be used as synonyms; in the present analysis, reference is made to the notation adopted by NASA's Navigation and Ancillary Information Facility (NAIF)® in the SPICE® software (SPICE 2018), i.e. a RS, or RF, is given by the definition of the three axes, while a CS describes how a specific point is located in the RS.

Furthermore, RSs can be inertials –not rotating wrt fixed stars and their origins have negligible accelerations, assumed null– or non-inertials.

[1]By defining the principal direction it is also defined the entire triplet of coordinates, since a RS has a dextral orthogonal triad (DHT) for the vast majority of situations

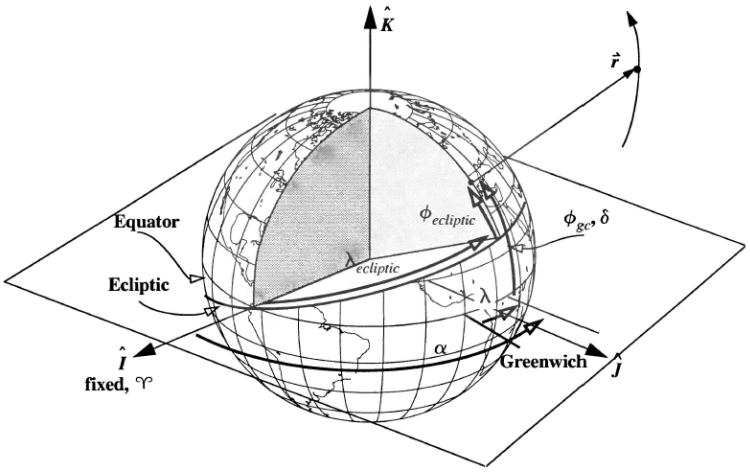

Figure 5.1: Earth equator and ecliptic planes (Vallado 2007)

In Fig. 5.1 is shown the Earth with both the equator plane, perpendicular to the axis of rotation, and the ecliptic plane, defined by the average position of the Earth during the revolution around the Sun. The two are inclined by about 23.5° (the approximate value is due to Earth's rotation axis precession).

The position of a site on the ground is identified by its North-South geocentric latitude φ_{gc} and East-West longitude λ, where $0° \leq \lambda \leq 360°$ if eastbound, or between $\pm 180°$ if East-West. A constant line of longitude is a meridian, of which Greenwich is the prime meridian, and a constant line of latitude is a parallel. Depending on whether the reference plane is the equator or the ecliptic, the two are referred to as simply latitude φ and longitude λ in the first case, or ecliptic ones φ_{ecl}, λ_{ecl} in the second. Sometimes the ecliptic parameters refer to the celestial sphere (Vallado 2007); in this case the terrestrial equatorial plane is extended into the celestial one, and positions are evaluated with the right ascension α, from the vernal equinox Υ, and the declination δ (wrt the equatorial plane, as λ and φ). As in Fig. 5.1, a generic site has position vector $\boldsymbol{r}_{site}$ defined by

$$\boldsymbol{r}_{site} = \begin{bmatrix} r\cos\varphi\cos\lambda \\ r\cos\varphi\sin\lambda \\ r\sin\varphi \end{bmatrix} \tag{5.1}$$

For example, the sunny Pasadena, with $\{\varphi, \lambda\} = \{34° \; 8' \; 52'' \text{ N};\; 118° \; 8' \; 37'' \text{ W}\}$, is located at $\boldsymbol{r}_{Pas} = \{-2.4870, -4.6492, 3.5762\} \cdot 10^3$ km.
Trani, a charming Pugliese resort in Italy, has $\{\varphi, \lambda\} = \{41° \; 17' \; 0'' \text{ N};\; 16° \; 25' \; 0'' \text{ E}\}$, or $\boldsymbol{r}_{Tra} = \{4.5924, 1.3531, 4.2035\} \cdot 10^3$ km.

In this particular analysis the focus in on the SC.
It is positioned at $\{\varphi, \lambda\} = \{89° \; 40' \; 12'' \text{ S};\; 129° \; 46' \; 48'' \text{ E}\}$ or, equally, it is located at at the Moon's south –really south– pole at $\boldsymbol{r}_{SC} = \{-6.4012, 7.6884, -1736.97\} \cdot 10^3$ km.

For the considerations made at the end of this Chapter, the analysis on the RS and the time is left out and postponed to future studies.

5.2 Two Body Problem

It may be stated that the two greatest steps forward in understanding the celestial mechanics are the contributions of Kepler and Newton. The first, Kepler, in different treatises and different years (*Astronomia Nova* in 1609 and *Harmonices Mundi Libri V* in 1619), described the kinematics of motion of celestial bodies in his famous three laws

1. The orbit of a planet is an ellipse with the Sun at one of the two foci	*Ellipsin fieri orbitam planetae [. . .] Sole foco altero huius ellipsis*
2. The line joining the planet to the Sun sweeps out equal areas in equal times	*Arcum ellipseos, cujus moras metitur area AKN, debere terminari in LK, ut sit AM*
3. The square of the orbital period of a planet is proportional to the cube of its orbit's semimajor axis	*Proportio qua est inter binorum quorumcunque planetarum tempora periodica, sit praecise sesquialtera proportionis mediarum distantiarum*

The dynamics of motion was studied, understood, and pusblished years later by Sir Isaac Newton in his equally fundamental three laws of dynamics. In his *Philosophiae Naturalis Principia Mathematica*, in 1687, the three laws were described as

1. Every body perseveres in its state of rest, or of uniform motion in a right line, unless it is compelled to change that state by forces impressed thereon	*Corpus omne perseverare in statu suo quiescendi vel movendi uniformiter in directum, nisi quatenus illud a viribus impressis cogitur statum suum mutare*
2. The alteration of motion is ever proportional to the motive force impressed; and is made in the direction of the right line in which that force is impressed	*Mutationem motus proportionalem esse vi motrici impressæ, et fieri secundum lineam rectam qua vis illa imprimitur*
3. To every action there is always opposed an equal reaction: or the mutual actions of two bodies upon each other are always equal, and contrary directed	*Actioni contrariam semper et aequalem esse reactionem: sive corporum duorum actiones in se mutuo semper esse aequales et in partes contrarias dirigi*

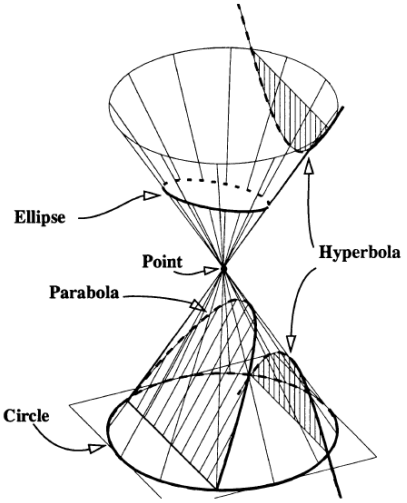

Figure 5.2: Conic sections (Vallado 2007)

The first law of Kepler guides the following treatment: the planets move on elliptical orbits and the Sun occupies one of the two foci. An ellipse is a conic section and, more precisely, as will be clear once introduced Newton's law of Universal Gravitation, the ellipse is just one of the possible conic sections that can define an orbit. For example, as shown in Fig. 5.2, artificial satellites can have circular, elliptic, parabolic, or hyperbolic orbits, drawn from the intersection of a plane and a cone –from which derives the name–. Only the point and any straigh line tangent to the cone surface are not physically viable orbits.

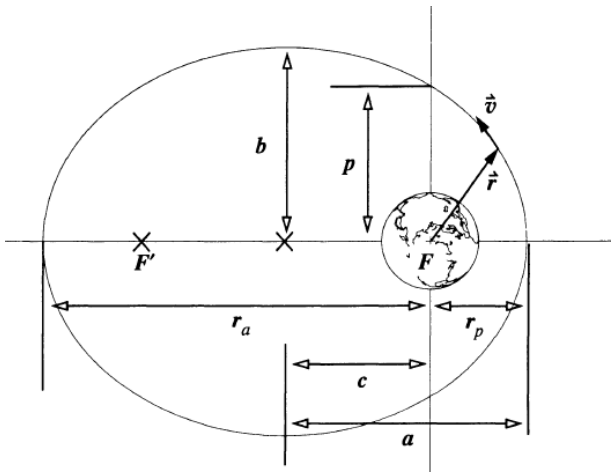

Figure 5.3: Geometry for conic sections (Vallado 2007)

The conic equation, often called in orbital mechanics trajectory equation, is known

$$r = \frac{p}{1 + e\cos\nu} \tag{5.2}$$

In Fig. 5.3 the geometry of an ellipse is shown. Neglecting the geometric treatment, the most important parameters in orbital mechanics are the Semimajor Axis (SMA) a, the Semiminor Axis (sma) b, the r_p and r_a radii, respectively periapsis and apoapsis, the eccentricity e, which defines the "flattening" of the ellipse, and the semilatus rectum p –or semiparameter–. From the conic, eq. (5.2), it is inferred that the periapsis and apoapsis are the two extreme values of the radius r such that

$$\begin{cases} r_p = \dfrac{p}{1 + e\cos 0} = \dfrac{p}{1+e} & \nu = 0 \\ r_a = \dfrac{p}{1 + e\cos\pi} = \dfrac{p}{1-e} & \nu = \pi \end{cases} \tag{5.3}$$

where ν is the true anomaly, which defines the position of the satellite in its orbit.

From other geometrical considerations,

$$p = a\left(1 - e^2\right) \tag{5.4}$$

by joining eqs. (5.3, 5.4)

$$\begin{cases} r_p = a\,(1-e) \\ r_a = a\,(1+e) \end{cases} \tag{5.5}$$

from which

$$e = \frac{r_a - r_p}{r_a + r_p} \tag{5.6}$$

Finally, from Fig. 5.3, it can be graphically seen the relationship

$$2a = r_p + r_a \tag{5.7}$$

So far, only closed orbits have been treated, namely ellipses; dealing with circumferences –degenerate ellipses– should show a similar trend. Controversely, parabolas and hyperboles are open orbits, and a satellite would not retrace indefinitely the same path over time. The parabola is really more an ideal case that acts as a watershed between closed and open orbits; hyperbolas, on the other hand, allow to escape from a Sphere Of Influence (SOI).

Briefly, the characteristics of each conic section are presented in the Table below.

ORBIT	e	a
Circle	$e = 0$	$a = r$
Ellipse	$0 < e < 1$	$r_p < a < r_a$
Parabola	$e = 1$	$a = \infty$
Hyperbola	$e > 1$	$a < 0$

Table 5.1: Types of orbits (values of conic sections)

It is possible to add to the considerations just made, following the first Kepler's law, that the second law of Newton, in conjunction with his law of Universal Gravitation, serves as a starting point for the study of orbital mechanics. Let m_1 and m_2 be two massive point bodies separated by a distance r. The two laws can be expressed as follows

$$\sum \boldsymbol{F} = \frac{d(m\boldsymbol{V})}{dt} = m\boldsymbol{a} \qquad \boldsymbol{F}_g = m\boldsymbol{a} = -G\frac{m_1 m_2}{r^2}\frac{\boldsymbol{r}}{|\boldsymbol{r}|} \tag{5.8}$$

Through some mathematical steps the relative acceleration is

$$\ddot{\boldsymbol{r}} = -G\frac{m_1 + m_2}{r^2}\frac{\boldsymbol{r}}{r} \tag{5.9}$$

The restricted problem hypotesis is introduced, implying that one body has significantly lower mass than the other, such as a satellite around a central body –like the Earth–. If $m_2 \ll m_1$, the gravitational parameter $\mu = GM$, where M is the greater mass among the two bodies, is introduced into eq. (5.9) leading to

$$\ddot{\boldsymbol{r}} = -\frac{\mu}{r^2}\frac{\boldsymbol{r}}{r} \tag{5.10}$$

eq. (5.10) is known as relative two-body equation. The eq. (5.10) is a NL second-order ODE, implementable in a Matlab® ODE solver, preferably `ode113`. By dividing the acceleration in the three spatial coordinates, it can be written (Curtis 2013)

$$\begin{cases} \ddot{x} = -\dfrac{\mu}{r^3}x \\ \ddot{y} = -\dfrac{\mu}{r^3}y \\ \ddot{z} = -\dfrac{\mu}{r^3}z \end{cases} \quad \text{with } r = \sqrt{x^2+y^2+z^2} : \; \boldsymbol{f}(t,\boldsymbol{y}) = \left[\dot{x} \;\; \dot{y} \;\; \dot{z} \;\; -\frac{\mu}{r^3}x \;\; -\frac{\mu}{r^3}y \;\; -\frac{\mu}{r^3}z\right] \tag{5.11}$$

For the 2BP it has been said that the main hypothesis is that the mass of the orbiting body is negligible compared to that of the main one. Moreover, the bodies are supposed with spherical simmetry, and therefore point-like, and the only force existing is the gravitational, in eq. (5.8). Assuming an intertial RS, the specific angular momentum $\boldsymbol{h}$ is

$$\boldsymbol{h} = \boldsymbol{r} \wedge \boldsymbol{V} \tag{5.12}$$

which is mass independent. Since $\boldsymbol{r}$ and $\boldsymbol{V}$ define the orbital plane, $\boldsymbol{h}$ must be always perpendicular to it. Furthermore, this values is always constant and conserved in the 2BP, and therefore provides a proportionality factor between the two quantities.

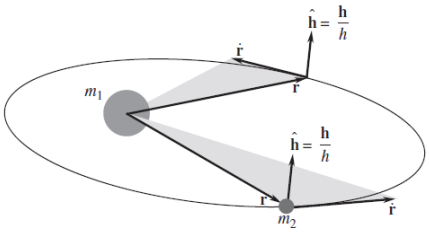

Figure 5.4: Specific angular momentum conservation in an orbit (Curtis 2013)

By rearranging the eq. (5.10), the specific mechanical energy of an orbiting body is

$$\xi = \mathcal{T} - \mathcal{U} = \frac{V^2}{2} - \frac{\mu}{r} \tag{5.13}$$

The eq. (5.13) is called integral equation, or vis-viva (living force). Both kinetic $\mathcal{T}$ and potential $\mathcal{U}$ specific energies can be noted. An alternative formulation is

$$\xi = -\frac{\mu}{2a} \tag{5.14}$$

always defined except for parabolic orbits. For elliptic orbits, therefore, the orbital velocity V is unequivocally defined by the specific position, r, and the orbit itself is uniquely defined by the SMA a. Therefore, by joining eqs. (5.13, 5.14) and solving for V

$$V = \sqrt{2\left(\frac{\mu}{r} + \xi\right)} = \sqrt{\mu\left(\frac{2}{r} - \frac{1}{a}\right)} \tag{5.15}$$

For circular orbits $a = r$, and therefore the eq. (5.15) is reduced to the simpler

$$V_c = \sqrt{\frac{\mu}{r}} \tag{5.16}$$

which is the velocity in a circular orbit of radius r, equal in every point.

Another important detail is that the visviva equation can be used in two different points of the same orbit. For example, let the following be the equation for a parabolic orbit

$$\xi = \frac{V_E^2}{2} - \frac{\mu}{r_p} = \frac{V_\infty^2}{2} - \frac{\mu}{r_\infty} = 0 \tag{5.17}$$

where the lhs refers to the periapsis and the rhs to the parabola "infinity". Since $r_\infty = \infty$ by definition and, unlike the hyperbola, the hyperbolic excess of velocity is $V_\infty = 0$ for a parabola, then from eq. (5.17) is possible to obtain the minimum speed necessary to reach a central body's SOI, namely the escape speed V_E.

$$V_E = \sqrt{2\frac{\mu}{r}} = \sqrt{2}V_c \tag{5.18}$$

From the second and third Newton's law, instead, it is possible to derive the orbital time, or simply the period $\mathcal{T}$.

$$\mathcal{T} = 2\pi\sqrt{\frac{a^3}{\mu}} \tag{5.19}$$

The analysis could continue with the definition of Keplerian orbital parameters and with the introduction of Lagrangian and Hamiltonian mechanics. This would allow the introduction of the 3BP and, with the addition of a trajectories study from the moment of launch to a certain point in the Earth-Moon system, would allow to study the payload position propagation with more precision. Moreover, it would also allow to study the suborbital trajectories to move the payloads between hypothetical multiple lunar bases, as well as the various uses that payloads could have (return to Earth, positioning in a well-defined parking orbit, near the Lagrangian points, etc...). This interesting but complex study, already started, is postponed to subsequent studies.

In the continuation of the analysis, the eq. (5.18) will be used to calculate an approximate value to be attributed to the burnout speed, i.e. the speed that the EML must guarantee at every payload.

6. The Moon

Shoot for the moon; you might get there.

— B. Aldrin

6.1 The environment

The Moon has many peculiar characteristics that can be taken into account during the design phase of a permanent base and, in the specific case, of a MD.

The positioning of a MD inside the SC, at the lunar south pole, eq. (5.1) creates a well-defined environment scenario. For example, the edge of the SC is almost perpetually illuminated, while inside it is mainly dark (Haruyama et al. 2008). Moreover, the Moon always shows the same side for an observer on the Earth[1]. This information, in conjunction with the quasi-circular lunar orbit with low orbital inclination, allows to have launch windows almost constant, in first approximation. SC is a truncated cone-shaped crater and has an outer radius of ≈ 10.5 km, a basement radius of ≈ 3.3 km, and a depth of ≈ 4.2 km, hence the inner wall slopes is

$$\delta_{SC} \approx 30^{\circ} \tag{6.1}$$

The Moon lacks an atmosphere, which eliminates the problems related to atmospheric friction and ideally does not place aerothermodynamics limits at the speeds reachable near the lunar ground. In addition, the lunar gravity is less than 20% compared to the Earth's one, reducing the deceleration during the launch proportional to the $\sin(\delta_{SC})$.

With reference to SC, lighting conditions play both in favor and against its design. As already shown in Chapter 4, the thermal phenomena are extremely relevant and must be kept under close observation. The fact that the SC has a permanently shadowed region (PSR) implies an average temperature of 90 K, leaving a wide margin of heating before reaching prohibitive temperatures for the materials themselves. At the same time, the energy needed to operate the MD derives from solar lighting, and therefore it is necessary to place solar panels outside the crater and to have energy distribution systems.

The set of all these phenomena, including their variations during the lunar orbital period, have been left out in this feasibility study. Nevertheless, it was noteworthy to mention them at the beginning of the Chapter to point out how many factors are interconnected.

[1]This phenomenon is called tidal locking: in the Earth-Moon gravitational interaction, over time the latter has lost a net component of rotation wrt that of Earth and has a synchronous rotation –except for the librations due to the eccentricity of the lunar orbit–.

6.2 Orbital characteristics

From eq. (5.18) it is obtained

$$V_{E,☾} = 2.3757\,\mathrm{km\,s^{-1}} \tag{6.2}$$

from the surface, where $r_{☾} = 1.7374 \cdot 10^3\,\mathrm{km}$.

An estimated launch velocity, to confirm with future studies, for example, for the fluctuations due to the launch time or due to the effective destination, can be set to be

$$V_{bo} = 2.500\,\mathrm{km\,s^{-1}} \tag{6.3}$$

This speed is the one that will be set as minimum at the launch and on which the sizing of the MD will be performed. It is noteworthy that $V_{bo} > V_{E,☾}$ and, therefore, the generic payload has a hyperbolic excess speed, so it manages to exceed the SOI radius of the Moon (Bate et al. 1971), namely

$$r_{SOI} = a_{☾} \left(\frac{m_{☾}}{m_{⊕}}\right)^{\frac{2}{5}} \frac{1}{\sqrt[10]{1 + 3\cos(\vartheta)^2}} \in [5.7674, 6.6244] \cdot 10^4\,\mathrm{km} \tag{6.4}$$

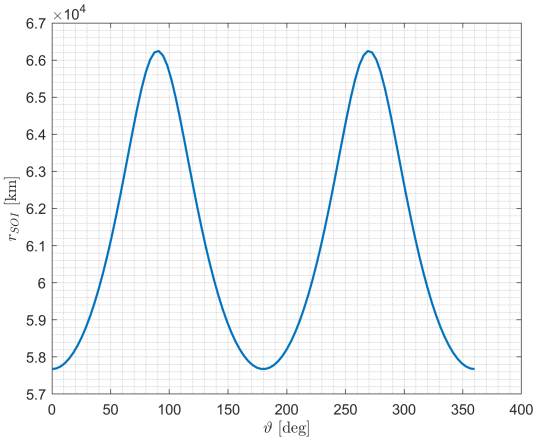

Figure 6.1: Moon SOI function of relative position wrt Earth

It is known that the SOI is a mathematical generalization and that this region of space, in which the sole attraction of the relevant body is supposed to exist, can vary its shape as the position of the orbiting body changes around the principal. The formulation in eq. (6.4) provides the radius of the SOI according to the relative angular position ϑ of the Moon wrt Earth.

For this dissertation it is sufficient to state that the payload will succeed in overcoming the maximum distance of the SOI, eq. (6.4).

7. Mass drivers

The science of today is the technology of tomorrow.

— E. Teller

7.1 Introduction

An electromagnetic launcher is a device capable of accelerating payloads to high velocities with electromagnetic forces. Recent developments and advances in energy and magnet technology make electromagnetic acceleration a viable alternative to chemical rocket space launch -or similar tasks-, usually characterized by massive engines and the use of a substantial quantity of propellant.

One of the main advantages in using EMLs, in place of conventional accelerating systems, is to have no limitations, or minor ones, in the payload size and final launch speed that can be achieved, especially in environments without friction, i.e., space or lunar surface. Indeed, unlike chemical propulsion, these do not depend on Tsiolkowski's equation (Kolm et al. 1980).

In the last decades, two different types of EMLs have been analyzed, with various alternative solutions and improvements. In turn, these types fall into two categories depending on their use. In the first place, the distinction between railguns (RGs) and coilguns (CGs) depends on the type of electromagnetic interaction that is used to accelerate the payload. A device that expels a mass to get by reaction an acceleration is called a reaction engine, which can be useful, i.e., to provide ΔV for space missions. If, on the other hand, the device aim is to provide kinetic energy to the launched mass and not to the accelerator itself, thus by discharging the reaction force to the ground, then it is referred to as a MD. This last category is of interest in this analysis.

The use of a MD does not have only energetic advantages. Even if it launches a payload without consuming chemical propellant to counteract the force that keeps the payload on the ground, it is also true that the use of electromechanical energy allows avoiding harmful gas emissions that could, in the long run, set up an unwanted lunar atmosphere (O'Neill and O'Leary 1977; O'Neill, Billingham, et al. 1979).

Furthermore, the possibility to power the MD system with solar energy, converted by solar panels, and the implementation of appropriate choices, to guarantee high reliability, efficiency and a high degree of reusability of the component (Chilton 1977), show how this technology can become extremely useful and efficient for the future of space exploration.

7.2 Railgun

The railgun, or Lorentz rail accelerator, is the most heavily studied hypervelocity launcher technology over the last decades. The reason is that a railgun is a relatively simple device to convert electric energy into kinetic and to obtain high performances (Lianos and Brown 1994; He et al. 2010; Morgan 1997).

The railgun, in its simplest version, consists of two conductive rails and a sliding conductive armature that moves with a sliding contact on them.

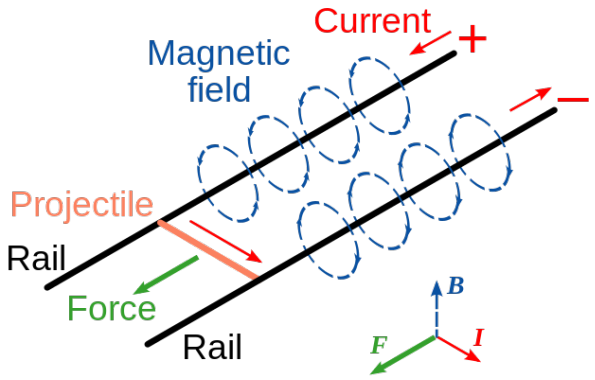

Figure 7.1: Railgun scheme

The principle of railgun operation bases itself on the Lorentz force (2.7). Referring to Fig. 7.1, the armature closes the circuit between the two rails, allowing the current flow. According to Biot-Savart law (2.5), this current induces a circumferential magnetic field, which results in a pushing force on the armature itself. The main advantages in the use of a railgun are its simplicity and acceleration capability. Moreover, the RG bases its acceleration principle on an electrical basis, allowing the payload or its container to be conductive but not necessarily ferromagnetic –even though the use of the latter would increase the performances even if limited by the magnetic saturation, Section 2.7–.

There are, however, few disadvantages, especially if great energies are needed. For the same acceleration principle, the current throught the rails creates a force that tends to repel each binary from the other. Moreover, using high currents may create a plasma arc which may bypass the payload, leaving it behind. Resistive and inductive losses increase with the length of the RG and a speed saturation is noticeable, given that railguns behave as large inductors whose inductance is proportional to the area enclosed by the armature and the barrel. The sliding contact between armature and projectile creates friction and erosion, strongly damaging and deteriorating the rails and making a multishot scenario a difficult task (Masugata 1997). Finally, the acquired kinetic energy by the projectile cannot exceed the magnetic energy left behind, thus limiting the efficiency.

The top speed and the efficiency can be increased by connecting shorter rails in series, each one connected to a dedicated power supply. Further improvements can be obtained with the use of more complex geometries, starting from an ideal cylindrical geometry, then using curved rails in pairs of two or four that contain a cylindrical payload, or even implementing models with their own name, like the helical railgun (Baum 2007). Nevertheless, it is immediate to notice the analogy between these cylindrical geometry improvements and the native configuration of the CG, which is analyzed from now on.

7.3 Coilgun

The term CG defines the class of EMLs which may improve railguns characteristics and overcome limitations in some applications. The CG is an EML which uses the magnetic interaction to accelerate the payload and, as a secondary effect, to make it levitate; CGs are made of drive coils, that are solenoid portions in which the current pulses and produces a magnetic field that interacts with the payload.

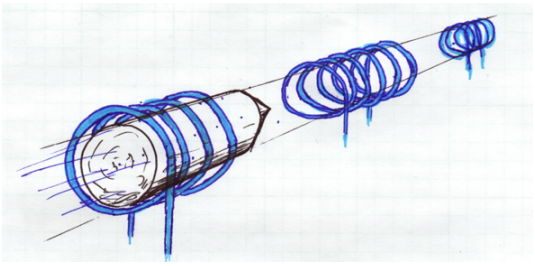

Figure 7.2: Schematic coilgun representation

Referring to Fig. 7.2, the solenoid portions fixed at specific points of the system are the drive coils. The payload, on the other hand, is contained in the so-called bucket, a subsystem constituted by the payload itself and the armature that holds and/or pushes it. The bucket radius is smaller than the drive coils' one, allowing it to pass through them.

CGs base their operating principle on the classic electromagnetic laws. The force acting on the bucket is given by the following formulation (O'Neill, Billingham, et al. 1979)

$$F = \frac{dM}{dx} I_b I_d \tag{7.1}$$

In the simplest way, a CG design can be divided into two categories as follows.

Depending on the material of the bucket, i.e. the payload container, CGs are divided into reluctance and inductance. The first ones use a ferromagnetic projectile, which is heavy and subject to magnetic saturation; moreover, due to the dipoles orientation, it may work only with a pulling force, and the magnetic field generated by the drive coils has to be quenched when the bucket reaches their center, otherwise it would be pulled back.
The second version, the inductance, does not need a ferromagnetic payload; the bucket may be magnetized inductively and, then, can produce its magnetic field which can interact with the one from the drive coils. If the bucket is wrap with another coil, the bucket can be made of any material and it is possible to achieve both a pulling and a pushing force; this is the configuration studied in this analysis, the so-called Push-and-Pull Inductance (PPI). By charging inductively the bucket before the launch, the PPI bucket coil has a decaying current in its windings and the current in the drive coils can be timely pulses so that the bucket is attracted during the approach and rejected when leaving.

In this framework lies one of the main characteristics in CGs: the inversion of the current. The mutual inductance gradient, one of the three factors contributing to the force exerted on the bucket calculation (Fig. 2.16, eq. (7.1)), is antisymmetrical over the traveled space: it follows that by mantaining constant the current values, the same attractive force produced in the approaching part is experienced in the leaving part, stopping completely the payload. Hence the need to commute, or reverse, the current.

7.3.1 Reluctance coilgun

A reluctance accelerator consists of a series of solenoid portions in which the bucket passes through. The principle of operation is based on the magnetization of the drive coils by means of a rapidly supplied electrical pulse which produces a magnetic field that attracts the bucket –ferromagnetic–, accelerating it in its path. The acceleration principle is based on the variation of reluctance during the advance (Bresie and Andrews 1991).

Materials with low reluctance, i.e. materials with a high coefficient of magnetic permeability, concentrate great part of the magnetic flux inside themselves, generating temporary poles that are attracted to areas with higher magnetic flux density, that is, the drive coil center. The flux actually concentrates in the material and not in the surrounding air because the former has a superior magnetic permeability. It is worth pointing out that the bucket can only be attracted, because even by reversing the direction of the current, once overtaken the center of the drive coil, would generate reversed poles in the bucket. Therefore, reluctance CGs are only able to generate pulling forces and have to quench the current as fast as possible -usually by switching off the voltage and closing the circuit with a diode, in the simplest scenario- when the center of the bucket approaches the center of the drive coil. This leads to a "spatial" efficiency at most equal to 50%.

Moreover, as mentioned in Section 2.7, the ferromagnetic materials fall into saturation if the applied magnetic field is too intense; i.e., iron reaches magnetic saturation around a magnetic field of $\approx 2\,\mathrm{T}$. All other materials, with higher reluctance, saturate in advance.

Diverse studies are present in literature about the reluctance CG (Bresie and Andrews 1991; Daldaban and Sari 2014; Barrera and Beard 2014). In many of these references, more and more precisely with the advancement of the publication year, it is stated that the reluctance CG technology is the most advanced and efficient at engineering and constructive level, among the CGs, but has many limitations due to its operating principles. One on all is saturation, which limits the maximum magnetic field intensity and, therefore, the maximum force on the bucket. The second is that the pull-only mode causes drive coils to span twice as much the bucket is accelerated. The third, which follows the foregoing considerations, is that as the bucket accelerates the current quenching is increasingly faster in order to avoid the so-called suckback effect. In other terms, the force density of the reluctance CG is lower than other CG classes, and also compared to the more advanced railguns.

Another fundamental consideration is that all electromagnetic phenomena, in the presence of ferromagnetic elements, become strongly NL. It seems that this technology is best suited for use with low-mass high-accelerated payloads.

All of these considerations push the author to devote more attention to the latest CGs developed, the induction CGs.

7.3.2 Quenchgun

Before proceeding to the configuration chosen for this analysis, the PPI CG, it is right to point out that there are still better solutions, to be improved to date from the point of view of realization, but promising. These are the technologies that require the use of superconducting materials in the drive coils, which would allow obtaining improvements on power needs and TRL (Andrews and Devine 1991). Nonetheless, the focus is still on the PPI CG, as it may be more efficiently implemented and cheaper in the immediate future.

One of the major issues in the use of standard materials for CGs is the energy supply method. In particular, the bucket plays only the role of the receiver, letting the current it has inside to drop with a decay rate dictated by the parameters of the LR circuit of its wire windings. While this energy can be provided somehow in a short time, it becomes more difficult to do the same with the drive coils, in much less time and with large energy discharges, given that the storage devices are capacitors, which are extremely inefficient, that is, they have low energy densities, when they have to provide large amounts of charge in a short time.

The use of quenchguns aims to overcome this limitation, changing the place for storing energy and how this electrical energy behaves over time. Quenchguns, more precisely defined as superconductive quenchgun (SQ), are EMLs that use superconductor materials in drive coils: in this way the electrical energy can be stored inside them, eliminating the use of external power storage devices (Korsmeyer et al. 1990).

Superconductors can conserve energy ideally for an indefinite period of time and can be recharged between two consecutive launches, requiring minor energy compared to traditional CGs. Additionally, while in conventional CGs the huge energy impulse must be supplied by a pulsed alternator or a flywheel, both subject to erosion, the superconducting barrels can be effectively powered directly by the energy generated by solar panels (Snow and Kolm 1992).

Another important feature that improves energy and the mere constructive cost considerations is that the bucket does not necessarily have to be provided with wires made of superconducting materials, provided their time costant is greater than the launch time. In the last cited study, it can be noted that many advantages can be obtained in the use of aluminium or beryllium alloys for bucket coils, provided that they are pre-cooled to about -195° C. While this study is based on the MD positioning at the lunar equator, where the environment is warmer than the point in which the present analysis is discussed, the SC has temperature in the PSRs of about -183° C, and therefore this constraint is roughly envisioned by the environment itself. At the most, it will be needed to maintain this temperature while charging the drive coils before each launch.

Notice how this study can be interesting to investigate in the future. It has been postulated that quenchguns can reach efficiencies $\eta_{QG} > 90\%$ (Davis 2018).

7.3.3 Push-and-Pull inductance coilgun

Since the probable pilot paper (O'Neill and O'Leary 1977) regarding the CGs, this alternative EML model has been studied as an improvement of the RG. CGs are formed by a payload, the bucket, which is accelerated by the electromagnetic interaction with one or more drive coils in which a great current pulses, producing a strong magnetic field. There are two CG families, reluctance, and inductance. The difference between the two lies in the material with which the bucket is made. In the reluctance coilguns the bucket is composed of a ferromagnetic material -or equipped with permanent magnets- that is attracted by the drive coils. In Paragraph 7.3.1 are presented the preliminary reasons for which in the analyzed framework it would be preferable to exploit the CG configuration.

In the inductance model, the payload is non-ferromagnetic and is wound by an additional coil, in which the current flows. This configuration, analyzed in (O'Neill and O'Leary 1977; O'Neill, Billingham, et al. 1979; Kolm et al. 1980), is the subject of the present analysis.

The study focuses on the PPI CG model for several reasons: for the lunar launch scenario, the CG is better than the RG for high-cycle launch applications, due to issues related to the component deterioration. Moreover, inductance CGs are the most suitable for high-speed applications, as they eliminate the high weight of ferromagnetic materials, they do not have magnetic saturation problems, and they do not have long-lasting transients as for ferromagnetic cores during the hysteresis cycle.

7.3.4 Carrier deceleration

Ultimately, it may be noted that the bucket containing the payload is an element that would be useful to keep in the vicinity of the launcher, without dispersing it with the payload itself. Thanks to the electromagnetic interaction it could be assumed to leave the front part of the bucket open so that, once the launch speed is reached, the bucket itself can be decelerated by means of opposing magnetic fields and stored for successive operations; the opening would allow the payload to escape, ideally without misalignments and perturbations.

This study, already deepened in the first papers about CGs (Snow, Dunbar, et al. 1982; Snow and O'Neill 1979), is certainly interesting and deserves a more profound analysis.

8. Lunar mass driver case study

Let's face it, space is a risky business. I always considered every launch a barely controlled explosion.

— A. Cohen

8.1 Mathematical model

Please remember the difference between ρ and ϱ, respectively resistivity and material density. The notation with subscripts $A_{x,y}$ indicates that A refers to the element b, while y, if present, specifies the distinction between different types of A. For example, $T_{b,w}$ indicated the temperature of the wires in the bucket, while $T_{d,w}$ the temperature of the wires in the drive coils.

It is possible to write a series of ODEs to be simultanously satisfied to model the MD physical phenomena as realistically as possible. A condition to be certainly verified is the decay over time of the bucket current, which is not fed with a potential during its motion. The current circuit equation in the drive coils can be "omitted" as it is supposed to be forced. It will be interesting, however, to consider how the two currents will generate a proportional force on the bucket. Obviously, it will be essential to consider the thermal phenomena: the currents certainly cause a temperature rise, which affects the resistance of the cables and, therefore, the whole phenomenon.

A more realistic model of electromagnetic and mechanical phenomena in a MD shows an interdependence between the bucket velocity V and the current I_b flowing in its coil windings.

The drive and bucket coil circuit equation can be expressed in matricial form as (Andrews and Devine 1991)

$$\begin{Bmatrix} \mathcal{V}_d \\ \mathcal{V}_b \end{Bmatrix} = \left(\begin{bmatrix} L_d & 0 \\ 0 & L_b \end{bmatrix} + \begin{bmatrix} 0 & M \\ M & 0 \end{bmatrix} \right) \frac{d}{dt} \begin{Bmatrix} I_d \\ I_b \end{Bmatrix} + \begin{bmatrix} R_d & 0 \\ 0 & R_b \end{bmatrix} \begin{Bmatrix} I_d \\ I_b \end{Bmatrix} + V \begin{Bmatrix} I_b \\ I_d \end{Bmatrix} \frac{d}{dx} \begin{bmatrix} 0 & M \\ M & 0 \end{bmatrix} \tag{8.1}$$

or, likewise,

$$\begin{Bmatrix} \mathcal{V}_d \\ \mathcal{V}_b \end{Bmatrix} = \left(\begin{bmatrix} L_d & 0 \\ 0 & L_b \end{bmatrix} + \begin{bmatrix} 0 & M \\ M & 0 \end{bmatrix} \right) \frac{d}{dt} \begin{Bmatrix} I_d \\ I_b \end{Bmatrix} + \begin{bmatrix} R_d & 0 \\ 0 & R_b \end{bmatrix} \begin{Bmatrix} I_d \\ I_b \end{Bmatrix} + \begin{Bmatrix} I_b \\ I_d \end{Bmatrix} \frac{d}{dt} \begin{bmatrix} 0 & M \\ M & 0 \end{bmatrix} \tag{8.2}$$

$$\begin{cases} \mathcal{V}_d = L_d \dfrac{dI_d}{dt} + M \dfrac{dI_b}{dt} + R_d I_d + V I_b \dfrac{dM}{dx} \\ \mathcal{V}_b = L_b \dfrac{dI_b}{dt} + M \dfrac{dI_d}{dt} + R_b I_b + V I_d \dfrac{dM}{dx} \end{cases} \tag{8.3}$$

Unless considering the $t < 0$ condition –bucket coil charging period–, the bucket as no potential applied during its motion, and therefore $\mathcal{V}_b = 0$. The current in drive coils, instead, is forced. It follows that the variation of current over time in the bucket is given by the following formulation

$$\frac{dI_b}{dt} = -\frac{1}{L_b}\left(R_b I_b + M \frac{dI_d}{dt} + I_d \frac{dM}{dt}\right) \tag{8.4}$$

From the magnetic energy stored in a circuit it can be deduced the force on the bucket (7.1), and, therefore, another ODE. It follows

$$a = \frac{dV}{dt} = \frac{F}{m} = \frac{1}{m}\frac{dM}{dx} I_d I_b \tag{8.5}$$

The gravity of the moon, $g_{\leftmoon} = 1.625\,\mathrm{m\,s^{-2}}$, scaled with the $\sin\delta$ of the launch angle deducted in the eq. (6.1), has to be subtracted from eq. (8.5) in the lhs, leading to

$$\frac{dV}{dt} = \frac{1}{m}\frac{dM}{dx} I_d I_b + 1.625 \sin\delta \tag{8.6}$$

For optimized geometries, the mutual inductance gradient $dM_{,x}$ can reach values of about $1 \cdot 10^{-5}\,\mathrm{H\,m^{-1}}$. To obtain an acceleration comparable to the gravity one, for example, it would be necessary to have the product of the currents about five orders of magnitude higher than the mass values.

The eq. (2.24) allows to find the energy needed to operate the drive coils, namely

$$\frac{dW_d}{dt} = P_d = R_d(T) I_d^2(t) \tag{8.7}$$

while the energy needed to charge, at $t = 0$, the wires in the bucket, is governed by the equation

$$I_{b,charge}(t) = \frac{\mathcal{V}_s}{R_b}\left(1 - e^{-\frac{R_b t}{L_b}}\right) \tag{8.8}$$

where t_f can be assumed equal to 5 time constants, eq. (2.39), which is the conventional time to reach the steady state value. Moreover, the following condition must be respected

$$\mathcal{V}_s = I_{b0} R_b \tag{8.9}$$

Therefore, the energy needed to charge the bucket coil can be written as

$$\frac{dW_b}{dt} = P_b = R_b(T)\left[I_{b0}\left(1 - e^{-\frac{R_b t}{L_b}}\right)\right]^2 \tag{8.10}$$

Another equation that is convenient to implement is the heat equation, eq. (4.3). Assuming that the heat produced inside the wires depends solely on the thermal dissipation due to the Joule effect –reasonable consideration given the analysis made in Chapter 4–, it is possible to obtain the (8.39). Indeed, the thermal conduction and radiation phenomena, specifically the eqs. (4.24, 4.26), are neglected for short times as the ones in the MD launch. By writing the resistance in explicit form, the length of the cables is eluted and it is obtained for both the bucket and drive wires

$$\begin{cases} \dfrac{dT_{b,w}}{dt} = \dfrac{\rho_{b,w}\left(T_{b,w}\right)}{c_{b,w}\left(T_{b,w}\right)\varrho_{b,w}\left(T_{b,w}\right)A_{b,w,cs}^2} I_b^2(t) \\ \dfrac{dT_{d,w}}{dt} = \dfrac{\rho_{d,w}\left(T_{d,w}\right)}{c_{d,w}\left(T_{d,w}\right)\varrho_{d,w}\left(T_{d,w}\right)A_{d,w,cs}^2} I_d^2(t) \end{cases} \tag{8.11}$$

where the quantities $[\rho, c, \varrho] = f(T)$, as shown in Chapter 4, and A_{cs} specifies the cross-sectional area, πr^2.

It is possible to include the ODEs presented in eqs. (8.4, 8.5, 8.7, 8.11) in one system. It is inferred that in the eqs. (8.4, 8.7) the wire resistances R have to be explicitely expressed, namely

$$R(T) = \frac{\rho_w(T)\ell_w}{A_{w,cs}} = \frac{\rho_w(T)\ell_w}{\pi r_w^2} \tag{8.12}$$

Therefore

$$\begin{cases} \dfrac{dI_b}{dt} = -\dfrac{1}{L_b}\left(\dfrac{\rho_{b,w}\left(T_b\right)\ell_{b,w}}{A_{b,w,cs}} I_b + M(x)\dfrac{dI_d}{dt} + I_d(x)\dfrac{dM(x)}{dt}\right) \\ \dfrac{dV}{dt} = \dfrac{1}{m}\dfrac{dM}{dx} I_d(x) I_b + 1.625\sin\delta \\ \dfrac{dT_{b,w}}{dt} = \dfrac{\rho_{b,w}\left(T_b\right)}{c_{b,w}\left(T_b\right)\varrho_{b,w}\left(T_b\right)A_{b,w,cs}^2} I_b^2(t) \\ \dfrac{dT_{d,w}}{dt} = \dfrac{\rho_{d,w}(T)}{c_{d,w}\left(T_d\right)\varrho_{d,w}\left(T_d\right)A_{d,w,cs}^2} I_d^2(t) \\ \dfrac{dW_d}{dt} = \dfrac{\rho_{d,w}\left(T_d\right)\ell_{d,w}}{A_{d,w,cs}} I_d(t)^2 \end{cases} \tag{8.13}$$

Given the definition of $M(x)$ and $dM(x)$, it may be convenient to convert the system in eq. (8.13) into a space-derivative one by the following transformation

$$\frac{\mathcal{X}(x)}{dt} = \frac{\mathcal{X}}{dx}\frac{dx}{dt} = \frac{\mathcal{X}}{dx}V(x) \tag{8.14}$$

At the same time, an additional ODE can be inserted to compute the time t, known that $V = \frac{dx}{dt}$, hence

$$\frac{dt}{dx} = \frac{1}{V(x)} \tag{8.15}$$

Therefore

$$\begin{cases} \dfrac{dI_b}{dx} = -\dfrac{1}{L_b}\left(\dfrac{\rho_{b,w}(T_b)\,\ell_{b,w}}{A_{b,w,cs}}\dfrac{I_b}{V(x)} + M(x)\dfrac{dI_d}{dx} + I_d(x)\dfrac{dM(x)}{dx}\right) \\ \dfrac{dV}{dx} = \dfrac{1}{m}\dfrac{dM}{dx}I_d(x)\dfrac{I_b}{V(x)} + \dfrac{1.625\sin\delta}{V(x)} \\ \dfrac{dT_{b,w}}{dx} = \dfrac{\rho_{b,w}(T_b)}{c_{b,w}(T_b)\,\varrho_{b,w}(T_b)\,A_{b,w,cs}^2}\dfrac{I_b^2(x)}{V(x)} \\ \dfrac{dT_{d,w}}{dx} = \dfrac{\rho_{d,w}(T_d)}{c_{d,w}(T_d)\,\varrho_{d,w}(T_d)\,A_{d,w,cs}^2}\dfrac{I_d^2(x)}{V(x)} \\ \dfrac{dW_d}{dx} = \dfrac{\rho_{d,w}(T_d)\,\ell_{d,w}}{A_{d,w,cs}}\dfrac{I_d^2(x)}{V(x)} \\ \dfrac{dt}{dx} = \dfrac{1}{V(x)} \end{cases} \tag{8.16}$$

Let $\{I_b, V, T_{b,w}, T_{d,w}, W_d, t\} = \{y_1, y_2, y_3, y_4, y_5, y_6\}$. The system can be rewritten as

$$\begin{cases} y_1' = -\dfrac{1}{L_b}\left(\dfrac{\rho_{b,w}(y_3)\,\ell_{b,w}}{A_{b,w,cs}}\dfrac{y_1}{y_2} + M(x)\dfrac{dI_d}{dx} + I_d(x)\dfrac{dM}{dx}\right) \\ y_2' = \dfrac{1}{m}\dfrac{dM}{dx}I_d(x)\dfrac{y_1}{y_2} + \dfrac{1.625\sin\delta}{y_2} \\ y_3' = \dfrac{\rho_{b,w}(y_3)}{c_{b,w}(y_3)\,\varrho_{b,w}(y_3)\,A_{b,w,cs}^2}\dfrac{y_1^2}{y_2} \\ y_4' = \dfrac{\rho_{d,w}(y_4)}{c_{d,w}(y_4)\,\varrho_{d,w}(y_4)\,A_{d,w,cs}^2}\dfrac{I_d^2(x)}{y_2} \\ y_5' = \dfrac{\rho_{d,w}(y_4)\,\ell_{d,w}}{A_{d,w,cs}}\dfrac{I_d^2(x)}{y_2} \\ y_6' = \dfrac{1}{y_2} \end{cases} \tag{8.17}$$

The advantage of using the variable in space instead of time allows to to evaluate $I_d(x)$ as sinusoidal over space, avoiding the difficulty of writing the function for the chirp signal analyzed in the Paragraph 2.6.3.

The system in eq. (8.17) is eventually rewritten as follows

$$\begin{pmatrix} \dfrac{dI_b}{dx} \\ \dfrac{dV}{dx} \\ \dfrac{dT_{b,w}}{dx} \\ \dfrac{dT_{d,w}}{dx} \\ \dfrac{dW_d}{dx} \\ \dfrac{dt}{dx} \end{pmatrix} = \begin{pmatrix} y_1' \\ y_2' \\ y_3' \\ y_4' \\ y_5' \\ y_6' \end{pmatrix} = \begin{pmatrix} f_1(x, y_1, y_2, y_3) \\ f_2(x, y_1, y_2) \\ f_3(y_3) \\ f_4(x, y_4) \\ f_5(x, y_2, y_4) \\ f_6(y_2) \end{pmatrix} = \begin{pmatrix} -\dfrac{1}{L_b}\left(\dfrac{\rho_{b,w}(y_3)\,\ell_{b,w}}{A_{b,w,cs}}\dfrac{y_1}{y_2} + M(x)\dfrac{dI_d}{dx} + I_d(x)\dfrac{dM}{dx}\right) \\ \dfrac{1}{m}\dfrac{dM}{dx}I_d(x)\dfrac{y_1}{y_2} + \dfrac{1.625\sin\delta}{y_2} \\ \dfrac{\rho_{b,w}(y_3)}{c_{b,w}(y_3)\,\varrho_{b,w}(y_3)\,A_{b,w,cs}^2}\dfrac{y_1^2}{y_2} \\ \dfrac{\rho_{d,w}(y_4)}{c_{d,w}(y_4)\,\varrho_{d,w}(y_4)\,A_{d,w,cs}^2}\dfrac{I_d^2(x)}{y_1} \\ \dfrac{\rho_{d,w}(y_4)\,\ell_{d,w}}{A_{d,w,cs}}\dfrac{I_d^2(x)}{y_2} \\ \dfrac{1}{y_2} \end{pmatrix} \tag{8.18}$$

This ODE system is the iterative core of optimization which must be accompanied by appropriate boundary conditions, NL constraints and MFs, in order to constrain the solution to physically feasible and desired results.

8.1.1 Constraints

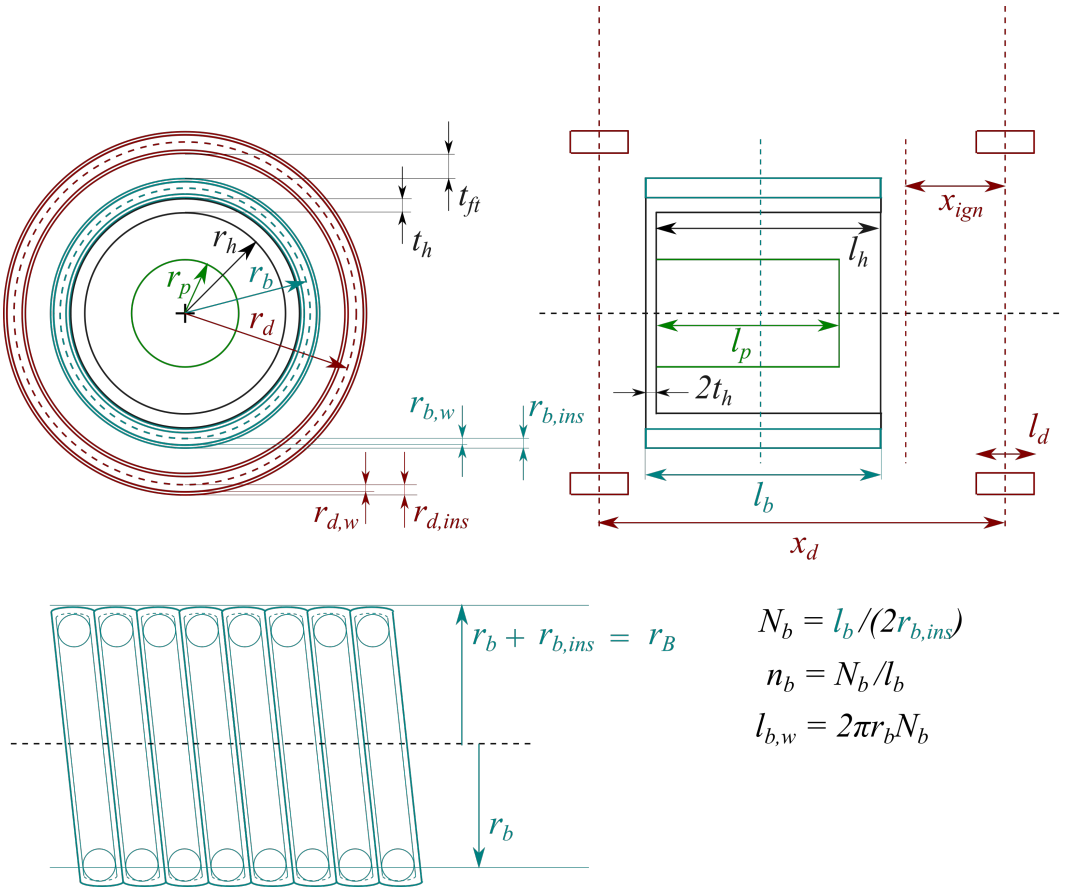

Figure 8.1: Mass driver configuration

In Fig. 8.1 is represented the mass driver configuration. There are 21 variables expressed in the column vector $\mathcal{x}$

$$\mathcal{x} = \left\{m_p, r_p, l_p, r_h, l_h, t_h, r_b, r_{b,i}, l_b, t_{ft}, r_d, r_{d,i}, l_d, n_b, n_d, r_{b,w}, r_{d,w}, x_d, x_{ign}, I_{bm}, I_{dm}\right\}^T \quad (8.19)$$

The convergence of a system of such large size and independent variables is difficult, with the addition of the fact that the computational cost could prove to be excessive. Furthermore, the problem will likely be not convex, and unless using a coarse global optimization to find feasible initial guess values, the solution would probably fall into various local minima.

It is possible to reduce the number of variables, in eq. (8.19), by imposing some parameters *a priori*, thus eliminating them from the optimization iterations. Surely two geometric parameters can be treated in this way, namely

$$\begin{aligned} t_h\,[\mathrm{m}] &= \frac{\max\left(m_p\right)\ \cdot 10^{-3}}{1+\exp\left[-\frac{m_p - 0.5\max\left(m_p\right)}{0.1\max\left(m_p\right)}\right]} \\ t_{ft}\,[\mathrm{m}] &= 5\ \cdot 10^{-3} \end{aligned} \quad (8.20)$$

Initially it was decided to use an S-curve –Sigmoid curve, or logistic function– for t_h to adapt the mass driver characteristics according to the payload mass. This choice proved to be only computationally more burdensome, and therefore the empirical formulation in eq. (8.21) was derived from the mean values of the iterations.

$$\begin{aligned} t_h\,[\mathrm{m}] &= 1\ \cdot 10^{-3} + 5 m_p\ \cdot 10^{-5} \\ t_{ft}\,[\mathrm{m}] &= 5\ \cdot 10^{-3} \end{aligned} \tag{8.21}$$

Lower mass implies a thinner bucket and, even though the value $\max(t_h)$ should be derived from structural considerations –as shown in Chapter 3–, since the acting forces are an output of the set of ODEs, a trial and error approach is implemented.

Furthermore, following the considerations made for the insulating radius in Paragraph 4.5.1, it is stated in first approximation that for any wire radius

$$r_i = 1.1 r_w \qquad \Longleftrightarrow \qquad k_i = 1.1 \tag{8.22}$$

This strong hypothesis will be refined in subsequent calculations.

Optimizing the value of m_p, r_b, l_b, together with eq. (8.21), allows to eliminate from the set of variables in eq. (8.19) the cavity dimensions, namely r_h and l_h, as linearly dependent. In other words, for the bucket volume computation, reference will be made only to the optimised values in such a way that the following expression is valid

$$\mathcal{V}_b = \pi \left\{ \left(r_b - 1.1 r_{b,w}\right)^2 l_b - \left[r_b - 1.1 r_{b,w} - t_h\left(m_p\right)\right]^2 \left[l_b - t_h\left(m_p\right)\right] \right\} \tag{8.23}$$

The verification of containment of the payload inside the bucket is done *a posteriori*. Indeed, the radius and the length of the cylinder, r_p and l_p, which simulates the payload, are variables and are actually independent of the whole problem. What really matters is that it is contained in the bucket cavity: a volume check would suffice

$$\mathcal{V}_p = \frac{m_p}{\varrho_p} = \pi r_p^2 l_p \tag{8.24}$$

with r_p and l_p freely chosen. A better result would be to impose them realistically as a real tank, for example by imposing

$$2 r_p = l_p \tag{8.25}$$

Following the considerations in Chapters 4, 6, it can be stated a preliminary sizing of the wires. Given that the total launch time is –roughly and indicatively–

$$t_{launch} \geq 2 \frac{l_{MD}}{V_{bo}} \tag{8.26}$$

i.e. below a second with reference values of $l_{MD} = 500\,\mathrm{m}$, $V_{bo} = 2500\,\mathrm{m\,s^{-1}}$, it follows that the bucket and drive coil wires can be sized *a priori*, knowing the JE heating. At most, they may be modified one-off. Therefore

$$\begin{cases} r_{d,w}[m] = 1 \cdot 10^{-3} \\ r_{b,w}[m] = 5 \cdot 10^{-3} \end{cases} \tag{8.27}$$

The bucket wires are thicker because they undergo the JE for the entire acceleration –and also after the launch, if the current has not yet completely decayed–. Consequently, other two parameters are deleted from the set of equations in eq. (8.19).

As anticipated, a slight improvement may be achieved by imposing a greater wire radius for the first bunch of drive coils, with the same provided current, so that temperature considerations will not limit the other fast-passing-through drive coils. For example, a first guess imposed set of values could be

$$\begin{cases} r_{d,w,1}[m] = 5 \cdot 10^{-3} \\ r_{d,w,2}[m] = 4 \cdot 10^{-3} \\ r_{d,w,3}[m] = 2.5 \cdot 10^{-3} \\ r_{d,w,4:n}[m] = 1 \cdot 10^{-3} \qquad n = N_{DC} \\ r_{b,w}[m] = 5 \cdot 10^{-3} \end{cases} \tag{8.28}$$

Moreover, if the bucket and drive lengths are optimization variables, and the wire thickness is fixed as in eq. (8.28), then the winding densities n_b and n_d can be deleted from the set of eqs. as linearly dependent on these.

To reduce the computational cost, it is possible to make some observation to effectively limit the variability of each component of eq. (8.19), or to make one variable linearly dependent on another. It is possible to state that

- Chapter 2, eq. (2.70), Fig. 2.16: M and $dM_{,x}$ increase with the ratio between the smaller and bigger coil, namely $\alpha = \frac{r_b}{r_d}$, therefore similar radii provide better electromagnetic mutual phenomena. Moreover, from Chapter 7, eq. (7.1), the force acting on the bucket and, thus, on the payload, is directly proportional to the $dM_{,x}$. This implies a strict equality between r_b and r_d, and therefore only one among the two should be used in the optimization, and the one chosen is r_b to comply with eq. (8.23) and, indeed, also with the considerations made in Paragraph 2.8.3;
- Chapter 4, eq. (4.35), Fig. 4.10: Copper does not melt with high currents over a single second. The drive coils have forced current and their impulse, even for the first couple of drives, lasts much less than a second. Therefore, the drive coil wire thickness does not need to be optimised and can be imposed *a priori*;

Finally, it is necessary to consider how M and $dM_{,x}$ are defined and how a NL optimizer works, in this case `fmincon`. The functions contained within it must be continuous and derivable in the domain, but both the previous are defined only in the ignition interval of the drive coil. For this reason, it might be appropriate to discretize the problem in the domain of a single drive coil, therefore within $\left[D_{d,i} - x_{ign}, D_{d,i} + x_{ign}\right]$, and then integrate

in the subsequent domain $\left[D_{d,i+1} - x_{ign}, D_{d,i+1} + x_{ign}\right]$ taking as initial values the final ones of the previous. In doing so, it is not necessary to know the distance between the drive coils, since the optimized condition –which also guarantees magnetic levitation– is to always have a current in the drive coils that accelerates buckets and payload. Therefore, also x_d can be deleted.

To generalize, the number of drive coils N_{DC} can be added to the system prior the computation. In addition, an integer parameter referred to the number of radial wire layers may be added for both the bucket and the drive coil(s), respectively n_{lb} and n_{ld}. Nevertheless, the number of layers can be defined also *a priori*; from the considerations made in Chapter 2, Paragraph 2.8.3, it can be deduced that the greater the number of layers, the more benefits to some electromagnetic parameters. Therefore, with the same considerations, after some iterations it was found the best efficiency with the following

$$\begin{cases} n_{lb} = 20 \\ n_{ld} = 3 \end{cases} \tag{8.29}$$

which leads to eliminate these parameters from the set of variables.

It is also important to consider the cable weight, especially for the bucket. In fact, the bucket mass to be accelerated is not simply the payload m_p, but to this must be added the container mass m_b, supposed in fiberglass laminate with $\varrho_b = 1800\,\mathrm{kg\,m^{-3}}$ (Laminated Plastics 2018), and the mass of the cable around the bucket, m_w. The following relationships can be used

$$\begin{aligned} m_w &= \mathcal{V}_w \varrho_w = \ell_w A_w \varrho_w \\ A_w &= \pi r_{b,w}^2 \\ \ell_w &= 2\pi l_b \sum_{i=0}^{n_{lb}} \left[r_b + k_i r_{b,w} \left(n_{lb} + 1 - 2i \right) \right] \end{aligned} \tag{8.30}$$

It follows that the effective number of variables is at least 8, and the system in eq. (8.19) becomes

$$\chi = \left\{ r_b, l_b, I_{b0}, l_d, x_{ign}, I_{dm}, r_{bw}, r_{dw,i} \right\}^T \tag{8.31}$$

Therefore $\chi \in \mathbb{R}^{\tilde{n}}$, where $\tilde{n} = n + N_{DC}$, where $n = 7$ are the variables for a single bucket-drive configuration and each set of new N_{DC} variables $r_{dw,i}$ are for each additional drive coil. Whether or not each drive coil is independent or not among each other, except for the wire radius size, arises from a first optimization.

Therefore, following these considerations, all constraints are presented.

$$\begin{aligned}
\left(r_b + 1.1r_{b,w} + t_{ft} - r_d + 1.1rd_w\right)_i &\le 0 \\
1 - 2 \cdot 1.1r_{b,w}n_b &= 0 \\
\left(1 - 2 \cdot 1.1r_{d,w}n_d\right)_i &= 0 \\
l_b - 2x_{ign,i} &\le 0 \\
\frac{m_p}{\varrho_p} - \pi\left\{\left(r_b - 1.1r_{b,w}n_{lb}\right)^2 l_b - \left[r_b - 1.1r_{b,w}n_{lb} - t_h\left(m_p\right)\right]^2\left[l_b - 2t_h\left(m_p\right)\right]\right\} &= 0
\end{aligned} \tag{8.32}$$

Where $i = 1, N_{DC}$, and all the pedices $_p$ refer to the payload, $_b$ to the bucket, $_d$ to the drive coils, and $_{,w}$ to the coil wires. The r are radii, l lengths, and n winding densities. The x_{ign} parameter refers to the drive coil ignition distance from its center for the current pulse. Finally, I_{bm} and I_{dm} refer to the current amplitude in the bucket and drive coils.

From this definition, the system of equations in eq. (8.32) can be rewritten in different form, separating the linear equations from the NL ones.

$$\begin{aligned}
\left(r_b + 1.1r_{b,w} + t_{ft} - r_d + 1.1rd_w\right)_i &\le 0 \\
l_b - 2x_{ign,i} &\le 0
\end{aligned} \quad \text{L}$$

$$\begin{aligned}
1 - 2 \cdot 1.1r_{b,w}n_b &= 0 \\
\left(1 - 2 \cdot 1.1r_{d,w}n_d\right)_i &= 0 \\
\frac{m_p}{\varrho_p} - \pi\left\{\left(r_b - 1.1r_{b,w}\right)^2 l_b - \left[r_b - 1.1r_{b,w} - t_h\left(m_p\right)\right]^2\left[l_b - t_h\left(m_p\right)\right]\right\} &= 0
\end{aligned} \quad \text{NL} \tag{8.33}$$

The eq. (8.33) can be expressed in matrix form. The linear disequalities $A\chi \le b$ are

$$\begin{cases}
r_b - r_d + 1.1r_{d,w} \le -5 \cdot 10^{-3} - 1.1r_{b,w} \\
l_b - 2x_{ign} \le 0
\end{cases} \tag{8.34}$$

$$\begin{matrix} r_b & l_b & I_{bm} & r_d & l_d & x_{ign} & I_{dm} & \overset{i}{\rightarrow} \end{matrix}$$
$$\begin{bmatrix} 1 & 0 & 0 & -1 & 0 & 0 & 0 & \dots \\ 0 & 1 & 0 & 0 & 0 & -2 & 0 & \dots \end{bmatrix}\{\chi\} \le \begin{Bmatrix} -5 \cdot 10^{-3} - 1.1r_{b,w} \\ 0 \end{Bmatrix} \tag{8.35}$$

2 rows and 4 columns are added to A in eq. (8.35) for each additional drive coil.

There are no linear equalities $A_{eq}\chi = b_{eq}$.

There are no nonlinear disequalities $c(\chi) \le 0$.

All the nonlinear equations in eq. (8.33) are nonlinear equalities $c_{eq}(\chi) = 0$.

8.1.2 Optimization logic

The entire ODE system presented in the previous Paragraphs allows to optimize geometric and electromagnetic parameters in order to obtain the minimum possible energy needed to feed the drive coils and make the launch of a certain payload for a certain mission feasible. This scenario implies the necessity to optimize two parameters, the final velocity –above a certain minimum value, eq. (6.3)– and the energy –the lowest possible for that final velocity–. However, the objective function of the optimization process can be only one. Therefore, the Matlab® possibility to embed a function in nested function is exploited to place a NL constraint to the velocity itself.

The optimization process is made up of two phases and the dimensions of the system to be solved, as well as the MF, change with each variation.

The first phase deals with the research of feasible geometries that fall within the limits imposed by linear and NL constraints. This phase has a raw discretization and usually converges in a short time: the set of variables of the system is simply 8, as if there was only a single drive coil, with the only difference to impose a scaling trend for the drive wire radii, as ideally done in eq. (8.28).

$$\chi = \left\{r_b, l_b, I_{b0}, l_d, x_{ign}, I_{dm}, r_{bw}, r_{dw}\right\}^T \in \mathbb{R}^8 \tag{8.36}$$

In particular, to simulate a complete integration along the length of the MD, each drive coil sees, in first approximation, its r_{dw} scaling according to the following equation

$$r_{dw,i} = \left(1 + \frac{1}{i}\right) r_{dw,i} \qquad\qquad i = 1 : N_{DC} \tag{8.37}$$

which allows to respect the thermal constraints without having singularities. In fact, the first coils will have thicker cables, which goes well with the longer pulse time which, in turn, produces a greater JE. With these hypotheses, the optimizer produces an estimate of the feasible geometry in order to obtain that given burnout speed using the Sequential-Quadratic-Programming (SQP) algorithm.

When this first phase is completed, the results, specifically the geometrical and electromagnetic values, are taken as initial guess of the second optimization phase. This foresees a change of the MF to be minimized, that is the energy, the fifth equation of the system in eq. (8.18). At the same time, the burnout speed becomes a NL constraint. The boundaries are immediately changed: in particular, the geometric optimization occurs in the neighborhood of the guess values produced in the first optimization, with the exception of the I_{b0} and $I_{dm,i}$ currents which act as upper limit values. In this optimization phase the system is bigger since it considers singularly each drive coil –and, therefore, computes the best radius for each of them–.

$$\chi = \left\{r_b, l_b, I_{b0}, l_d, x_{ign}, I_{dm}, r_{bw}, r_{dw,i}\right\}^T \in \mathbb{R}^{7+N_{DC}} \tag{8.38}$$

In the following Figure it is possible to appreciate a flowchart that describes the optimization logic.

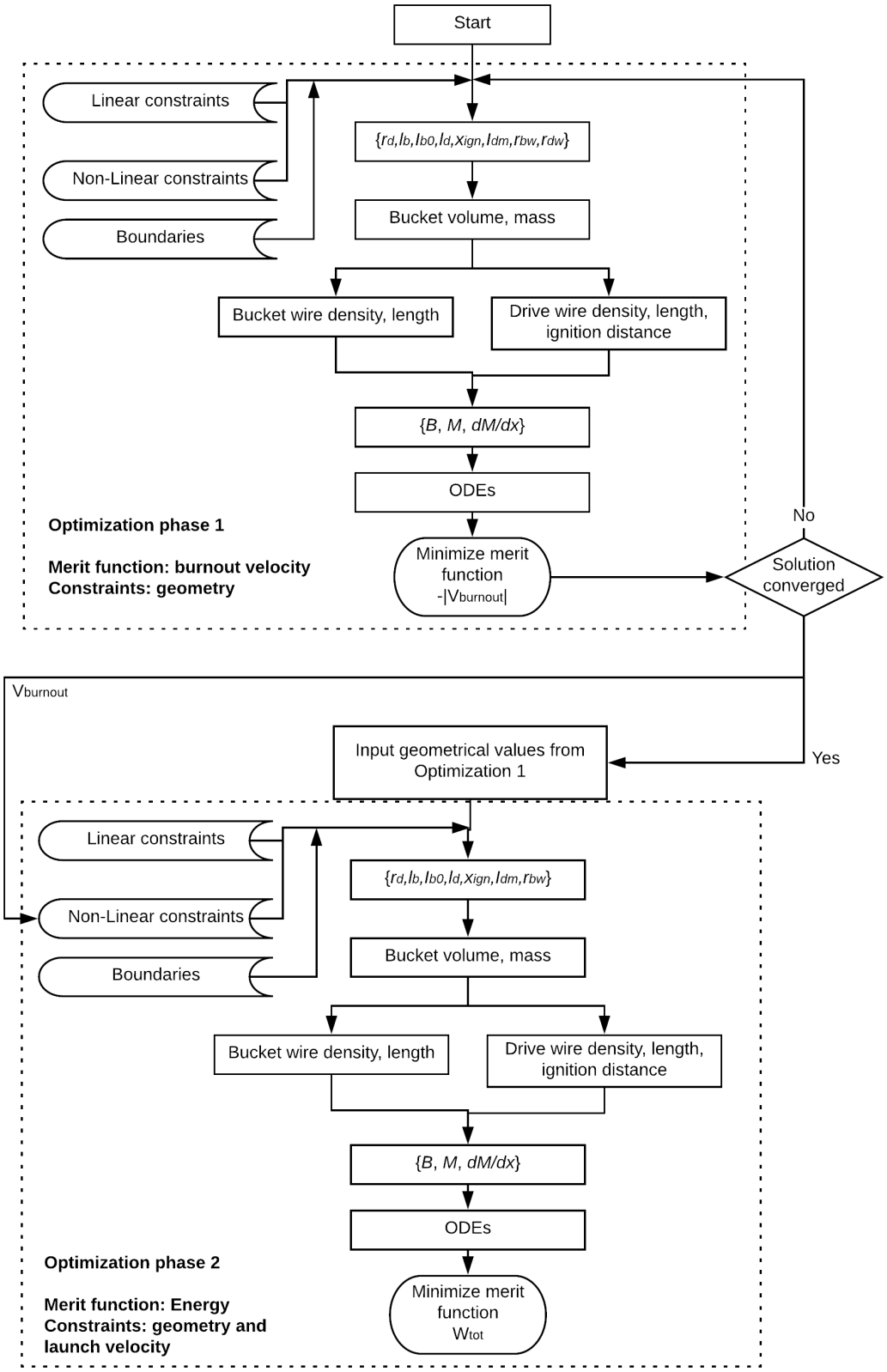

Figure 8.2: Optimization logic

8.1.3 A further consideration about thermal constraints

By combining electrothermal phenomena, specifically the eq. (2.27) in Chapter 2 and the eq. (4.4) in Chapter 4, it is possible to show what will be computed "behind" the optimizer.

$$c \cdot m\Delta T = R(T)I^2\Delta t \tag{8.39}$$

in which the specific heat of the cable is correlated with the thermal energy produced by JE. By writing the resistance with eq. (2.28) and rearranging the rhs and lhs

$$\begin{aligned} c \cdot \varrho_{mat}\ell A_{w,cs}\Delta T &= \left[1 + \alpha\left(T - T_{ref}\right)\right]\rho_{ref}\frac{\ell}{A_{w,cs}}I^2\Delta t \\ \frac{\Delta T}{\Delta t} &= \frac{\rho_{ref}I^2}{c \cdot \varrho_{mat}A_{w,cs}^2}\left[1 + \alpha\left(T - T_{ref}\right)\right] \\ \frac{dT}{dt} &= \frac{\rho_{ref}I^2}{c \cdot \varrho_{mat}A_{w,cs}^2}\left(1 + \alpha T(t) - \alpha T_{ref}\right) \\ \frac{dT}{dt} &= k\left(1 + \alpha T(t) - \alpha T_{ref}\right) \end{aligned} \tag{8.40}$$

where ϱ_{mat} is the material density while ρ_{ref} is the material resistivity at 20°C.
It is possible to express the terms within the parentesis in the rhs as a function of an auxiliary variable (Adam 2015) in such a way that

$$\vartheta = 1 + \alpha T - \alpha T_{ref} \implies T = \frac{\vartheta - 1 + \alpha T_{ref}}{\alpha} \tag{8.41}$$

and therefore

$$\frac{dT}{dt} = \frac{dT}{d\vartheta}\frac{d\vartheta}{dt} = \frac{1}{\alpha}\frac{d\vartheta}{dt} \tag{8.42}$$

by equating (8.40, 8.42) it is possible to solve the ODE.

$$\begin{aligned} \frac{d\vartheta}{dt} &= k\alpha\vartheta & &\implies \frac{d\vartheta}{\vartheta} = k\alpha dt \\ \int_1^{\vartheta}\frac{\mathrm{d}\vartheta}{\vartheta} &= \int_0^t k\alpha\ \mathrm{d}t & &\implies \ln\vartheta - \ln 1 = k\alpha t \implies \ln\vartheta = k\alpha t \end{aligned} \tag{8.43}$$

By substituting again ϑ in the lhs and k in the rhs

$$\ln\left(1 + \alpha T - \alpha T_{ref}\right) = \frac{\rho_{ref}I^2}{c \cdot \varrho_{mat}A^2}\alpha t \tag{8.44}$$

Equation (8.44) can be solved according to various parameters. If the temperature and time limit coincide with those of melting, T_{melt} and t_{melt}, knowing the physical parameters of the cable it can be traced back the melting current I_{melt}

$$I_{melt} = A\sqrt{\frac{c \cdot \varrho_{mat} \ln\left(1 + \alpha T - \alpha T_{ref}\right)}{\rho_{ref} \alpha t_{melt}}} \tag{8.45}$$

The (8.45) is used for a thermal analysis of cable fusion[1]. Taking as references cables made in aluminium, copper, and iron, in order to analyze their differences, an analysis should be made to understand to what extent may be influential to consider the temperature rise of the cables, at least from the point of view of the melting temperature and to understand if the short current pulses in the drive coils are sufficiently below the melting current.

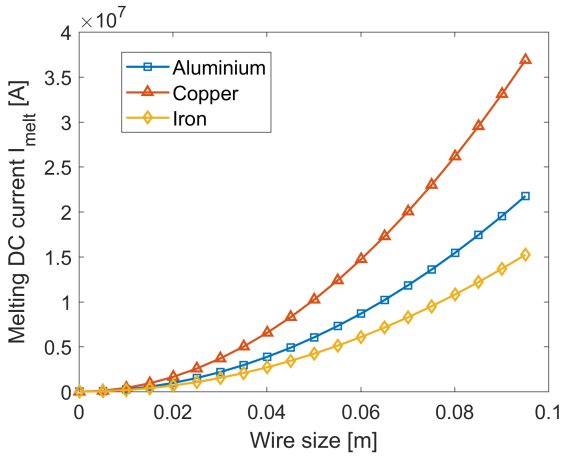

Figure 8.3: Melting current I_{melt}

In Fig. (8.3) it is possible to appreciate the trend of the melting current wrt the cable thickness. As reference temperature, it was chosen the Shackleton Crater PSR temperature, $T_{ref} = -183^{\circ}\,\mathrm{C}$ (Stoica et al. 2016; Sefton-Nash et al. 2017).

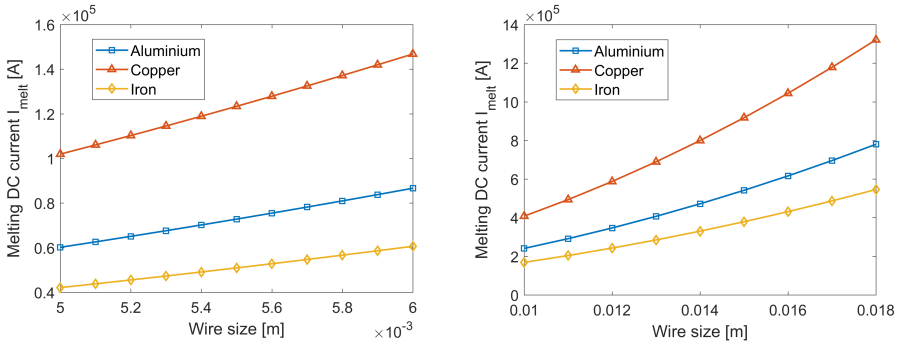

Figure 8.4: Melting current I_{melt} - smaller wires

Due to the copper melting temperature and its thermal properties at low temperatures (refer to Appendix A), the melting current is constantly higher wrt the other materials

[1]The validity of the formula is proven with the Stauffacher and Onderdonk study of short-time melting current for copper, (Stauffacher and Onderdonk 1928; Onderdonk 1944), in which all the variables in eq. (8.45) referred to a specific material are directly expressed by numbers and the units of measurement are related to the cmil. In this text, however, it is considered more appropriate to provide a general formulation and adopt the SI, specifying that the results for the copper differ less than half a percentage point wrt the cited formula.

and, for a pulse that last at most 5 centiseconds, higher than 10^5 A for wire radii of just 5 mm, as shown in Fig. 8.4. This current value increases in quadratic proportions by increasing the thickness of the cable.

It should be emphasized that the melting current is direct current (DC). Therefore, the use of an AC, as is actually done for the drive coils, would imply the use of the I_{eff} (2.49). Continuing to use $I_{d,m}$ in place of $I_{d,eff}$ implicitly imposes a safety factor of $\sqrt{2}$.

An important observation: on the one hand, the mutual inductance, and therefore its gradient, and in turn the force exerted on the bucket, increases with the winding density, which implies small wires, if the coil axial length is fixed; on the other hand, too small wires must have lower current to not melt, reducing the available force again.

Concluding, it can reasonably be stated that the melting current is not a problem for the the drive coils, as they are excited individually for short periods and with AC of about 10^5 A –imposed as upper limit–. As for the bucket, in which the decay of the current is given by the LR circuit, with the same considerations and with a conservative analysis, it must be imposed a conservative minimum radius, as done in eq. (8.27).

This brief observational paragraph also provides the information, once again, how in the scenario presented in this analysis the use of copper as a conductive material for cables is more convenient.

8.1.4 Energy needs

When the optimization process has completed the various iterations, it is possible to derive the energy needed to operate the MD. The simple ideal net energy $W = W_b + \sum W_d$ derived from the ODE system must be appropriately scaled by means of a series of electrical or energy efficiencies.

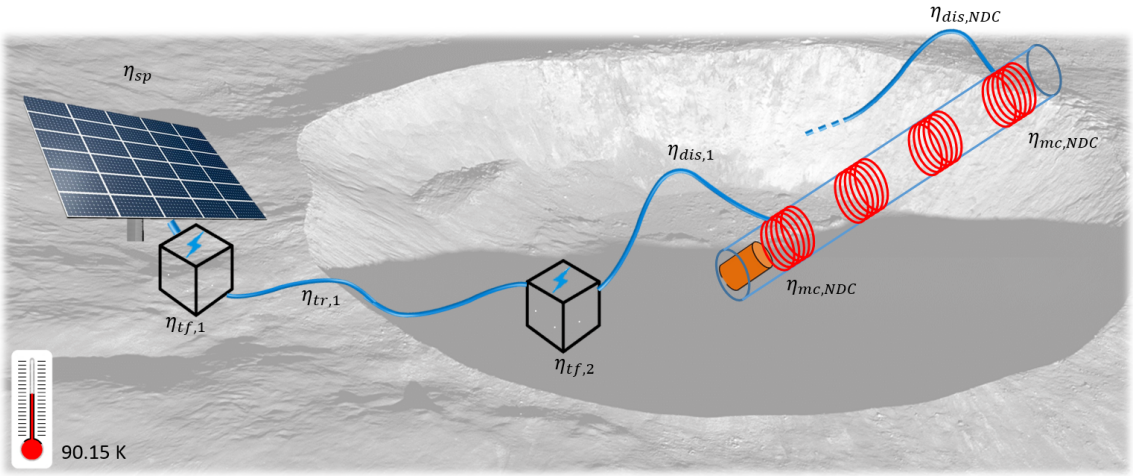

Figure 8.5: Efficiencies throughout the whole MD system

With reference to Fig. 8.5, starting from the solar panel system, it is noted that there is a transformer on the edge of the crater - which produces a high voltage in order to reduce line losses to the bottom–, a further transformer at the base of the crater, and a series of distribution lines in number equal to the number of drive coils. Each component has its energy efficiency, estimated or calculated in

$$\begin{cases} \eta_{sp} = 0.200 \\ \eta_{il} = 0.867 \\ \eta_{tr} = 0.900 \\ \eta_{tf} = 0.970 \\ \eta_{dis} = 0.980 \\ \eta_{mc} = \dfrac{1}{N_{DC}} \displaystyle\sum_{i=1}^{N_{DC}} \dfrac{M^2}{L_b L_{d,i}} \end{cases} \tag{8.46}$$

The solar panel efficiency, η_{sp} has a conservative value, compared to the current Technology Readiness Level (TRL). It may be pushed up to $\eta_{sp} \approx 0.250 \div 0.300$.

It is assumed a region with high solar illumination over a certain period of time to provide energy to the solar panels. Considering an illumination of 86.3% (Bryant 2009) towards the solar panel, the corresponding illumination efficiency η_{il} is deduced. It should be noted that it is not convenient to raise the solar panel height to increase the illumination because the gain in light/dark ratio does not justify the costs and the construction complexity (Haruyama et al. 2008).

To reduce transmission losses the power transmission from the crater rim to the bottom occurs with a very high-voltage line, thus defining a conservative transmission efficiency

η_{tr}. The transformer used for the electrical conversion has its own efficiency η_{tf} and has to be considered twice, one for the transformer on the crater rim and one on the base.

For the N_{DC} distribution lines it is supposed an equal efficiency for each line of η_{dis}.

The last efficiency, η_{mc}, is related to the magnetic coupling factor and it indicates how efficiently the magnetic fields interact among the coils. Since it changes during the launch, its mean value is taken as reference and it is computed at the end of every optimization.

In conclusion, the overall efficiency is

$$\eta = \eta_{sp} \cdot \eta_{il} \cdot \eta_{tf}^2 \cdot \eta_{tr} \cdot \eta_{mc} \cdot \sum_{i=1}^{N_{DC}} \eta_{dis,i} \tag{8.47}$$

8.2 Mass Driver Optimizer - MDO

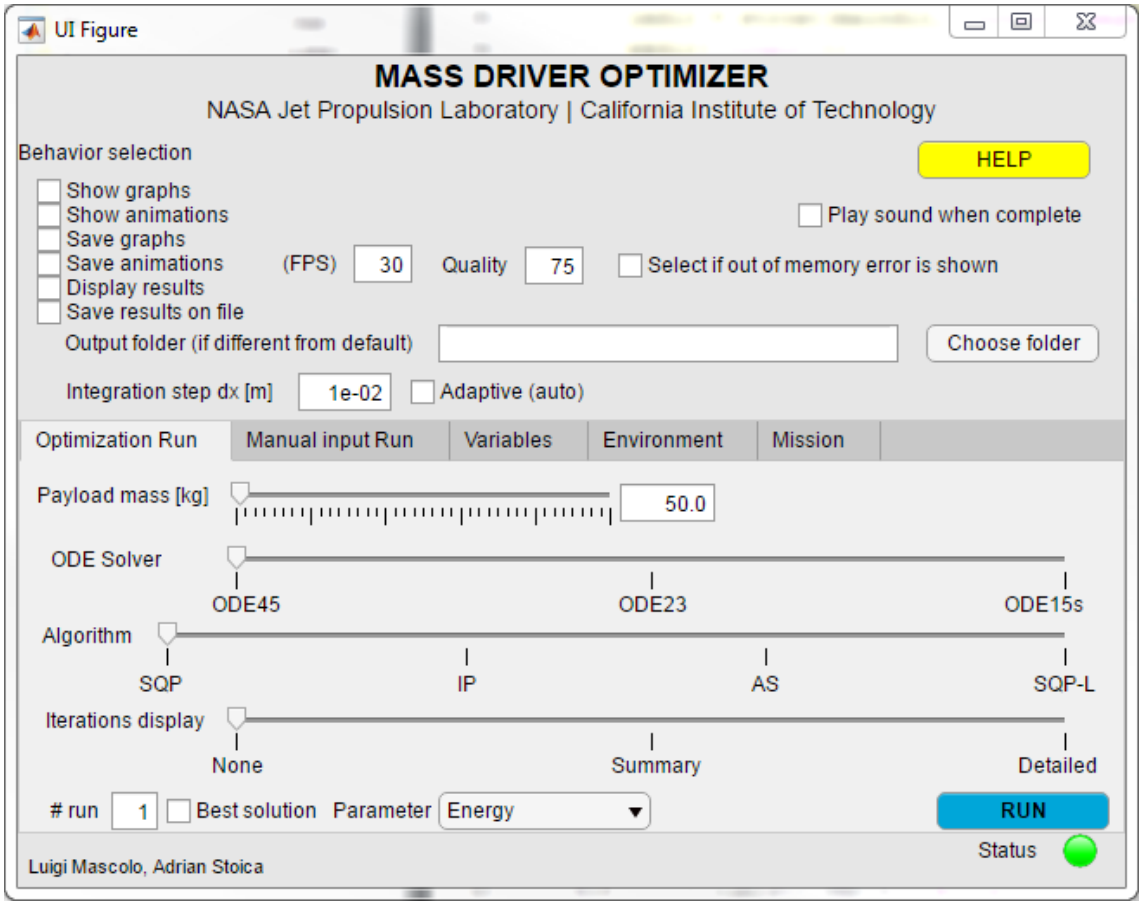

Figure 8.6: MDO GUI

The optimizer (Mass Driver Optimizer (MDO)®) has its own GUI for a wide input offer. It can re-analyze previous optimization to find, potentially, other possibly better local minima. MDO uses a gradient descent algorithm and, therefore, it searches for local minima. If the results are *good* local minima, or even –casually– a global minimum, is due to the fact that the same input array is executed more times the more the N_{DC} increases, and with random defects in order to avoid the same convergence.

It is also included a cue of a genetic algorithm: the more previous runs the software has, the more the database is filled with results that are cataloged, through the file name, with the most indicative parameters of a specific output (efficiencies, required energies, costs, etc. . .). If an actual iteration tends to approach values that have been categorized as inefficient, the algorithm tends to avoid that convergence, stopping that research and generating a new set of input data.

9. Results

The analysis presented in Chapter 8 includes a general guideline that clearly delineates the magnitude of the various parameters. Nevertheless, during the various optimizations it was noted that some parameters could be further refined: this "manual" optimization may have led to better results, but it is certainly worthy of an automated implementation in future studies.

Below there are the most significant results for three payloads of $m_p = \{5, 50, 500\}$ kg. Please note that m_u is the payload fraction, i.e. the mass of the payload m_p compared to the mass of the whole system (payload and bucket), namely

$$m_u = \frac{m_p}{m_p + m_b + m_w} \tag{9.1}$$

where m_b and m_w are, respectively, the bucket mass (eq. (8.24)) and the wire mass (eq. (8.30)).

	Payload mass		
	5	50	500
bucket			
n_{lb}	10	15	25
$l_b\,[\mathrm{m}]$	0.6216	2.1217	3.8601
$I_{b0}\,[\mathrm{A}]$	$9.7538 \cdot 10^3$	$8.9306 \cdot 10^3$	$7.3080 \cdot 10^3$
$r_b\,[\mathrm{m}]$	0.4083	0.8500	0.8825
$r_{bw}\,[\mathrm{m}]$	$1.112 \cdot 10^{-3}$	$2.120 \cdot 10^{-3}$	$2.237 \cdot 10^{-3}$
drive			
n_{ld}	3	3	3
$l_d\,[\mathrm{m}]$	0.9353	2.4935	4.0974
$I_{dm}\,[\mathrm{A}]$	$1.0000 \cdot 10^4$	$1.0000 \cdot 10^4$	$1.0000 \cdot 10^4$
$x_{ign}\,[\mathrm{m}]$	0.9617	2.7576	5.2765
goodness			
$\eta\,[\%]$	7.24	6.00	4.15
m_u	0.4449	0.3012	0.2970

Table 9.1: Geometrical and electrical results

	Drive coil wire radius r_{dw} [mm]		
	$i = 1, 4, 7, \ldots$	$i = 2, 5, 8, \ldots$	$i = 3, 6, 9, \ldots$
$m_p = 5$ [kg]	0.869	0.751	0.701
	0.667	0.644	0.625
	0.609	0.599	0.586
	0.577		
$m_p = 50$ [kg]	7.734	3.344	3.034
	1.631	1.543	1.419
	1.344	1.293	1.260
	1.260	1.224	1.192
	1.164	1.142	1.112
	1.110	1.086	1.078
	1.069	1.059	1.053
	1.046	1.041	1.035
	1.031		
$m_p = 500$ [kg]	1.500	1.250	1.180
	1.125	1.100	1.083
	1.093	1.063	1.056
	1.050	1.045	1.042
	1.038	1.036	1.033
	1.031	1.029	1.028
	1.026	1.025	1.024
	1.023	1.022	1.021
	1.020	1.019	1.019
	1.018	1.017	1.017
	1.016	1.016	1.015
	1.015	1.014	1.014
	1.014	1.014	1.013
	1.013	1.012	1.012
	1.012	1.012	1.011
	1.011	1.011	1.011
	1.010	1.010	

Table 9.2: Drive coils wire radii

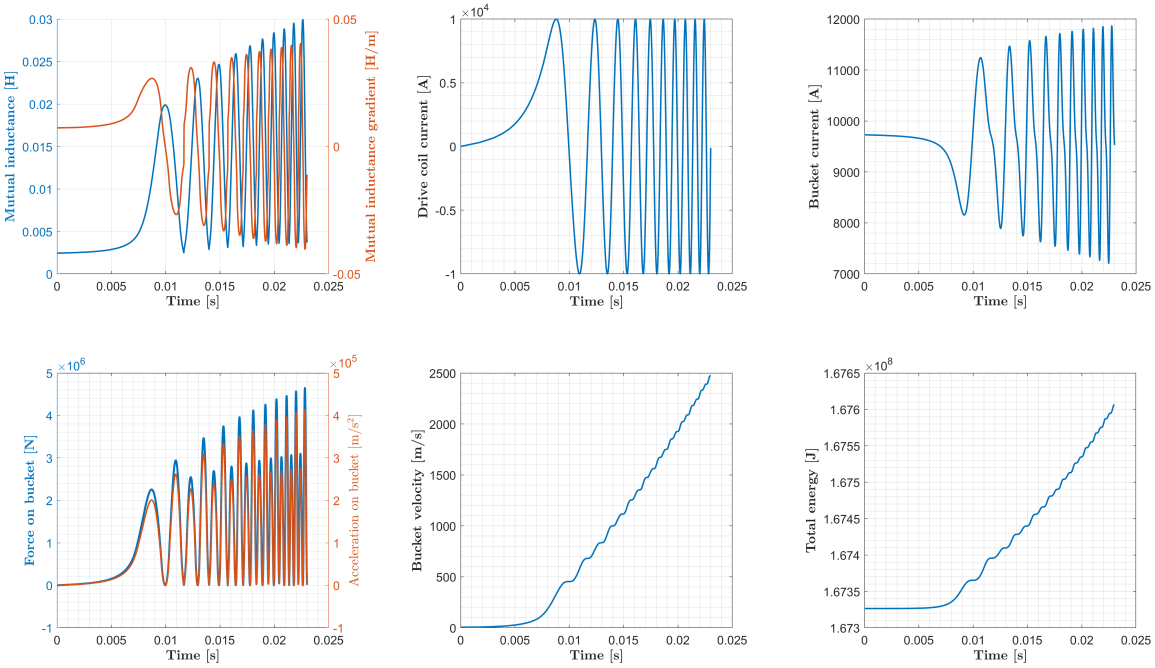

Figure 9.1: $m_p = 5\,[\text{kg}]$ - results 1 - overall trend

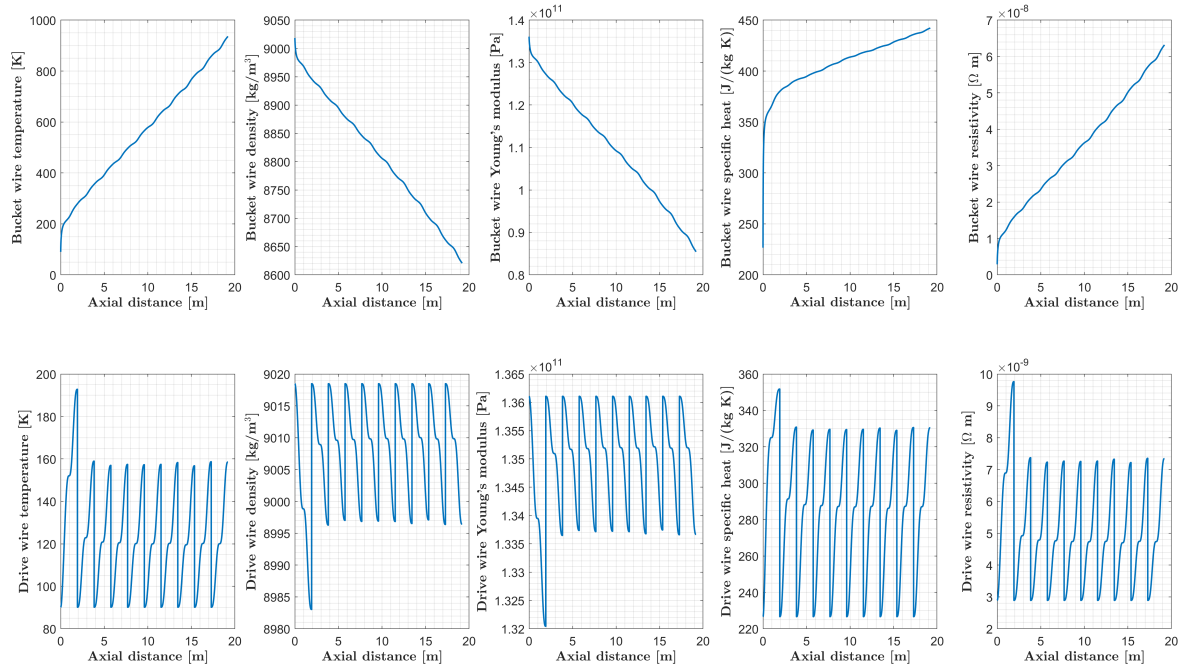

Figure 9.2: $m_p = 5\,[\text{kg}]$ - results 2 - material properties

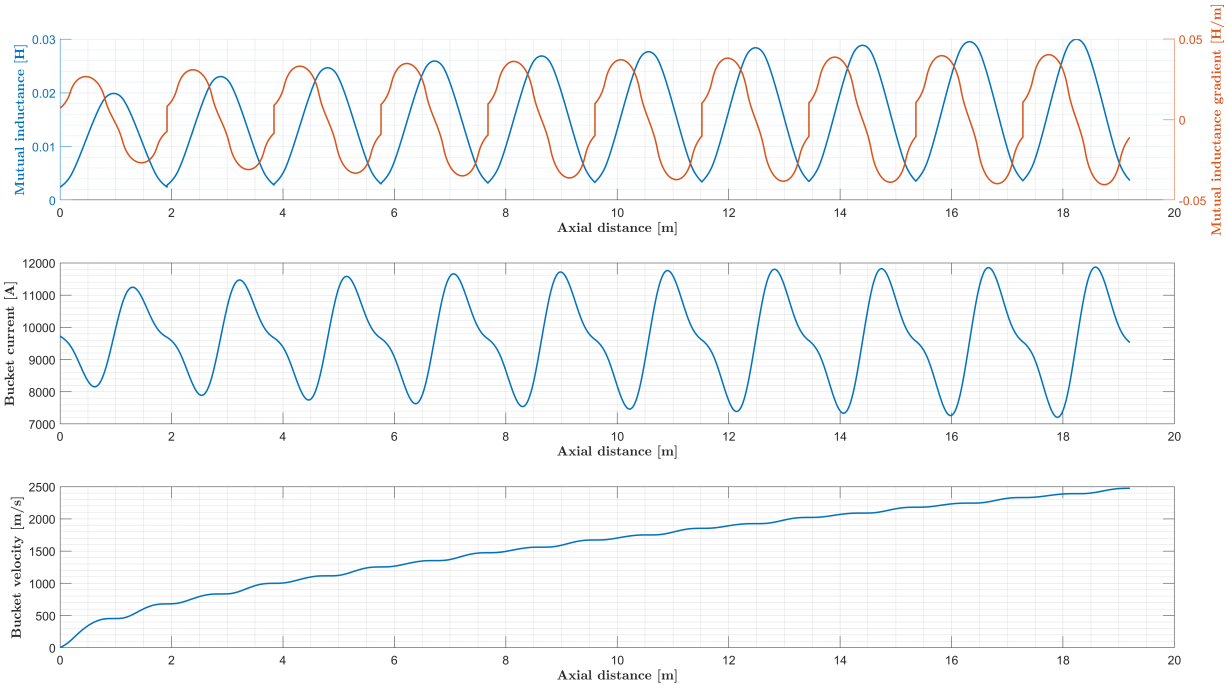

Figure 9.3: $m_p = 5\,[\text{kg}]$ - results 3 - electromagnetic details

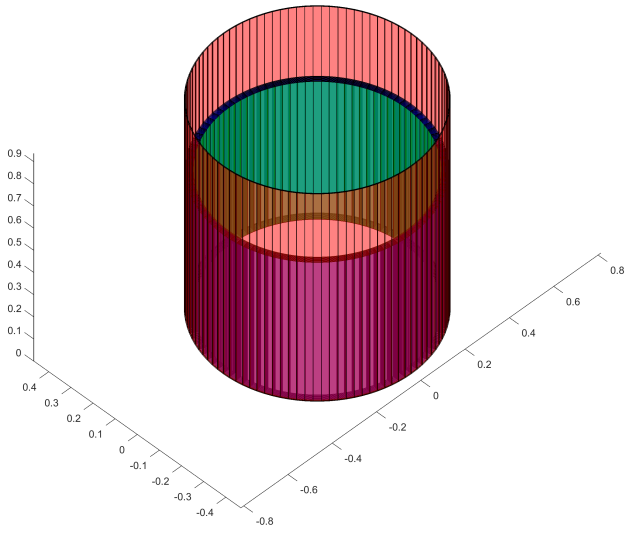

Figure 9.4: $m_p = 5\,[\text{kg}]$ - results 4 - payload/bucket coils/drive coils geometry

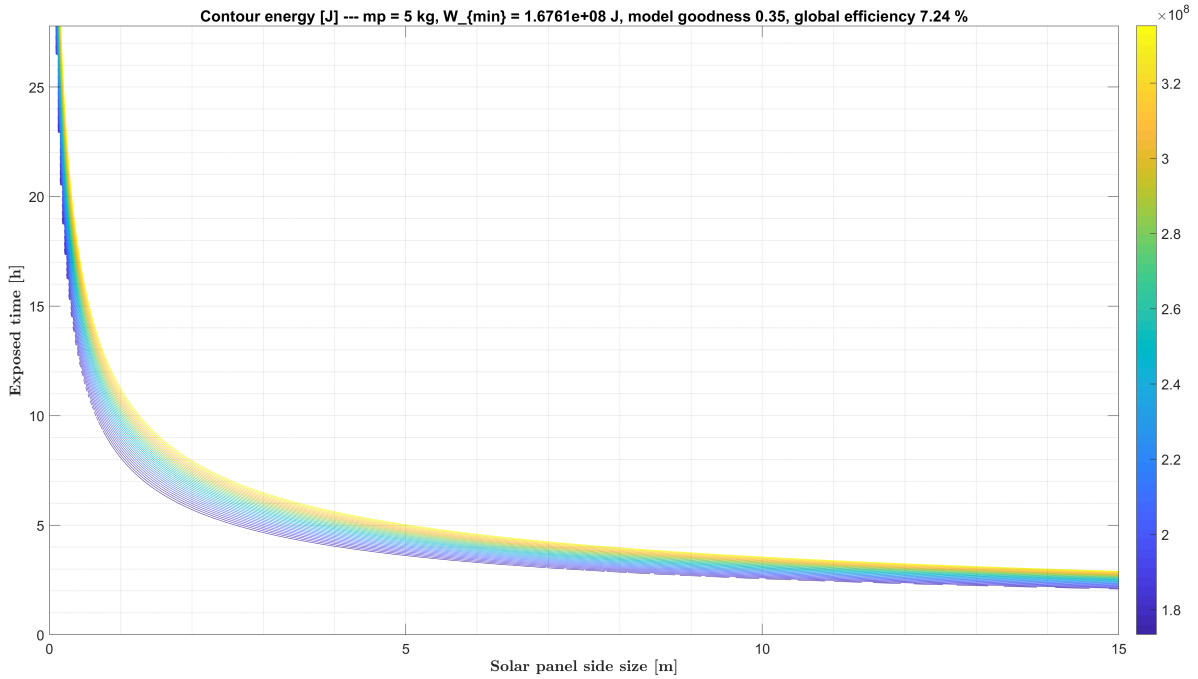

Figure 9.5: $m_p = 5\,[\text{kg}]$ - results 5 - energy contour 1

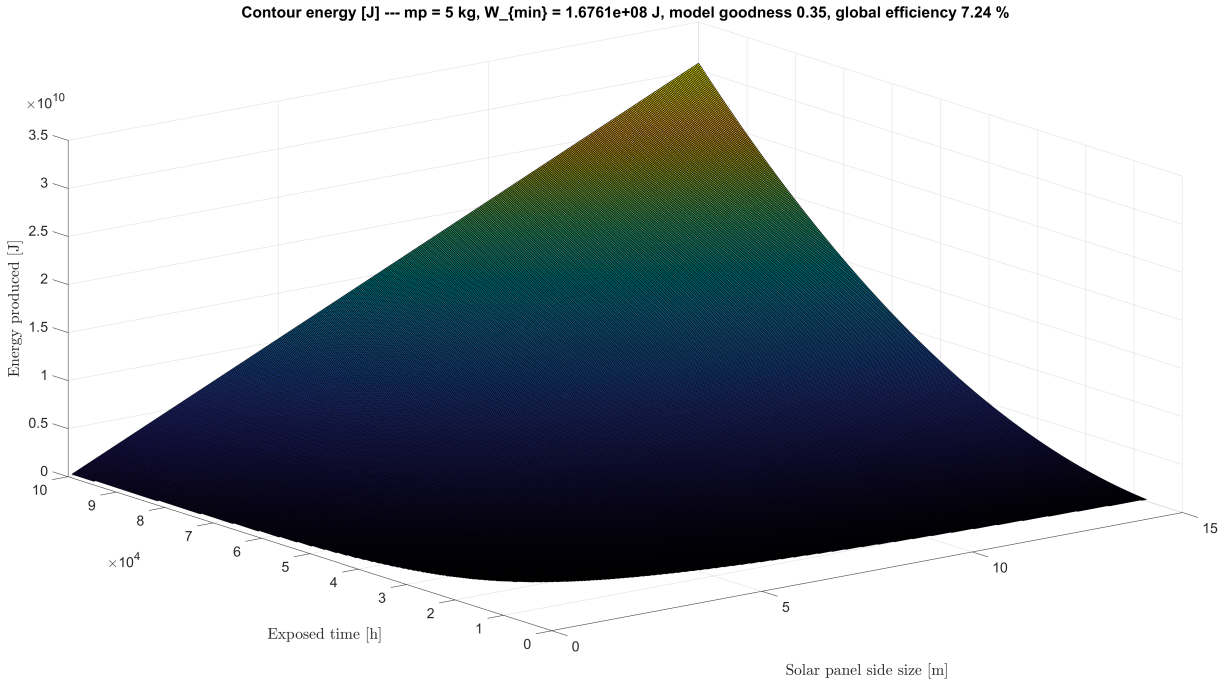

Figure 9.6: $m_p = 5\,[\text{kg}]$ - results 6 - energy contour 2

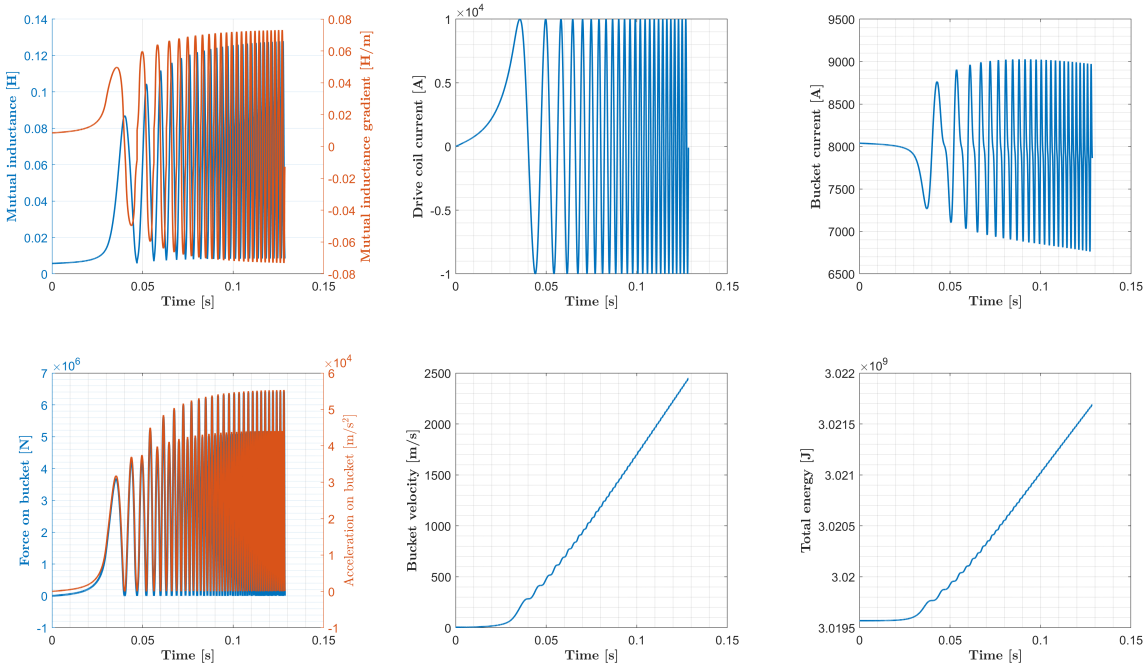

Figure 9.7: $m_p = 50\,[\text{kg}]$ - results 1 - overall trend

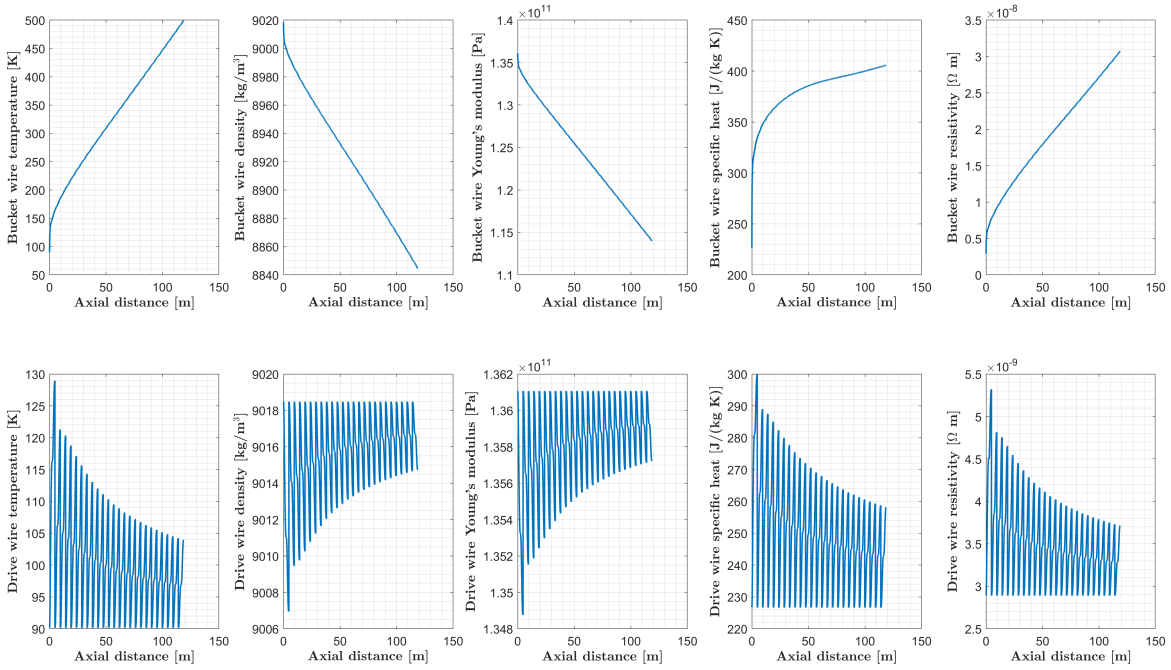

Figure 9.8: $m_p = 50\,[\text{kg}]$ - results 2 - material properties

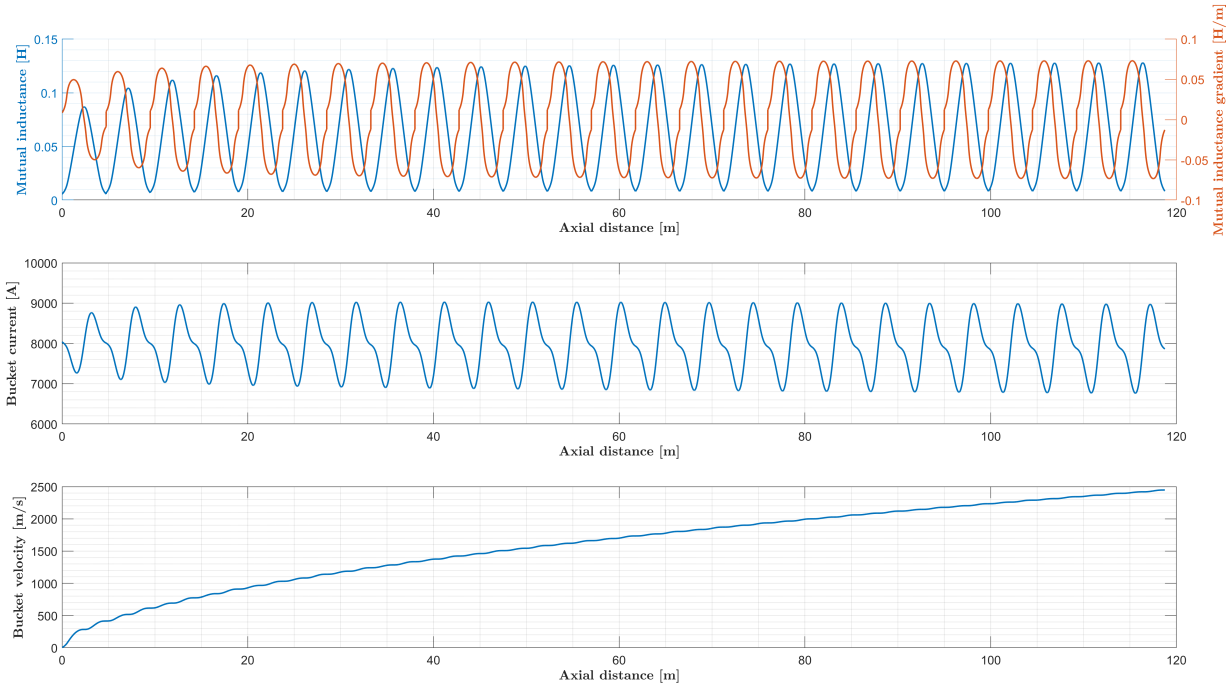

Figure 9.9: $m_p = 50\,[\text{kg}]$ - results 3 - electromagnetic details

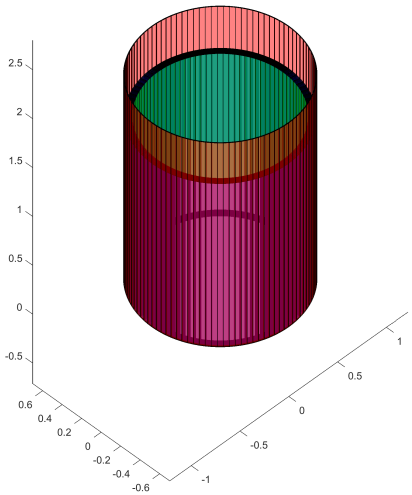

Figure 9.10: $m_p = 50\,[\text{kg}]$ - results 4 - payload/bucket coils/drive coils geometry

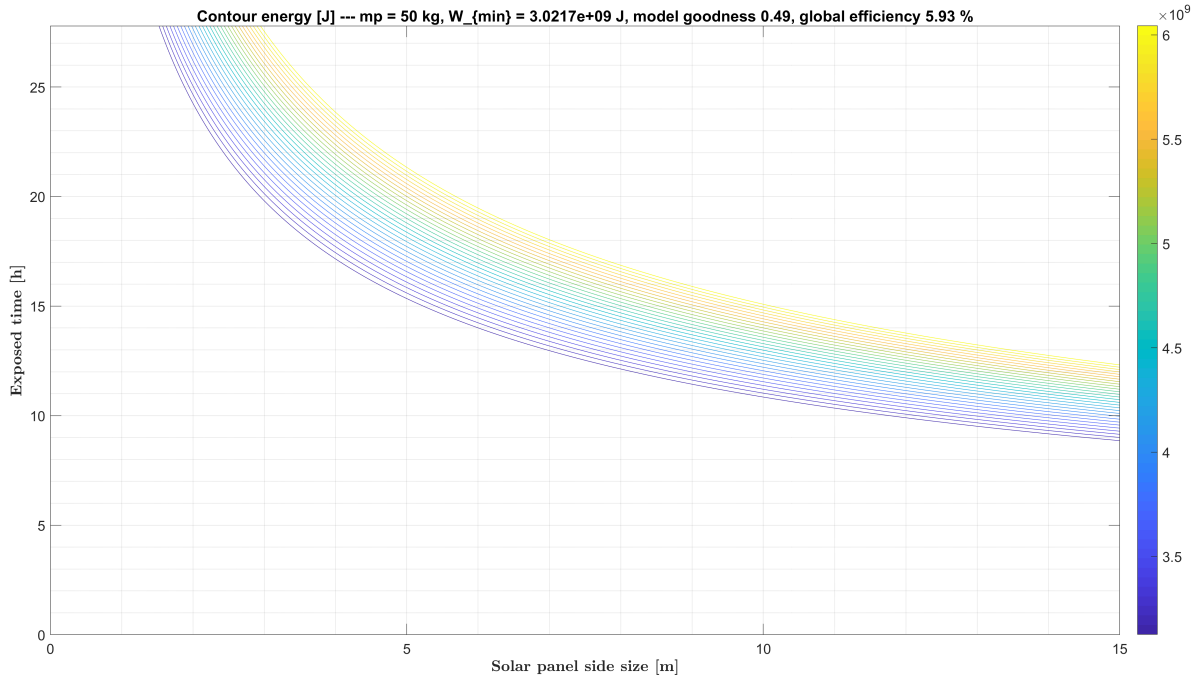

Figure 9.11: $m_p = 50\,[\text{kg}]$ - results 5 - energy contour 1

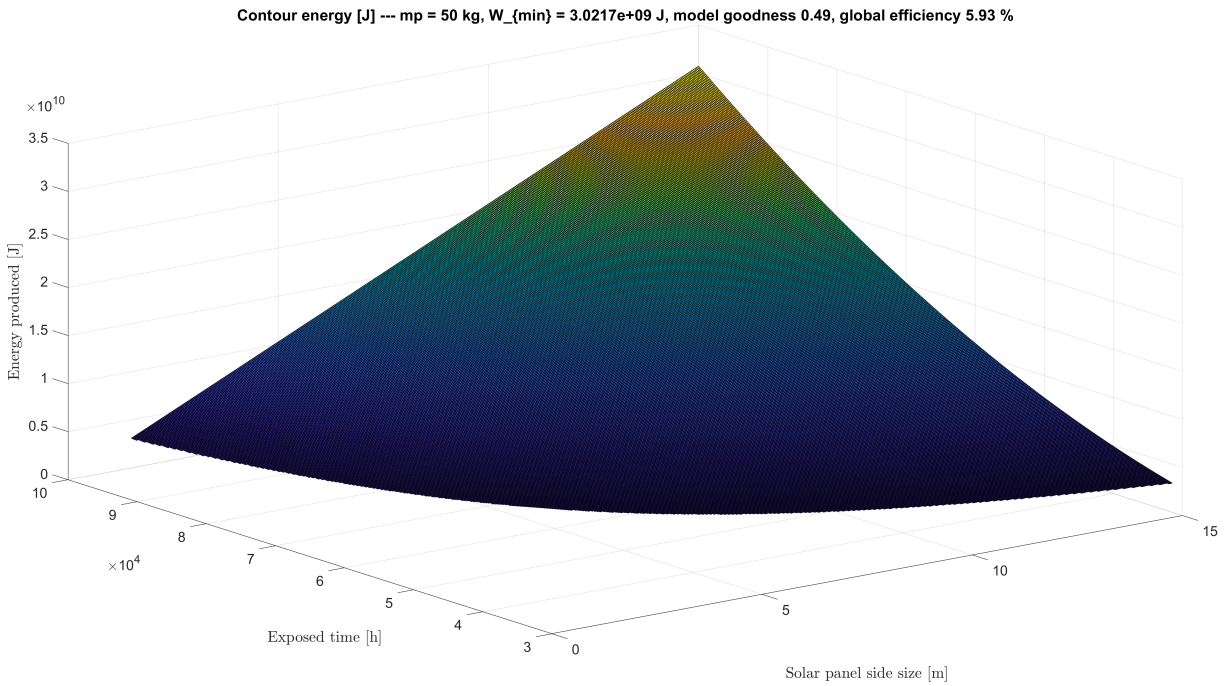

Figure 9.12: $m_p = 50\,[\text{kg}]$ - results 6 - energy contour 2

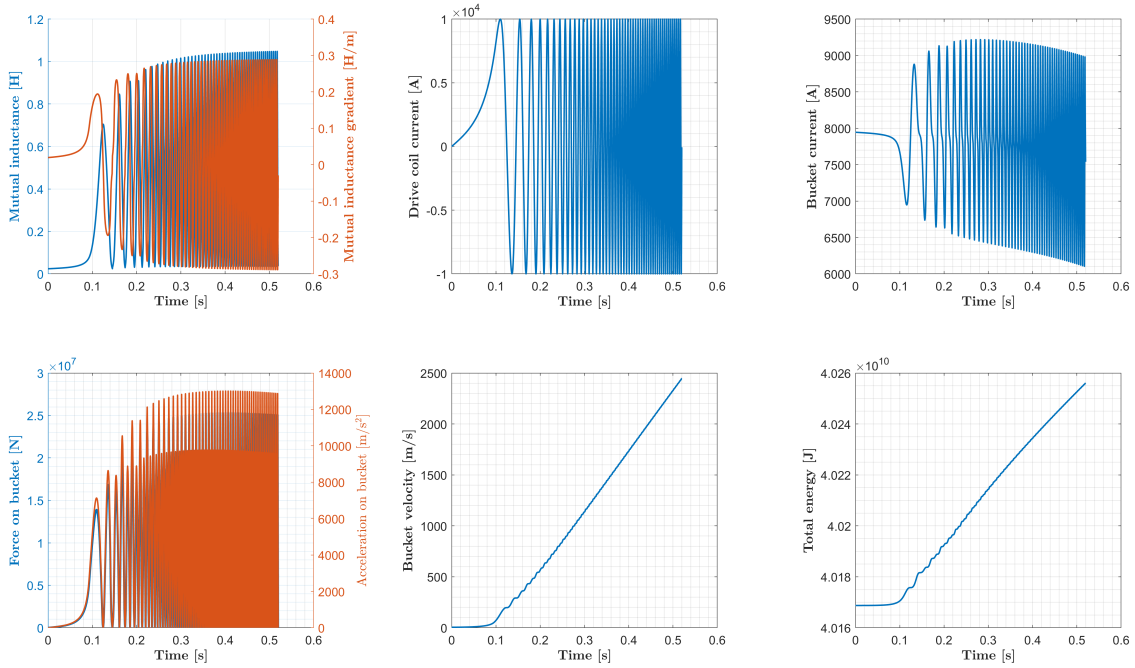

Figure 9.13: $m_p = 500\,[\mathrm{kg}]$ - results 1 - overall trend

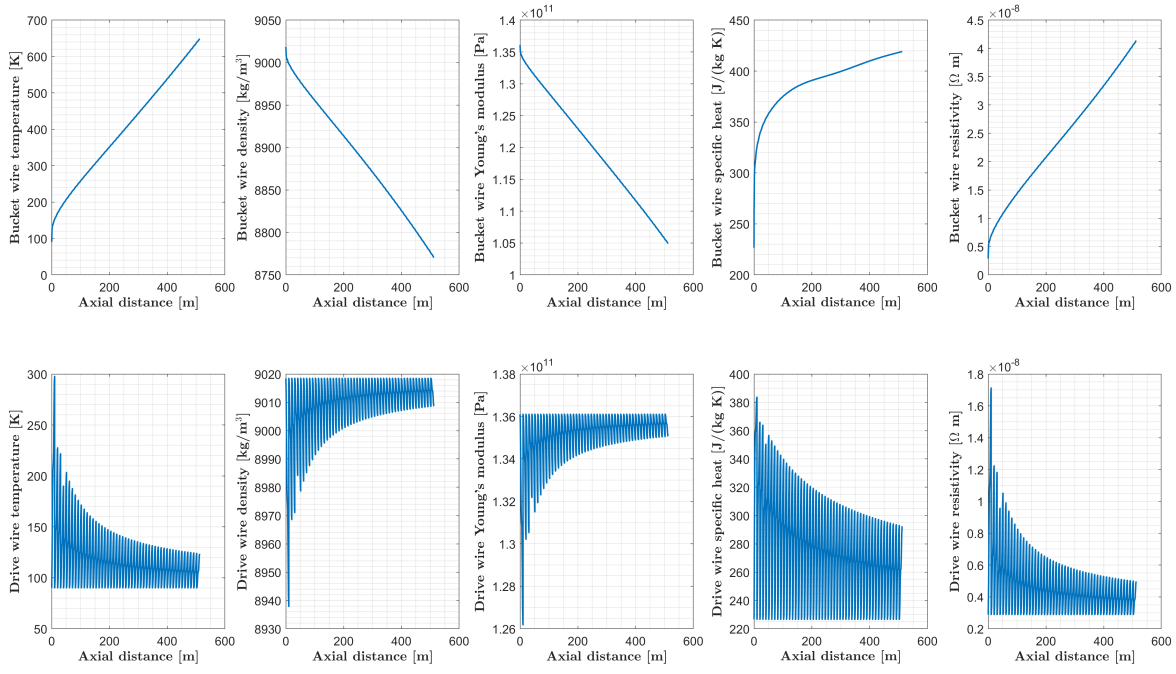

Figure 9.14: $m_p = 500\,[\mathrm{kg}]$ - results 2 - material properties

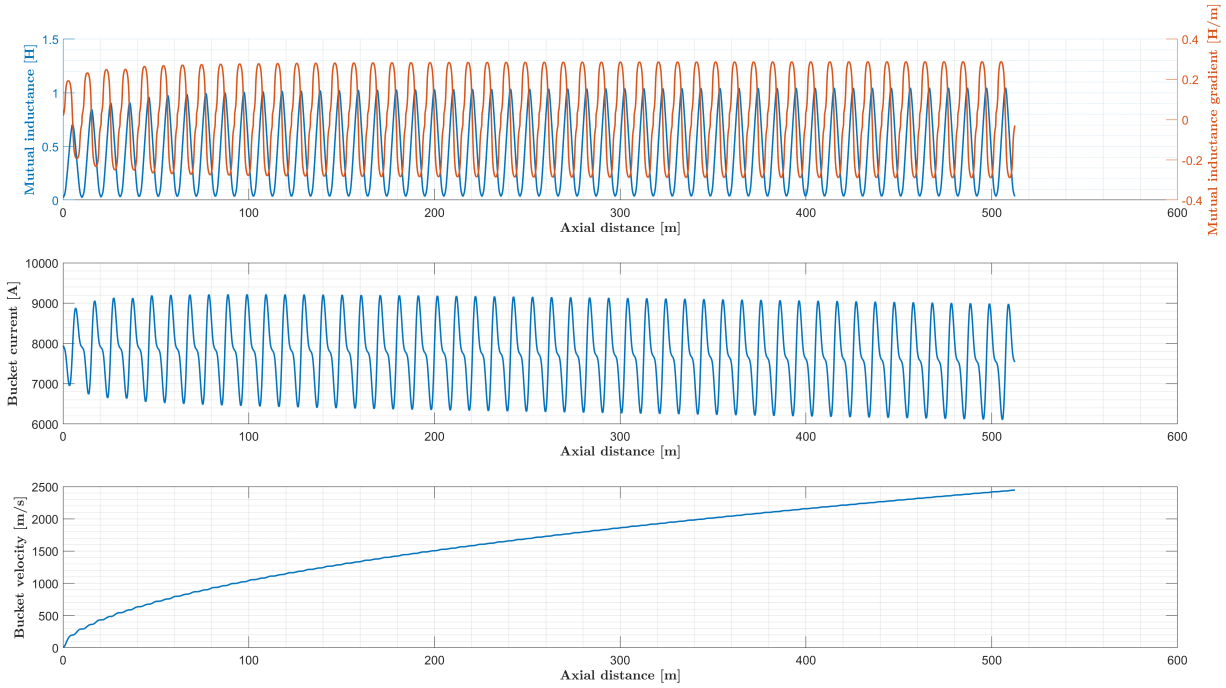

Figure 9.15: $m_p = 500\,[\text{kg}]$ - results 3 - electromagnetic details

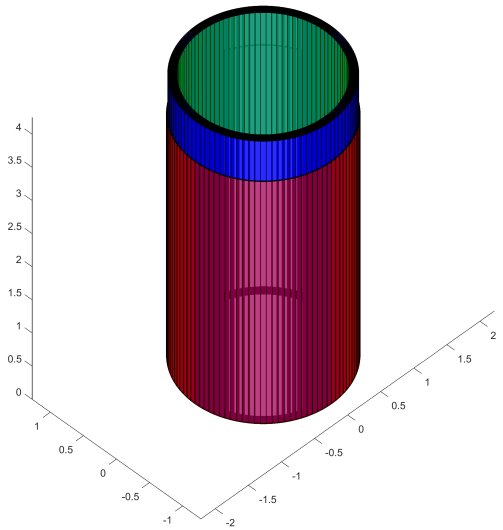

Figure 9.16: $m_p = 500\,[\text{kg}]$ - results 4 - payload/bucket coils/drive coils geometry

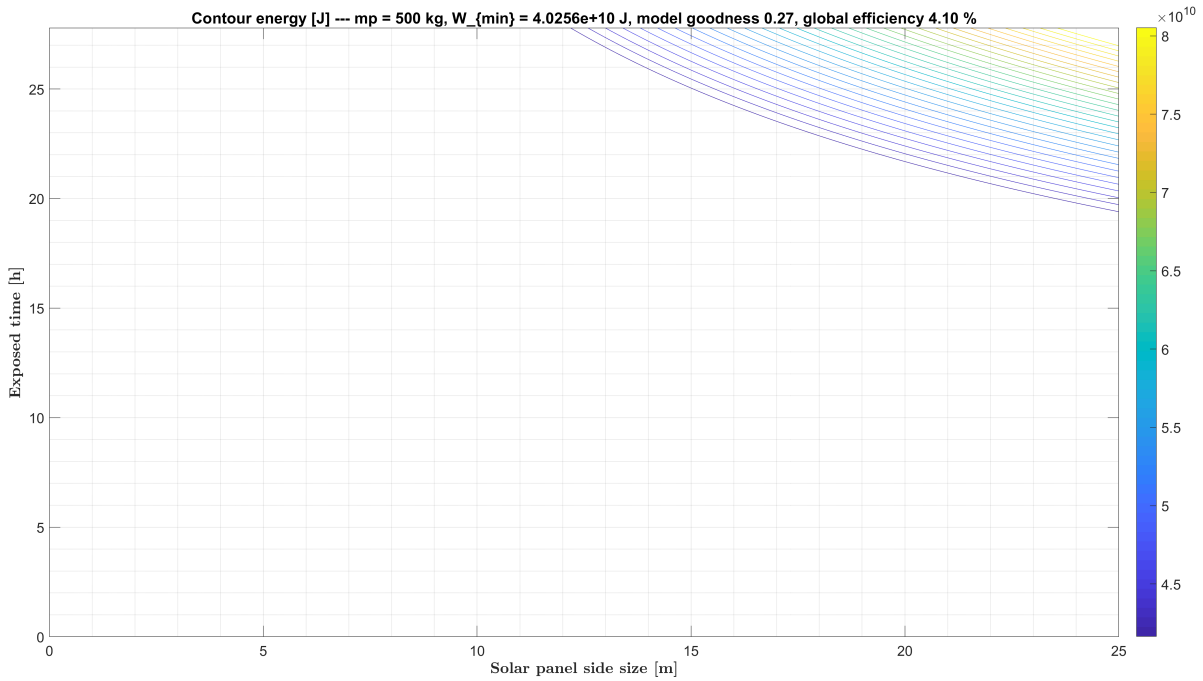

Figure 9.17: $m_p = 500\,[\text{kg}]$ - results 5 - energy contour 1

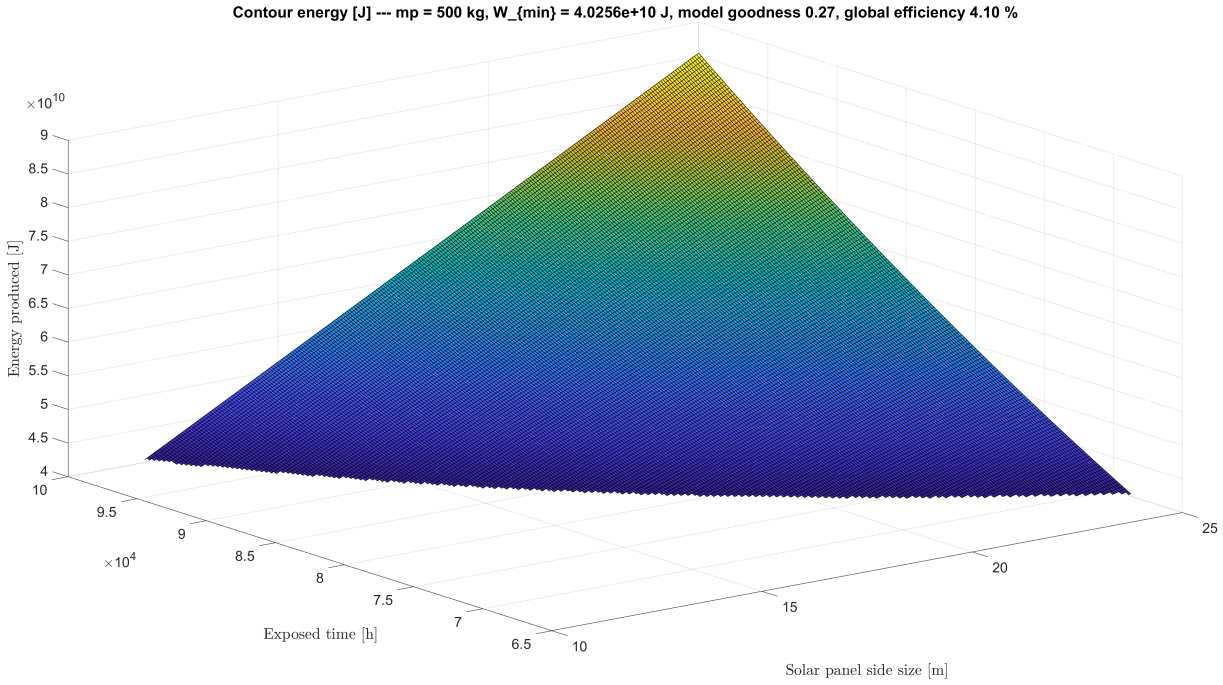

Figure 9.18: $m_p = 500\,[\text{kg}]$ - results 6 - energy contour 2

	Payload mass m_p [kg]		
	5	50	500
$\ell_{SP} = 2.5\,[\mathrm{m}]$	$0.8766 \cdot 10^4$	$1.9923 \cdot 10^4$	– – –
$\ell_{SP} = 5\,[\mathrm{m}]$	$1.2523 \cdot 10^4$	$2.9220 \cdot 10^4$	$0.4383 \cdot 10^5$
$\ell_{SP} = 10\,[\mathrm{m}]$	$1.7532 \cdot 10^4$	$3.9845 \cdot 10^4$	$1.3486 \cdot 10^5$
$\ell_{SP} = 15\,[\mathrm{m}]$	$2.1915 \cdot 10^4$	$4.8700 \cdot 10^4$	$1.7532 \cdot 10^5$
$\ell_{SP} = 20\,[\mathrm{m}]$	$2.9220 \cdot 10^4$	$6.2614 \cdot 10^4$	$2.0386 \cdot 10^5$
$\ell_{SP} = 25\,[\mathrm{m}]$	$4.3830 \cdot 10^4$	$7.3050 \cdot 10^4$	$2.3068 \cdot 10^5$
$\ell_{SP} = 30\,[\mathrm{m}]$	$5.4787 \cdot 10^4$	$8.7660 \cdot 10^4$	$2.5782 \cdot 10^5$
$\ell_{SP} = 35\,[\mathrm{m}]$	$6.2614 \cdot 10^4$	$1.0958 \cdot 10^5$	$2.8277 \cdot 10^5$
$\ell_{SP} = 40\,[\mathrm{m}]$	$6.7431 \cdot 10^4$	$1.2523 \cdot 10^5$	$3.0228 \cdot 10^5$

Table 9.3: Annual tonnage vs solar panel size of area $A = \ell^2$

In Table 9.3 it is possible to appreciate the annual tonnage according to the size of the MD power supply system –solar panel structure– and the payload mass.

10. Conclusions

In this document, the preliminary study of a Mass Driver was presented.

Chapter 1 shows in general why the study of electromagnetic launchers is appropriate, especially for lunar applications. In the continuation, specifically in Chapter 2, Chapter 3, Chapter 4, the key concepts for the preliminary analysis have been examined, namely the electromagnetic phenomena –at the base of the mass driver operating principle–, the mechanical characteristics –to verify the sizing and the structural safety–, and the thermodynamic phenomena –one of the most limiting characteristics for any tradeoff, specifically these phenomena are those that make most an ideal analysis detached from the real one–.

In Chapter 5 there are the main orbital dynamic phenomena, specifically in order to outline the first design parameters of the mass driver: the burnout velocity –launch speed– and the launch location. These considerations are supported by the brief description of the lunar environment and the Shackleton Crater in Chapter 6, allowing to know also relevant parameters such as the ambient base temperature, the solar lighting coverage and the mass driver inclination.

These chapters allowed to make a reasoned choice in Chapter 7, which describes shortly the state of the art of EMLs and chooses the most suitable for the present discussion, specifically a coilgun in the push and pull (inductance) configuration.

Chapter 8 represents the model of the analyzed case study. This chapter clearly shows the whole mathematical model implemented, which parameters –based on the considerations made in the previous Chapters– are included, and what was the logical process with which the optimizer was trained to allow the convergence of the iterations. The various constraints are clearly shown, with all the hypotheses necessary to endorse some linear dependencies.

Finally, in Chapter 9 are presented the results of three different case studies depending on the mass of payload available at launch. From a sample payload of 5 kg, further analyses were carried out with 50 and 500 kg. Based on the results shown and the subsequent sizing of the solar panels, it was found that all three configurations are capable of providing an annual mass at launch of more than 50000 kg (50 tonnes), assuming continuous launches at each recharge cycle. Clearly, the example of only 5 kg deteriorates the components more than making fewer more substantial launches of 500kg.

The 300 tons per year are potentially achieved with a system of solar panels with a total surface of 40×40 meters, or 200 tons a year with 20×20 meters.

As a final remark, the reasons that led to the choice of the PPI CG geometry over reluctance or superconductive models are the cost, the Technology Readiness Level, and the hypotetical effective reliability. The structural resistance analysis was verified retrospectively with a trial-and-error process on the bucket wall thickness.

10.1 Future work

The annual launch tonnage values obtained are lower than other feasibility studies found in literature. It is estimated that a CG, in the simplest version, can launch from 10 to 100 kilotons.

The reasons for which this analysis shows lower values are to be found in the mathematical model and in the assumptions that have led the author to neglect some phenomena to focus attention on others –apparently more influential–.

Therefore, the areas that deserve a more thorough analysis in the future should be pointed out:

• **thermodynamics**: the entire thermodynamic treatment, even if sufficiently detailed, should be validated with a more accurate model that includes radiative phenomena and thermal dissipation times. In particular, it is suggested to investigate how thermal stresses affects long-term performance and, if it is necessary to change materials, how weights and performances at launch are affected;

• **electromagnetics**: the entire electromagnetic interaction, specifically the interpenetration of the magnetic fields, the electromotive force and all the main phenomena that guarantee the acceleration of the payload, should be verified with a more detailed and precise FEM analysis. It is suggested to include in this analysis also the magnetic levitation, with the consequent stability analysis. Furthermore, the actual availability and operating capacity of components that can develop large currents in a very short discharge time should be verified;

• **orbital mechanics**: this part has been left out but will be the focus of the author's personal studies in the future. The orbital analysis would require to understand more clearly the actual lighting times, the launch windows and the various available destinations. A relevant detail would be to be able to position the various payloads in the vicinity of the Lagrangian points, where it could be built a lunar refueling base (like the lunar orbiting base discussed in recent years). Lastly, a factor to be taken into consideration would be to be able to adjust the current pulses: in the hypothetical case in which a lunar MD is built, this would have a fixed geometry but could have at the launch several payloads at different times, or different destinations, and therefore it is opportune to analyze how the electromagnetic interactions change when only the electrical component changes, specifically to understand if the magnetic levitation is still guaranteed at low currents or a flytube must be included.

The entirety of these measures would improve the reliability of the mathematical model that, to date, covers the main electromagnetic and thermal phenomena, and its goodness can be estimated to be around 50%.

A. Material properties

Material	$\rho\,[10^{-8}\,\mathrm{Ohm\,m}]$	$\alpha\,[^{\circ}\mathrm{C}^{-1}]$
Aluminium	2.65	0.0039
Carbon	1	−0.0002
Copper	1.68	0.00404
Gold	2.44	0.0034
Iron	9.71	0.005
Tungsten	5.60	0.0045

Table A.1: List of materials resistivity ρ and temperature coefficient of resistance α (Giancoli 2004)

Material	k
Air	1.00059
Glass	$5 \div 10$
Plexiglass	3.40
Vacuum	1

Table A.2: List of materials dielectric constant k

Material	$\mu_r[\mathrm{H\,m}^{-1}]$
Iron (anneled)	1.26
Cobalt-iron	$2.3 \cdot 10^{-2}$
Iron (pure)	$6.3 \cdot 10^{-3}$
Ferrite	$8 \cdot 10^{-4}$
Nickel	$5 \cdot 10^{-4}$
Aluminium	$1.25665 \cdot 10^{-6}$
Air	$1.25663753 \cdot 10^{-6}$
Vacuum	$4\pi \cdot 10^{-7}$
Copper	$1.256629 \cdot 10^{-6}$
Superconductors	0

Table A.3: List of materials relative magnetic permeability μ_r

Material	Symbol	$\frac{N}{\mathcal{V}}[10^{28}\,\mathrm{e}^{-}\,\mathrm{m}^{-3}]$
Aluminium	Al	18.1
Copper	Cu	8.47
Gold	Au	5.90

Table A.4: List of materials electron density $\frac{N}{\mathcal{V}}$ (Ashcroft and Mermin 1976)

Material	Symbol	T_D[K]
Aluminium	Al	428
Copper	Cu	343
Gold	Au	165
Iron	Fe	470

Table A.5: List of materials Debye temperature T_D (Van Sciver 2012)

Table A.6: Cu and Al properties wrt temperature variations

		Temperature [K]										
		0	10	20	30	40	50	60	70	80	90	100
Cu	ϱ [kg m^{-3}]	9028	9028	9028	9028	9027	9026	9025	9023	9021	9019	9016
	$\mathcal{E}$ [10^9 Pa]	137.0	137.0	136.9	136.9	136.8	136.7	136.5	136.4	136.2	136.0	135.7
	c [J/(kg K)]	≈ 0	0.0872	6.999	26.63	58.54	96.97	135.1	170.4	201.3	227.9	250.7
	k [W/(m K)]	≈ 10	453.2	839.3	992.4	902.6	728.0	600.2	513.0	464.9	436.9	420.9
	ρ [$10^{-8}\Omega$ m]	0.002	0.0021	0.0026	0.0083	0.0239	0.0529	0.0972	0.1528	0.2157	0.2821	0.3479
Al	ϱ [kg m^{-3}]	2734	2734	2734	2734	2734	2734	2733	2733	2732	2731	2730
	$\mathcal{E}$ [10^9 Pa]	76.60	76.59	76.56	76.50	76.40	76.28	76.13	75.96	75.76	75.55	75.31
	c [J/(kg K)]	≈ 0	≈ 1	≈ 10								481.7
	k [W/(m K)]	0	23960	11670	4895.2	2364.8	1284.3	785.8	518.7	368.9	323.8	300.8
	ρ [$10^{-8}\Omega$ m]	0.0001	0.0002	0.0007	0.0045	0.0180	0.0477	0.1029	0.1714	0.2513	0.3412	0.4398

		Temperature [K]										
		100	110	120	130	140	150	160	170	180	190	200
Cu	ϱ [kg m^{-3}]	9016	9013	9010	9007	9003	9000	8996	8992	8988	8984	8980
	$\mathcal{E}$ [10^9 Pa]	135.7	135.5	135.2	134.8	134.5	134.1	133.8	133.3	132.9	132.4	131.9
	c [J/(kg K)]	250.7	270.1	286.6	300.6	312.5	322.5	331.0	338.3	344.6	350.1	354.9
	k [W/(m K)]	420.9	414.2	408.7	404.0	400.1	397.0	394.5	392.6	391.2	390.2	389.5
	ρ [$10^{-8}\Omega$ m]	0.3479	0.4162	0.4852	0.5541	0.6629	0.6917	0.7603	0.8288	0.8973	0.9657	1.034
Al	ϱ [kg m^{-3}]	2730	2729	2728	2727	2725	2724	2723	2721	2720	2718	2716
	$\mathcal{E}$ [10^9 Pa]	75.31	75.06	74.80	74.52	74.24	73.94	73.63	73.31	72.99	72.66	72.33
	c [J/(kg K)]	481.7	528.2	570.6	609.0	643.8	675.3	703.6	729.1	752.0	772.5	790.9
	k [W/(m K)]	300.8	282.8	269.0	258.6	251.1	245.9	242.4	240.1	238.8	238.1	237.6
	ρ [$10^{-8}\Omega$ m]	0.4398	0.5455	0.6571	0.7730	0.8920	1.013	1.133	1.253	1.370	1.483	1.590

		Temperature [K]										
		200	210	220	230	240	250	260	270	280	290	300
Cu	ϱ [kg m^{-3}]	8980	8976	8972	8967	8963	8959	8954	8950	8946	8941	8937
	$\mathcal{E}$ [10^9 Pa]	131.9	131.4	130.8	130.3	129.7	129.1	128.4	127.7	127.0	126.3	125.6
	c [J/(kg K)]	354.9	359.3	363.3	366.9	370.4	373.5	376.4	378.9	381.1	382.7	383.5
	k [W/(m K)]	389.5	389.2	389.0	389.0	389.0	389.0	388.8	388.5	388.0	387.1	385.8
	ρ [$10^{-8}\Omega$ m]	1.034	1.102	1.170	1.239	1.307	1.375	1.443	1.511	1.579	1.647	1.715
Al	ϱ [kg m^{-3}]	2716	2715	2713	2711	2710	2708	2706	2704	2703	2701	2699
	$\mathcal{E}$ [10^9 Pa]	72.33	72.00	71.66	71.31	70.97	70.63	70.28	69.94	69.59	69.25	68.90
	c [J/(kg K)]	790.9	807.4	822.1	835.3	847.2	857.8	867.4	876.1	884.1	891.4	898.2
	k [W/(m K)]	237.6	237.3	236.9	236.5	235.9	235.3	234.7	234.4	234.6	235.6	237.2
	ρ [$10^{-8}\Omega$ m]	1.590	1.711	1.830	1.948	2.065	2.182	2.299	2.414	2.529	2.644	2.758

		Temperature [K]										
		300	320	340	360	380	400	420	440	460	480	500
Cu	ϱ [kg m^{-3}]	8937	8928	8919	8910	8901	8891	8882	8873	8863	8854	8844
	$\mathcal{E}$ [10^9 Pa]	125.6	124.5	123.4	122.2	121.1	120.0	118.8	117.7	116.5	115.3	114.1
	c [J/(kg K)]	383.5	386.0	388.4	390.8	393.2	395.5	397.7	399.8	402.0	404.0	406.0
	k [W/(m K)]	385.8	386.1	385.7	385.3	385.0	384.6	384.2	383.8	383.4	382.9	382.4
	ρ [$10^{-8}\Omega$ m]	1.175	1.852	1.988	2.124	2.261	2.397	2.535	2.672	2.809	2.948	3.086
Al	ϱ [kg m^{-3}]	2699	2695	2691	2687	2683	2679	2675	2671	2667	2663	2659
	$\mathcal{E}$ [10^9 Pa]	68.90	68.21	67.53	66.84	66.15	65.44	64.73	63.99	63.22	62.41	61.54
	c [J/(kg K)]	898.2	910.6	922.0	932.9	943.2	953.1	962.5	971.7	980.5	989.1	997.6
	k [W/(m K)]	237.2	238.6	239.5	240.0	240.1	239.9	239.4	238.8	238.0	237.2	236.2
	ρ [$10^{-8}\Omega$ m]	2.758	2.985	3.210	3.434	3.658	3.881	4.103	4.326	4.549	4.773	4.998

Table A.6: Continued

		Temperature [K]										
		500	520	540	560	580	600	625	650	675	700	750
Cu	ϱ [kg m^{-3}]	8844	8835	8825	8815	8805	8795	8783	8770	8757	8744	8718
	$\mathcal{E}$ [10^9 Pa]	114.1	112.9	111.7	110.5	109.2	108.0	106.4	104.8	103.2	101.6	98.30
	c [J/(kg K)]	406.0	407.9	409.8	411.7	413.5	415.2	417.3	419.4	421.4	423.3	427.2
	k [W/(m K)]	382.4	381.8	381.1	380.3	379.5	378.6	377.4	376.1	374.7	373.2	369.9
	ρ [10$^{-8}\Omega$ m]	3.086	3.225	3.365	3.505	3.646	3.788	3.966	4.146	4.327	4.509	4.879
Al	ϱ [kg m^{-3}]	2659	2655	2651	2646	2642	2637	2631	2626	2620	2614	2601
	$\mathcal{E}$ [10^9 Pa]	61.54	60.61	59.60	58.49	57.27	55.93	54.03	51.86	49.37	46.51	39.49
	c [J/(kg K)]	997.6	1006.0	1014.3	1022.7	1031.2	1039.8	1050.9	1062.5	1074.7	1087.6	1116.0
	k [W/(m K)]	236.2	235.2	234.2	233.1	232.0	230.9	229.4	227.9	226.4	224.8	221.3
	ρ [10$^{-8}\Omega$ m]	4.998	5.225	5.453	5.683	5.915	6.151	6.449	6.752	7.062	7.378	8.031

		Temperature [K]										
		750	800	850	900	950	1000	1050	1100	1150	1200	1250
Cu	ϱ [kg m^{-3}]	8718	8692	8666	8640	8614	8586	8559	8531	8502	8474	8444
	$\mathcal{E}$ [10^9 Pa]	98.30	94.95	91.53	88.05	84.50	80.89	77.21	73.74	69.66	65.79	61.86
	c [J/(kg K)]	427.2	431.1	435.0	439.2	443.8	448.9	454.8	461.6	469.6	479.0	490.0
	k [W/(m K)]	369.9	366.4	362.8	359.1	355.4	351.9	348.5	345.3	342.3	339.2	336.0
	ρ [10$^{-8}\Omega$ m]	4.879	5.255	5.640	6.033	6.435	6.848	7.272	7.707	8.155	8.616	9.091
Al	ϱ [kg m^{-3}]	2601	2588	2575	2562	$\mathrm{Al_s}\rightharpoonup\mathrm{Al}_\ell$						
	$\mathcal{E}$ [10^9 Pa]	39.49	31.57	22.83	12.90	$\mathrm{Al_s}\rightharpoonup\mathrm{Al}_\ell$						
	c [J/(kg K)]	1116.0	1148.7	1186.7	1231.0	$\mathrm{Al_s}\rightharpoonup\mathrm{Al}_\ell$						
	k [W/(m K)]	221.3	217.6	213.7	210.0	$\mathrm{Al_s}\rightharpoonup\mathrm{Al}_\ell$						
	ρ [10$^{-8}\Omega$ m]	8.031	8.719	9.444	10.21	$\mathrm{Al_s}\rightharpoonup\mathrm{Al}_\ell$						

Bibliography

Adam, J. (2015). *In Search for Preece and Onderdonk*. UltraCAD Design, Inc. URL: http://www.ultracad.com (visited on 11/27/2017) (cited on page 87).

Akyel, C. and S. I. Babic (2007). "Mutual inductance between coaxial circular coils of rectangular cross section and thin coaxial circular coils with constant current density in air (filament method)". In: volume 6, pages 102–108. ISBN: 978-9608457744 (cited on page 26).

Andrews, J. A. and J. R. Devine (1991). "Armature Design for Coaxial Induction Launchers". In: *IEEE Transaction on Magnetics* 27 (1). DOI: 10.1109/20.101109 (cited on pages 73, 75).

Ashcroft, N. W. and D. N. Mermin (1976). *Solid State Physics*. 1st edition. Brooks Cole. ISBN: 978-0030839931 (cited on pages 41, 108).

Barrera, T. and R. Beard (2014). "Exploration and Verification Analysis of a Linear Reluctance Accelerator". In: *17th International Symposium on Electromagnetic Launch Technology*. DOI: 10.1109/EML.2014.6920629 (cited on page 72).

Bate, R. R., D. D. Mueller, and J. E. White (1971). *Fundamentals of Astrodynamics*. Revised edition. Dover Publications. ISBN: 978-0486600611 (cited on page 68).

Baum, C. E. (2007). *Some Electromagnetic Considerations for Design of Railgun Electromagnetic Projectile Launchers*. Technical report. PEP8-1. Albuquerque, New Mexico // Air Force Office of Scientific Research: Department of Electrical and Computer Engineering. URL: http://ece-research.unm.edu (cited on page 70).

Boles, M. A. (2014). *Thermodynamics: An Engineering Approach*. 8th edition. McGraw-Hill Education. ISBN: 978-0073398174 (cited on page 40).

Bresie, D. A. and J. A. Andrews (1991). "Design of a Reluctance Accelerator". In: *IEEE Transactions on Magnetics*. DOI: 10.1109/20.101106 (cited on page 72).

Bryant, S. (2009). "Lunar pole illumination and communications maps computed from GSSR elevation data". In: INSPEC Accession Number: 10625267. DOI: 10.1109/AERO.2009.4839375 (cited on page 90).

Cengel, Y. A. (2002). *Heat Transfer: A Practical Approach*. 2nd edition. McGraw-Hill. ISBN: 978-0072458930 (cited on pages 39, 48, 49).

Chilton, F. (1977). "Mass driver theory and history". In: *AIAA 3rd Conference on Space Manufacturing Facilities*. DOI: 10.2514/6.1977-533 (cited on page 69).

Curtis, H. D. (2013). *Orbital Mechanics for Engineering Students*. 3rd edition. Butterworth-Heinemann. ISBN: 978-0080977478 (cited on pages 63, 64).

Daldaban, F. and V. Sari (2014). "Design and Implementation of a Three-Coil Linear Reluctance Launcher". In: *16th International Power Electronics and Motion Control Conference and Exposition*. DOI: 10.1109/EPEPEMC.2014.6980653 (cited on page 72).

Davis, E. W. (2018). *Advanced Propulsion Study*. Air Force Research Laboratory (AFMC). Approved for public release; distribution unlimited. URL: https://www.researchgate.net/publication/235107865_Advanced_Propulsion_Study (visited on 01/24/2018) (cited on page 73).

Easton, R. L. Jr. (2010). *Fourier Methods in Imaging*. Wiley. ISBN: 978-0-470-68983-7 (cited on page 19).

Eland Cables (2018). *Online resource*. URL: http://www.elandcables.com (visited on 01/16/2018) (cited on page 54).

Engel, T. G. and D. W. Mueller (2009). "High-Speed and High-Accuracy Method of Mutual-Inductance Calculations". In: *IEEE Transactions on Plasma Science* 37 (5). DOI: 10.1109/TPS.2009.2014764 (cited on page 24).

Engel, T. G. and S. N. Rohe (2006). "A Comparison of Single-Layer Coaxial Coil Mutual Inductance Calculations Using Finite-Element and Tabulated Methods". In: *IEEE Transactions on Magnetics* 42 (9). DOI: 10.1109/TMAG.2006.880687 (cited on pages 24, 25).

Estalote, E. A. and K. G. Ramanathan (1977). "Low-temperature emissivities for copper and aluminium". In: *Journal of the Optical Society of America* 67 (1), pages 39–44. DOI: 10.1364/JOSA.67.000039 (cited on page 50).

Gere, J. M. (2003). *Mechanics of Materials*. 6th edition. Thomson-Engineering. ISBN: 978-0534417932 (cited on pages 29, 30).

Giancoli, D. C. (2004). *Physics: Principles with Applications*. 6th edition. Pearson/Prentice Hall. ISBN: 978-0130606204 (cited on page 107).

Hahn, D. W. and M. N. Özişik (2012). *Heat Conduction*. 3rd edition. John Wiley & Sons Inc. ISBN: 978-0470902936 (cited on page 47).

Hambley, A. R. (2009). *Elettrotecnica*. Italian. Edited by F. Grasso, A. Luchetti, and M. C. Piccirilli. 4th edition. Prentice Hall. ISBN: 978-8871925561 (cited on page 16).

Haruyama, J. et al. (2008). "Lack of Exposed Ice Inside Lunar South Pole Shackleton Crater". In: *Science* 322 (5903), pages 938–939. DOI: 10.1126/science.1164020 (cited on pages 67, 90).

He, Y. et al. (2010). "Efficiency Analysis of an Electromagnetic Railgun With a Full Circuit Model". In: *IEEE Transaction on Plasma Science* 38 (12), pages 3425–3428. DOI: 10.1109/TPS.2010.2082567 (cited on page 70).

Holland, M. G. (1963). "Analysis of Lattice Thermal Conductivity". In: *Physical Review* 132.6. DOI: 10.1103/PhysRev.132.2461 (cited on page 34).

Jackson, J. D. (1998). *Classical Electrodynamic*. 3rd edition. Wiley. ISBN: 978-0471309321 (cited on page 9).

JAHM Software, Inc. (1998). *Material Properties DataBase*. https://www.jahm.com/ (cited on pages 13, 35).

Jones, R. J. and W. F. Wright (1992). *High Temperature Dielectric Polymer Film Insulation*. Technical report. WL-TR-91-2105. Strategic Defense Initiative Office: Aero Propulsion and Power Directorate, Wright Laboratory. URL: http://www.dtic.mil/dtic/tr/fulltext/u2/a255243.pdf (cited on page 55).

Karwa, R. (2017). *Heat and Mass Transfer*. 1st edition. Springer. ISBN: 978-9811015564 (cited on pages 47, 49).

Kolm, H. H., P. Mongeau, and F. Williams (1980). "Electromagnetic Launchers". In: *IEEE Transaction on Magnetics* 16 (5), pages 719–721. DOI: 10.1109/TMAG.1980.1060806 (cited on pages 2, 69, 74).

Korsmeyer, D., C. Bilby, and N. Nottke (1990). "A Superconducting Quenchgun for Delivering Lunar Derived Oxygen to Lunar Orbit". In: *26th Joint Propulsion Conference*. DOI: 10.2514/6.1990-2369 (cited on page 73).

Laminated Plastics (2018). *Online Resource*. URL: www.laminatedplastics.com (visited on 02/15/2018) (cited on page 83).

Langford-Smith, F. (1952). *Radiotron Designer's Handbook*. 4th edition. The Wireless Press. ISBN: B001D4OHV0 (cited on pages 15, 26, 27).

Lianos, D. and J. L. Brown (Sept. 27, 1994–Sept. 29, 1994). "Hypervelocity Coil Guns, Rail Guns and Light Gas Guns". In: *Space Programs and Technologies Conference and Exhibit*. AIAA SPACE Forum. Huntsville, AL. DOI: 10.2514/6.1994-4627 (cited on page 70).

Masugata, K. (1997). "Hyper Velocity Acceleration by a Pulsed Coilgun Using Traveling Magnetic Field". In: *IEEE Transaction on Magnetics* 33 (6), pages 4434–4438. DOI: 10.1109/20.649877 (cited on page 70).

Maxwell, J. K. (1892a). *A Treatise on Electricity and Magnetism*. Volume 1. University of Michigan Library. ISBN: 978-1140219675 (cited on page 15).

– (1892b). *A Treatise on Electricity and Magnetism*. Volume 2. University of Michigan Library. ISBN: 978-0511709340 (cited on page 25).

Millikan, R. A. and E. S. Bishop (2016). *Elements of Electricity: A Practical Discussion of the Fundamental Laws and Phenomena of Electricity and Their Practical Applications in the Business and Industrial World*. Palala Press. ISBN: 978-1355810230 (cited on page 4).

Morgan, J. (July 6, 1997–July 9, 1997). "A brief history of cannon launch". In: *33rd Joint Propulsion Conference and Exhibit*. Joint Propulsion Conferences. Seattle, WA. DOI: 10.2514/6.1997-3138 (cited on page 70).

Nalty, K. (2011). *Classical Calculation for Mutual Inductance of Two Coaxial Loops in MKS Units*. URL: http://www.kurtnalty.com/Helmholtz.pdf (visited on 11/26/2017) (cited on pages 21, 23).

O'Neill, G. K., J. Billingham, and W. Gilbreath (1979). "Space Resources and Space Settlements: Technical Papers Derived from the 1977 Summer Study at NASA Ames Research Center". In: *US Government Printing Office 0—293-364*. URL: https://ntrs.nasa.gov/search.jsp?R=19790024054 (cited on pages 69, 71, 74).

O'Neill, G. K. and B. O'Leary (1977). "Space-Based Manufacturing from Nonterrestrial Materials: Technical Papers Derived from the 1976 Summer Study at NASA Ames Research Center". In: *AIAA Progress in Astronautics and Aeronautics* 57. DOI: 10.2514/4.865312 (cited on pages 69, 74).

Onderdonk, I. M. (1944). "Short-time Current Required to Melt Copper Conductors". In: *Electrical World* 121 (26), page 98. URL: http://www.ultracad.com/articles/reprints/electrical_world.pdf (cited on page 88).

Pässler, R. (2017). "Unprecedented Integral-Free Debye Temperature Formulas: Sample Applications to Heat Capacities of ZnSe and ZnTe". In: *Hindawi, Advances in Condensed Matter Physics*. DOI: 10.1155/2017/9321439 (cited on page 45).

Patterson, J. and B. Bailey (2016). *Solid-State Physics: Introduction to the Theory*. 2nd edition. Springer. ISBN: 978-3662499948 (cited on page 45).

Perfetti, R. (2012). *Circuiti Elettrici*. Italian. 2nd edition. Zanichelli. ISBN: 978-8808178886 (cited on page 16).

Physics, Stackexchange (2017). https://physics.stackexchange.com/. Retrived on 2017-11-10 (cited on page 5).

Plastelec SAS (2018). *Online resource*. URL: http://www.plastelec.com (visited on 01/16/2018) (cited on page 54).

Ramanathan, K. G. and S. H. Yen (1977). "High-temperature emissivities of copper, aluminium, and silver". In: *Journal of the Optical Society of America* 67 (1), pages 32–38. DOI: 10.1364/JOSA.67.000032 (cited on page 50).

Recktenwald, G. W. (2017). *Finite-Difference Approximations to the Heat Equation*. URL: http://www.nada.kth.se (visited on 12/26/2017) (cited on page 55).

Richmond, M. (2017). *Astrophysical Sciences and Technology Program Faculty*. URL: http://spiff.rit.edu/classes (visited on 11/26/2017) (cited on page 8).

Romanowski, B., D. Chrobak, J. Räisänen, and R. Nowak (2015). "Elasticity and Debye temperature of defected fcc crystals ($AlCu_3$, Al, Cu): Molecular dynamics and first-principles calculations". In: *Computational Materials Science* 109. DOI: 10.1016/j.commatsci.2015.07.018 (cited on page 34).

Rosa, E. B. and F. W. Grover (2016). *Formulae and Tables for the Calculation of Mutual and Self-Inductance (1908)*. Edited by National Institute of Standards and Technology. Palala Press. ISBN: 978-1-333-93611-2 (cited on pages 15, 21, 23, 24, 26).

Schroeder, D. V. (1999). *Introduction to Thermal Physics*. 1st edition. Addison-Wesley. ISBN: 978-0201380279 (cited on pages 41–43, 45).

Sears, F. W. (1958). *Electricity and Magnetism (Principles of Physics Series)*. 1st edition. Addison-Wiley. ISBN: B000H4O0TQ (cited on page 20).

Sefton-Nash, E., M. A. Seigler, and D. A. Paige (2017). *Thermal Extremes in Permanently Shadowed Regions at the Lunar South Pole*. URL: https://www.lpi.usra.edu/meetings/lpsc2013/eposter/2617.pdf (visited on 11/27/2017) (cited on pages 13, 88).

Sievers, A. J. (1978). "Thermal radiation from metal surfaces". In: *Journal of the Optical Society of America* 68 (11), pages 1505–1516. DOI: 10.1364/JOSA.68.001505 (cited on page 50).

Smythe, W. R. (1989). *Static and Dynamic Electricity*. 3rd edition. Hemisphere Publishing Corporation. ISBN: 0-89116-917-2 (cited on page 15).

Snow, W. R., R. S. Dunbar, J. A. Kubby, and G. K. O'Neill (1982). "Mass Driver Two: a Status Report". In: *IEEE Transaction on Magnetics* 18 (1), pages 127–134. DOI: 10.1109/TMAG.1982.1061777 (cited on page 74).

Snow, W. R. and H. H. Kolm (1992). *Electromagnetic Launch of Lunar Material*. Technical report. Energy, Power, and Transport: ID 19930007725. Johnson Space Center, Space Resources: NASA, pages 117–135. URL: https://ntrs.nasa.gov/search.jsp?R=19930007725 (cited on page 73).

Snow, W. R. and G. K. O'Neill (1979). *Construction and Testing of the 2.5m Mass Driver*. Technical report. Princeton, N. J.: Princeton/AIAA/DGLR 14th International Electric

Propulsion Conference. URL: http://arc.aiaa.org%20%7C%20DOI:%2010.2514/6.1979-2095 (cited on page 74).

SPICE (2018). *NASA's NAIF, SPICE: An Observation Geometry System for Space Science Missions*. URL: https://naif.jpl.nasa.gov/naif (visited on 01/20/2018) (cited on page 59).

Stauffacher, E. R. and I. M. Onderdonk (1928). "Short-time Current Carrying Capacity of Copper Wire". In: *General Electric Review* 31 (6), pages 326–327. URL: http://www.ultracad.com/articles/reprints/stauffacher.pdf (cited on page 88).

Stoica, A. et al. (2016). "TransFormers of Extreme Environments and Their Integration in a Solar Power Infrastructure". In: *AIAA SPACE Forum*. DOI: 10.2514/6.2016-5326 (cited on pages 13, 88).

Tan, D., L. Zhang, Q. Chen, and P. Irwin (2014). "High-Temperature Capacitor Polymer Films". In: *Journal of Electronic Materials* 43 (12), pages 4569–4575. DOI: 10.1007/s11664-014-3440-7 (cited on page 55).

Vallado, D. A. (2007). *Fundamentals of Astrodynamics and Applications*. 3rd edition. Microcosm Press/Springer. ISBN: 978-1881883142 (cited on pages 60–62).

Van Sciver, S. W. (2012). *Helium Cryogenics*. 2nd edition. Springer. ISBN: 978-1493901593 (cited on pages 43, 45, 48, 50, 108).

Wang, D., Q. She, Y. Zhu, and J. Chen (1997). "The Magnetic Levitation of the Projectile in Coilguns". In: *IEEE Transaction on Magnetics* 33 (1), pages 195–200. DOI: 10.1109/20.559945 (cited on page 10).

Whittaker, E. T. (2012). *A History of the Theories of Aether and Electricity: From the Age of Descartes to the Close of the Nineteenth Century (1910)*. Oxford City Press. ISBN: 978-1781391303 (cited on page 4).

Wigley, D. (2012). *Mechanical Properties of Materials at Low Temperatures (The International Cryogenics Monograph Series)*. 1st edition. Softcover reprint of the original 1st ed. 1971. Springer. ISBN: 978-1468418897 (cited on page 35).